



Title	Study on Governing Factor for Oxygen Reduction Reaction Activity of Electrocatalyst for Polymer Electrolyte Fuel Cells
Author(s)	垣内, 孝宏
Citation	北海道大学. 博士(工学) 甲第11886号
Issue Date	2015-03-25
DOI	10.14943/doctoral.k11886
Doc URL	http://hdl.handle.net/2115/60733
Type	theses (doctoral)
File Information	Takahiro_Kaito.pdf



[Instructions for use](#)

Study on Governing Factor for Oxygen
Reduction Reaction Activity of Electrocatalyst
for Polymer Electrolyte Fuel Cells

固体高分子型燃料電池用電極触媒の
酸素還元活性の支配因子に関する研究

Takahiro KAITO

垣内 孝宏

Division of Quantum Science and Engineering,
Graduate School of Engineering,
Hokkaido University

March 2015

Table of contents

Chapter 1 : Introduction	1
1.1 Fuel cell	2
1.1.1 Basics of fuel cell	2
1.1.2 Operational voltage of fuel cell	4
1.1.3 Enhancement of ORR activity	6
1.1.4 Challenge of fuel cell for FCEV applications	7
1.2 Review of X-ray absorption fine structure analysis	9
1.2.1 X-ray absorption fine structure	9
1.2.1.1 XANES	10
1.2.1.2 EXAFS	10
1.2.2 X-ray absorption fine structure analysis on PEFC electrocatalyst	11
1.3 Review of PEFC electrocatalyst	13
1.3.1 Pt electrocatalyst	13
1.3.2 Core-shell Electrocatalyst	13
1.3.3 Pt alloy electrocatalyst	14
1.4 Objectives and outline of this research	18
1.5 References	19
Chapter 2 : Development of Spectroelectrochemical Cell for <i>in situ</i> XAFS	
Experiment	25
2.1 Introduction	26
2.2 Basic concepts for the cell design	28

2.3 Experimental	29
2.3.1. <i>In situ</i> electrochemical cell for Pt and Au K-edge EXAFS measurements ...	29
2.3.2 XAFS measurement	37
2.4 Results and discussions	38
2.4.1 Electrode performance in the spectroelectrochemical cell	38
2.4.2 Pt K-edge EXAFS measurement of Pt foil	41
2.4.3 XAFS measurement with the electrochemical cell	44
2.4.4 EXAFS measurement of the Pt/Au/C electrocatalyst in the electrochemical cell	47
2.5 Conclusions	51
2.6 References	52

Chapter 3 : K-edge X-ray Absorption Fine Structure Analysis of Pt/Au Core-Shell

Electrocatalyst – Evidence for Short Pt-Pt Distance –	55
3.1 Introduction	56
3.2 Materials and methods	57
3.2.1 Preparation of Pt/Au/C core-shell electrocatalyst	57
3.2.2 Characterization of Pt/C and Pt/Au/C core-shell electrocatalysts	57
3.2.3 XAFS measurements	58
3.2.4 XAFS analyses	59
3.3 Results	61
3.3.1 Characterization of Pt/C and Pt/Au/C core-shell electrocatalysts	61
3.3.2 ORR activity of Pt/Au/C core-shell electrocatalysts	66
3.3.3 XAFS analysis	68

3.3.3.1 Reference foils	68
3.3.3.2 Pt/C electrocatalyst	73
3.3.3.3 Pt/Au/C core-shell electrocatalyst	76
3.4 Discussions	80
3.4.1 Estimation of Pt/C and Pt/Au/C core-shell electrocatalyst structures	80
3.4.1.1 Estimation of the structure of Pt/C nanocluster	80
3.4.1.2 Estimation of the structure of Pt/Au/C	80
3.4.2 Bond length and electrochemical ORR activity of Pt/Au/C	84
3.4.3 The origin of Pt-Pt contraction of Pt/Au/C	87
3.5 Conclusions	89
3.6 References	90

Chapter 4 : <i>In situ</i> X-Ray Absorption Fine Structure Analysis of PtCo, PtCu and PtNi Alloy Electrocatalyst-The origin for Enhanced Activity of Oxygen Reduction Reaction	93
4.1 Introduction	94
4.2 Materials and methods	95
4.2.1 Preparation of PtCo/C, PtCo/C-HT, PtCu/C, PtCu/C-HT and PtNi/C electrocatalyst	95
4.2.2 Characterization of Pt/C, PtCo/C, PtCo/C-HTs, PtCu/C, PtCu/C-HT and PtNi/C electrocatalysts	97
4.2.3 XAFS measurement	98
4.3 Results	100
4.3.1 Characterization of PtCo/C, PtCo/C-HT, PtCu/C, PtCu/C-HT and PtNi/C electrocatalysts.....	100
4.3.2 ORR activities of Pt/C, PtCo/C, PtCo/C-HTs, PtCu/C, PtCu/C-HT and PtNi/C	

electrocatalysts	113
4.3.3 XAFS analysis	117
4.3.3.1 XANES analysis of PtCo/C, PtCo/C-HTs, PtCu/C, PtCu/C-HT and PtNi/C electrocatalyst	117
4.3.3.2 EXAFS analysis of Reference foils and Pt/C base electrocatalyst	123
4.3.3.3 EXAFS analysis of PtCo/C, PtCo/C-HTs, PtCu/C, PtCu/C-HT and PtNi/C electrocatalyst	125
4.4 Discussions	130
4.4.1 Estimation of PtCo/C electrocatalysts internal structures	130
4.4.2 Bond length and electronic effects to the ORR activity of electrocatalyst ..	131
4.5 Conclusions	139
4.6 References	140
Chapter 5 : General conclusions and discussions	145
5.1 General conclusions of thesis	146
5.2 General discussions	147
5.2.1 The effect of Pt-Pt contraction on ORR activity	147
5.2.2 Activity enhancement in an actual fuel cell stack	150
5.3 References	152
Acknowledgements	155

Chapter 1

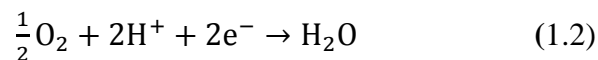
Introduction

1.1 Fuel cell

1.1.1 Basics of fuel cell

The first demonstration of fuel cell (FC) was conducted by William Grove in 1839, using experimental device consisted of one large beaker filled with dilute acid electrolyte and two pair of platinum electrode and test tube as shown in Figure 1.1.¹ Water was electrolyzed into hydrogen and oxygen by passing an electric current using power supply as shown in Fig. 1.1(a). After that power supply was replaced with the current ammeter, then small current was observed. Oxygen and hydrogen were consumed and electric current was produced. Gradually electric current became smaller, and finally it disappeared after the consumption of oxygen and hydrogen.

However actual FC continues to generate electricity as long as fuel is supplied. This is the large difference between FC and battery and the advantage of FC electric vehicle (FCEV) comparing with electric vehicle (EV). Hence FCEV would cruise more than 500 km after a few minutes of hydrogen charge. On the other hand according to Nissan motor official website world best seller commercial EV, Nissan Leaf FY2014 model takes 30 minutes to quick charge electricity for approximately 200 km cruising range at JC08 cruising testing mode. In addition compared with internal combustion engines (ICE) automobiles, FCEV has advantage in efficiency. Although ICE automobiles burns the fuel directly accompanying release of heat, FC splits the combustion reaction into two electrochemical half reactions described by equation (1.1), (1.2) and directly produces the electricity. Hence maximum efficiency of FC is higher than that of ICE.



Equation (1.1) indicates the anode reaction releasing the electrons and H^+ ions, which is hydrogen oxidation reaction (HOR). Equation (1.2) indicates the cathode reaction, in which oxygen reacts with electrons taken from the electrode thorough external circuit and H^+ ions from the anode through the electrolyte, which is the oxygen

reduction reaction (ORR). Overall electrochemical reaction of FC is described as equation (1.3).



The change of Gibbs free energy for the reaction of equation (1.3) is the released energy. It is 237.2 kJmol^{-1} at 25 C° . Electromotive force (EMF) is calculated from the change of Gibbs free energy. The maximum EMF at 25 C° for the reaction is 1.23 V with liquid water formation and the efficiency limit known as thermodynamic efficiency is 83% on HHV basis.

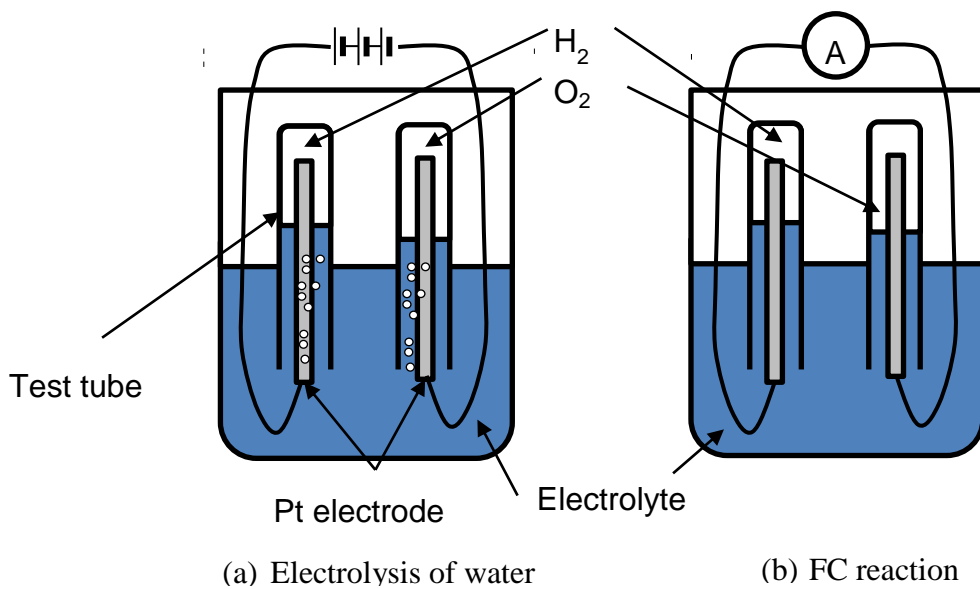


Figure 1.1 Schematic diagram of experimental system

1.1.2 Operational voltage of fuel cell

Figure 1.2 shows the schematic drawing of polymer electrolyte FC (PEFC) stack. It consists of electrolyte membrane, catalyst layers, gas diffusion layers (GDL), and bipolar plates (BPP). The function of each component is shown in red character. ORR and HOR reaction undergoes at cathode and anode electrocatalyst layers, respectively. Hydrogen diffuses from anode flow channel to anode electrocatalyst layer through GDL. Then proton generated at the anode electrocatalyst layer moves through the electrolyte membrane and react at the cathode catalyst layer with the oxygen diffused from the cathode flow channel of BPP. Electrons move to cathode electrocatalyst through anode GDL, anode BPP, external circuit, cathode BPP and cathode GDL. Generated water at cathode catalyst layer is ejected to flow channels then exhausted to outside of FC stack.

If there are no losses in the reaction of equation (1.3), theoretical voltage would be obtained. However in an actual FC stack theoretical voltage is not obtained because of several internal losses as shown in Figure 1.3. Internal losses are divided into following three losses, ohmic loss, reaction loss and mass transfer loss. In these three losses reaction loss is the largest one and has predominant effect on the voltage of entire current density. Ohmic loss would be improved by the reduction of contact resistivity and bulk resistivity of component as BPP or GDL used in FC stack. Mass transfer loss also would be improved by changing the properties of component materials of GDL or dimension of flow channel of BPP. Hence the voltage of high current density would be improved on some level by advancement of engineering. However the voltage around low current density would not be improved drastically by other methods except for the reduction of reaction loss as shown in Fig. 1.3. Especially for the application to FCEV, voltage at low current density is important from the standpoint of the extension of cruising range through the hydrogen fuel consumption reduction, because the economic point of operation of FC stack is at the low current density.

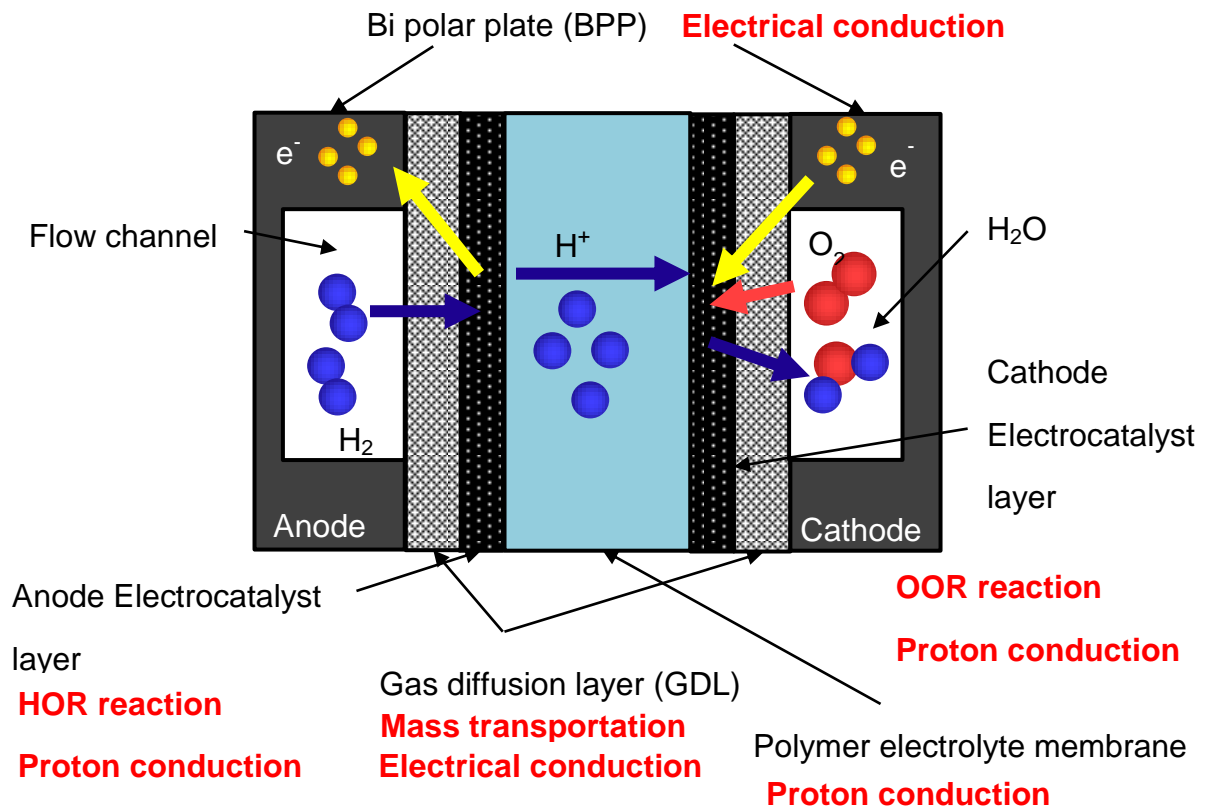


Figure 1.2 Schematic drawing of PEMFC cell

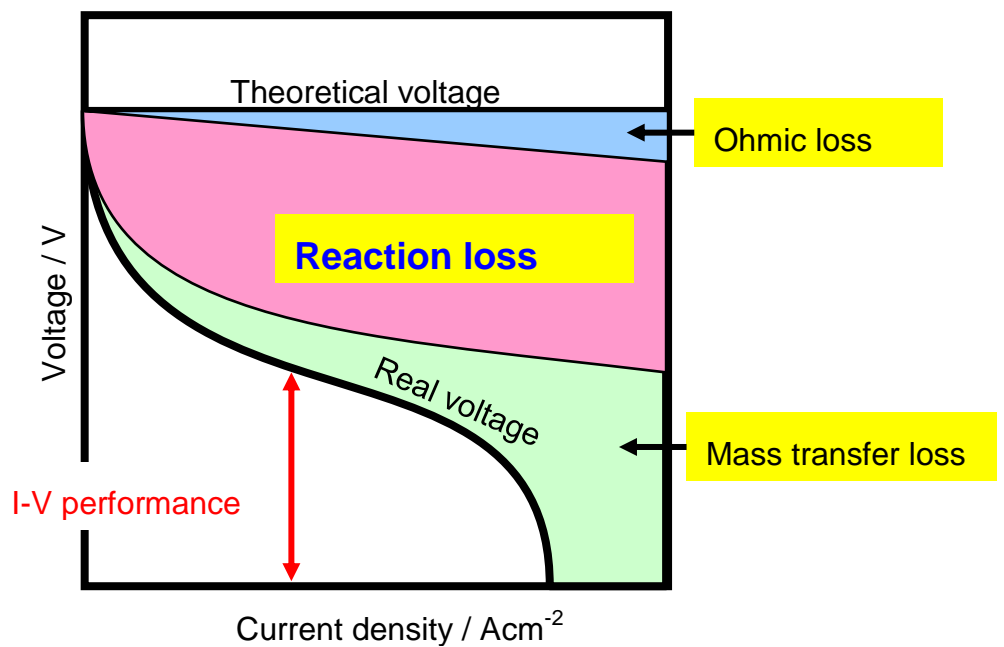


Figure 1.3 Schematic performance (I-V curve) curve and internal resistance

1.1.3 Enhancement of ORR activity

The only method to reduce the reaction loss is enhancement of activity of electrocatalyst on ORR. The activity of electrocatalyst is explained by the equation below.

$$i_m = i_a \times A_{\text{ECSA}} \quad (1.4)$$

where i_m is the mass specific activity and i_a is the area specific activity and A_{ECSA} is the electrochemical active area. Hence there are two ways to improve the mass specific activity. One is the expansion of electrochemical active area (A_{ECSA}). Another is the enhancement of area specific activity (i_a).

For the expansion of A_{ECSA} , Pt atoms which are not used in the reaction directly have to be reduced. One method is the reduction of particle diameter because the ratio of Pt surface increases. However the reduction of diameter is limited because that of typical Pt electrocatalyst is already small around 2 to 3 nm. When the diameter is reduced less than 2 nm, the stability as a nanoparticle deteriorates. Another method is the reduction of Pt mole fraction in a nanoparticle as the alloying of other element except for Pt. There are several alloying structures as core-shell or random alloy or intermetallic. Among them, core-shell structure which consists of Pt shell and core of other metallic element is most promising to increase the A_{ECSA}

Meanwhile for the enhancement of i_a , catalytic activity of each surface Pt has to be improved. For the enhancement of catalysis, surface structure and electronic states of surface Pt atoms have to be changed. One of the methods is the alloying again where addition of other elements to Pt particles induces electron transfer between Pt and other elements metals. In addition atomic distance of Pt atoms may be changed by the stress induced by the added atoms which have different atomic radius from the Pt atom. Hence alloying is a promising method to increase both A_{ECSA} and i_a .

1.1.4 Challenge of fuel cell for FCEV applications

As described in previous sections PEFCs are promising as future power sources for automobiles because they do not emit greenhouse gases during their operation, and operates at higher efficiency than ICE automobiles, and has longer extension in the cruising range and requires shorter energy charging time than EVs. However, there are unresolved several issues before the worldwide usage of FCEVs. The issues are low power density of FC stack, low efficiency of the entire power-train system, low durability under a wide range of operating conditions and environments including freeze-start, and finally high cost of total FC system.² In these issues cost is the most important issue to be solved for the wide spread of the FCEV, because other issues can be solved by using expensive FC system. In fact fuel cell commercial sedan automobile has been already released by Toyota motor in December 2014 in Japan. This fact means that the FCEV is already usable in the real world. However the price of the car is still expensive.

To reduce the cost of FCEV enhancement of the mass-specific activity of Pt electrocatalyst for ORR is most important.³ The reason is as follows. Activity improvement has several effects on the cost reduction of FC system not only reduction of Pt usage of FC stack itself, but also the reduction of FC stack size and reduction of air compressor size thorough the reduction of operating pressure. According to US DOE FC stack and air management system shares approximately 50 % and 16 % of total FC system potential cost respectively.⁴ In addition electrocatalyst shares 50 % of FC stack cost. That is to say electrocatalyst shares 25 % of total FC system cost. Detail description of several benefits of the activity improvement of electrocatalyst for cost reduction of FC stack are following as decreasing of number of cells, size of active areas of a cell, and Pt loading per unit active area. All of them lead to the reduction of the expensive Pt usage accompanied by the improvement of the power density. Considering the FCEV application improvement of power density is significant to mount the FC system under the bonnet hood avoiding the development of the special

vehicle body. In addition the expansion of FCEVs to several segment automobiles as sedan, coupe, and sport utility vehicles would be easy by that.

Meanwhile to improve the mass specific activity of Pt, expansion of A_{ECSA} and enhancement of i_a are required as described in section 1.1.3. In order to improve the i_a , the structure of Pt electrocatalysts and the reaction mechanism have to be studied for understanding of ORR catalysis at the atomic level.⁵⁻⁹

1.2 Review of X-ray absorption fine structure analysis

1.2.1 X-ray absorption fine structure¹⁰

X-ray absorption fine structure (XAFS) includes both Extended X-ray absorption fine structure (EXAFS) and X-ray absorption near edge structure (XANES) as shown in Figure 1.4. Experimentally X-ray absorption coefficient of samples is measured with scanning the incident X-ray energy towards higher side. When the incident X-ray energy agrees with the binding energy of a core electron of an atom in the sample, incident X-ray is absorbed by the sample drastically, causing a drop in the transmitted X-ray intensity. This results in an absorption edge. Each element on the periodic table has a set of intrinsic absorption edges as K, L, M... from low to high energy corresponding to different binding energies of its electrons. This gives element selectivity of XAFS analysis. The region within -50 eV of an absorption edge is so called XANES region and the region beyond 50 eV to over 1500 eV is called EXAFS regions. EXAFS region includes weak modulation of absorption coefficient.

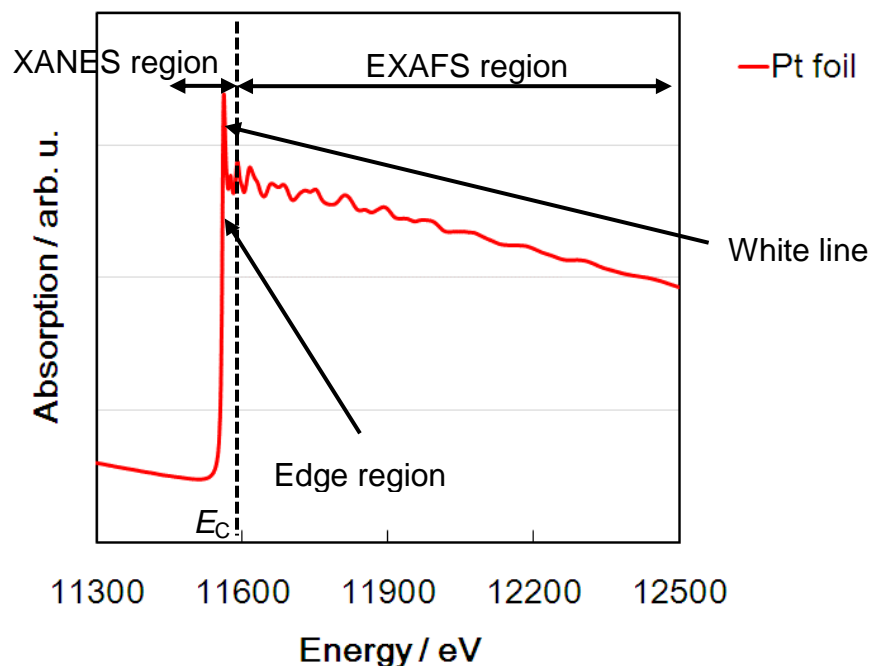


Figure 1.4 Pt L_{III} XAFS spectrum of Platinum foil

1.2.1.1 XANES

In the XANES region when the energy of incident photon is less than E_0 , which is the energy of the core ionization potential and the absorption threshold, discrete transition occurs to the unoccupied valence states. If energy of incident photon E is $E_0 < E < E_C$, it is continuum XANES. E_C is the energy where the wavelength of initially excited photoelectron conforms to the interatomic distance. XANES extends over an energy range of some tens of electron-volts above E_0 approximately 50 eV. In XANES region 8 eV from E_0 the symmetry of the unoccupied electronic states and the effective atomic charge on the absorbing atom can be determined. In specific cases as Pt L_{III} edge, strong absorption called white line is observed. Therefore data processing of the white line reveals the oxidation states or electron transfer by alloying as described in section 1.1.3. On the other hand 8 to 50 eV from E_0 the excited electron is backscattered many times within the system surrounding the central atom due to high backscattering probability at low k values, which is wave number. Therefore multiple scattering events become dominant in the XANES spectra.

1.2.1.2 EXAFS

In the EXAFS region incident photon whose energy $h\nu$ exceeds the core state binding energy E_B ejects photoelectron. The ejected photoelectron has the energy $E = h\nu - E_B$ relative to the Fermi level of the sample. The binding energy of core levels are separated by a large energy range, therefore X-ray absorption spectrum concerns specific core level of a specific atom. The photoelectron ejected by the absorption travels as a spherical wave with the wavelength of $2\pi/k$. When excited atom is surrounded by other atoms the outgoing spherical photoelectron wave is scattering back towards the p. The phase of the reflected wave depends on the photoelectron wavelength and the atomic number of the scatters. The reflected phase shifted wave undergoes interference with the outgoing waves from the emitter. Quantum mechanically this photoelectron interference effect in the final states modifies the

absorption cross section and result in modulation of transmitted X-ray intensity over a range of 50-1500 eV. The resulting modulation is so called EXAFS. The amplitude of modulation depends on the atomic number and backscattering strength of the neighboring atoms and the distance from absorbing atom. Then the resulting modulation, sinusoidal oscillation is processed along the theoretical equations. The detailed analysis methods of EXAFS oscillation is described in section 3.2.4.

1.2.2 X-ray absorption fine structure analysis on PEFC electrocatalyst

In situ XAFS has been employed to investigate several types of catalysts including electrocatalysts because of the large penetration ability of X-rays.¹¹ Such studies have revealed catalytic properties and reaction mechanisms based on dynamic structural changes.^{12,13,14} Hence XAFS is a powerful technique that can be used to study atomic level dynamic structural changes also in an electrochemical environment.

The XAFS study on PEFC electrocatalyst is divided broadly to 2 categories from the standpoint of spectroelectrochemical cell. One is the study using electrochemical cell with three electrodes.¹⁵⁻²⁴ Another is the study using actual fuel cell including polymer electrolyte membrane as Nafion.²⁵⁻³¹ Former cell is favorable for accurate control of electrochemical potential. Latter is favorable to study the properties of electrocatalyst in real world of FC stack.

As an example of the former categories, Mukerjee *et al.* studied several types of Pt and Pt alloy electrocatalyst to clarify the correlation between ORR activity and structure, Pt 5d vacancy of electrocatalyst.²⁴ They reported that there is the appropriate Pt-Pt distance contraction, increase of Pt 5d vacancy from typical Pt nanoparticle to achieve the enhancement of the area specific activity. Sasaki *et al.* studied Pt shell Pd core core-shell electrocatalyst and applied XAFS analysis to confirm the core-shell structure from the determined coordination numbers.²³ In addition the determined Pt-Pt distance of the Pt shell was compared with the typical Pt electrocatalyst and concluded as an origin of enhanced activity. Especially for the structural analysis of core-shell

electrocatalysts XAFS is useful because the XRD does not give any information of Pt shell because the Pt shell is too thin to give the diffraction pattern. Adzic *et al.* utilized the XANES to know the oxidation state of several types of electrocatalysts at the potential around 1.0 V vs. reversible hydrogen electrode (RHE).³² They reported that the electrocatalyst showed slight oxidation with enhanced activity because of the decreased oxide blocks of ORR reaction sites.

On the other hand Tada *et al.* studied the reaction kinetics of surface structural changes of the Pt/C electrocatalyst using time-gating quick XAFS (QXAFS) technique with 1 second time resolution and an energy-dispersive XAFS (DXAFS) system with 4 milliseconds time resolution.²⁸ They reported the significant time lag between electron transfer and the structural change. Successively to reveal the difference of structural kinetics between Pt electrocatalyst and PtCo alloy electrocatalyst, Ishiguro *et al.* studied using QXAFS.²⁹ They reported the increases of reaction rate constants for the reduction processes of Pt-O bond breaking, Pt-Pt bond reformation in PtCo electrocatalyst which showed higher activity comparing with Pt. Greco *et al.* studied structural change of PtCo alloy electrocatalyst before and after controlled potential cycles using XAFS, and reported enhancement of ORR activity through the surface structural modification of nanoparticles.³⁰

As described above XAFS can reveal the dynamic or static structures and electronic states including oxidation states of electrocatalysts at atomic scale under controlled electrochemical potentials and it is valuable to understand the ORR kinetics, activity governing factors and the origin of enhanced activity.

1.3 Review of PEFC electrocatalyst

1.3.1 Pt electrocatalyst

Typical electrocatalyst is the Pt nanoparticles loaded on carbon support as shown in Figure 1.5. The diameter of Pt particles is 2 to 3 nm. Typical carbon support is Ketjenblack which has high specific surface area and approximately 30 to 50 nm diameter.

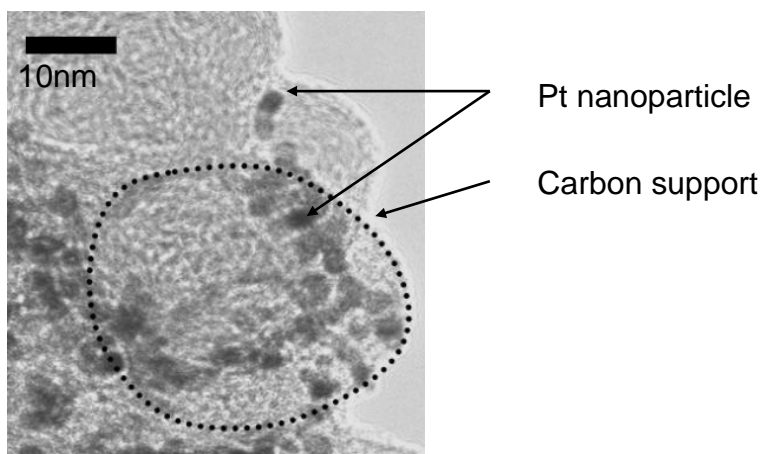


Figure 1.5 Transmission electron microscope (TEM) micrograph of Pt electrocatalyst supported on carbon

1.3.2 Core-shell Electrocatalyst

In recent years, core-shell type electrocatalysts have drawn wide attentions to improve the Pt mass-specific activity.³²

One effective typical core-shell electrocatalyst consists of a Au core and a Pt shell supported on a carbon substrate.^{8,31,33-40} In Pt/Au core-shell electrocatalysts, both the mass-specific activity and area-specific activity are enhanced with respect to the Pt nanoparticle electrocatalyst, which indicates the effectiveness of the core-shell structure to not only increase of the Pt fraction on the surface of the electrocatalyst particle (geometric effect), but also to modify the Pt electronic state (electronic effect). The latter can be achieved by electron transfer and/or lattice contraction/expansion induced by interactions between the Au core and the Pt shell. According to Mukerjee *et al.*⁴¹

contraction of Pt-Pt distance and the increase of Pt 5d vacancy are the origin of enhanced activity. However area specific activity improvement of Pt/Au/C is not understandable. Because considering the Au lattice, the Pt-Pt distance of the Pt shell in a Pt/Au core-shell electrocatalyst is expected to be longer than that in a simple Pt electrocatalyst. In fact surface X-ray diffraction analysis has revealed that the Pt-Pt distance in a Pt monolayer deposited on the Au (111) surface is elongated.⁴² Area specific activity of Pt/Au core-shell was approximately 2 times higher than that of Pt/C according to Shao *et al.*³⁹ The reason of activity improvement was considered to be the contraction of Pt-Pt atomic distance induced by the contraction of Au-Au distance of Au core induced by existence as a nanocluster. However Pt-Pt distance of Pt shell on Au core is not understandable to be shorter than that of typical Pt nanocluster from their report. Hence the reason of activity improvement of Pt/Au core-shell remains still elusive. To clarify the activity governing factor direct measurement of Pt-Pt distance of Pt/Au/C is desirable.

Another intensively studied core-shell electrocatalyst is Pd core Pt shell supported on carbon.^{23,43,44,45} According to Sasaki *et al.*²³ 4 to 5 times enhancement of mass specific activity was reported including the scale up synthesis method and the contraction of Pt-Pt distance of Pt shell was determined by the EXAFS analysis. The reason of activity enhancement was considered to be the contraction of Pt-Pt distance. Pd core slightly Au added and Pt shell electrocatalyst was also reported for the improvement of the stability in the potential cycling.⁴⁴

Although catalytic activity per Pt mass was improved from the typical Pt/C electrocatalysts by core-shell structure as described above, noble metals such as Au or Pd are still used in the core. Hence the activity per noble metal cost was not improved drastically.

1.3.3 Pt alloy electrocatalyst

On the other hand binary and ternary Pt alloy electrocatalysts (PtM) where Pt and M

(other metal except for Pt) are randomly mixed or intermetallic structure have been investigated to enhance the activity. 3d transition metal atoms are used for additives such as PtNi, PtCo, PtMn, PtFe, PtCr, PtCoCr, and PtVCr. They have been reported to have the higher ORR activity than Pt/C electrocatalyst has.⁴⁶⁻⁵⁷ One advantage of PtM alloy electrocatalyst is reduction of Pt usage as core-shell structure. In addition some of the PtM electrocatalysts show much higher area specific and mass specific activities than core-shell electrocatalysts.⁵⁶ Mukerjee *et al.* investigated correlation between ORR activity and Pt-Pt distances and Pt 5d vacancy of highly ordered L1₂ intermetallic as PtMn, PtCo, PtFe, PtNi, PtCr nanoparticles by *in situ* XAFS analysis. They reported volcano-plot of the area specific activity for Pt-Pt distance and Pt 5d vacancy.⁴⁷ In addition intermetallic structure was thought to be effective to induce the contraction of Pt-Pt distance and improve the activity.

Among several kinds of alloy electrocatalysts PtCo alloyed electrocatalyst is most intensively investigated electrocatalyst. Xiong *et al.* investigated the correlation between Co concentration of PtCo ordered alloy electrocatalyst and extent of ordering determined from the intermetallic diffraction peak obtained by the *ex situ* XRD pattern.⁴⁸ They again claimed volcano relationship between Pt-Pt distance and activity or extent of ordering. According to them increase of the extent of ordering was predominant to enhance the ORR area specific activity as reported by Mukerjee *et al.*⁴⁷ Koh *et al.* prepared L1₂ ordered heat treated PtCo, and mixed of PtCo L1₀ ordered and disordered electrocatalyst.⁴⁹ The intermetallic structure of L1₂ and L1₀ are shown in Figure 1.6. L1₂ structure of Pt₃M has a cubic structure in which the M atoms occupy all corner positions and the Pt atoms occupy all the face centered positions. L1₀ structure of PtM shows tetragonal structure where Pt and Co atoms occupy the alternate (001) planes. They studied not only the initial ORR activity but also durability. The ordered PtCo, showed the higher ORR specific activity than that of disorder PtCo. However ordered PtCo electrocatalyst showed lower durability than disorder PtCo electrocatalyst. Wanjala *et al.* prepared PtVCo ternary electrocatalysts changing heat

treatment temperatures from 400 to 900 degree and conducted structural and electrochemical analysis.⁵³ They reported the detrimental effect on the activity by the excess structural ordering by the heat treatment at more than 700 °C. Wang *et al.* prepared the completely intermetallic ordered Pt₃Co core and Pt-shell electrocatalyst by heat treatment at 700 °C which showed 10 times higher specific activity than Pt/C, whereas the ordered alloy electrocatalyst showed higher durability than disordered structure.⁵⁶ This result conflicts with the durability test of the Koh *et al.*⁴⁹ Jia *et al.* prepared the Pt₁Co₁, L1₀ ordered electrocatalyst and conducted the structural analysis with EXAFS.⁵⁸ The origin of enhanced activity was concluded to be the contraction of Pt-Pt distance and the ligand effect of Co subsurface induced by the Pt₁Co₁ specific structure.

On the other hand PtCu alloy electrocatalysts are also intensively studied. For example surface Pt rich PtCu alloy core electrocatalysts were reported.⁵⁹⁻⁶² The specific activity of Pt₂₅Cu₇₅ reported by Mani *et al.* showed 12 times higher than that of typical Pt/C electrocatalyst.⁵⁹ The structure of prepared PtCu alloys were studied with XRD and clarified as similar disorder face-centered-cubic (FCC). The origin of high activity was considered to be the surface roughening and its geometric and electronic effects as candidates.

In the meanwhile according to Stamenkovic *et al.* PtNi electrocatalyst is also expected to enhance notably the area specific activity.⁶³ The area specific activity of Pt₃Ni (111) flat model electrode was 10 times higher than that of the Pt (111) single crystal flat electrode. They discussed the origin of enhanced activity combining with d band center and concluded that the origin of enhanced activity was the downshift of d-band center of Pt₃Ni (111). Wang *et al.* reported core shell electrocatalyst which consisted of the multilayer Pt shell and PtNi alloy core.⁶⁴ The enhancement of area specific activity comparing with the Pt/C was 6.5 times. Although they conducted *in situ* XANES analysis combining with STEM and XRD, EXAFS structural analysis was not conducted and the correlation with Pt-Pt distance and area specific activity has not

been reported. Loukrakpam *et al.* reported PtNi/C and PtCo/C with changing Pt/Ni or Pt/Co atomic ratio.⁶⁵ The area specific activity of PtNi/C was enhanced 3 times than that of Pt/C. However PtCo/C and PtNi/C showed the same area specific activity in spite of large difference in Pt-Pt distances. There is some conflict with the result of Mukerjee *et al.*^{47,48,49,58} They concluded the activity enhancement is induced by the combination of Pt-Pt distance, surface segregation and the size of the particles.

From the researches as described above area specific and mass specific activities of Pt electrocatalysts alloyed especially with Co, Cu, Ni, 3d transition metals are thought to be drastically improved and the durability would be also changed. However the relation between structural parameters as Pt-Pt distances, internal structure of the alloyed nanoparticle as intermetallic or random, concentration of added metal and its electrochemical properties as activity and durability still remain elusive.

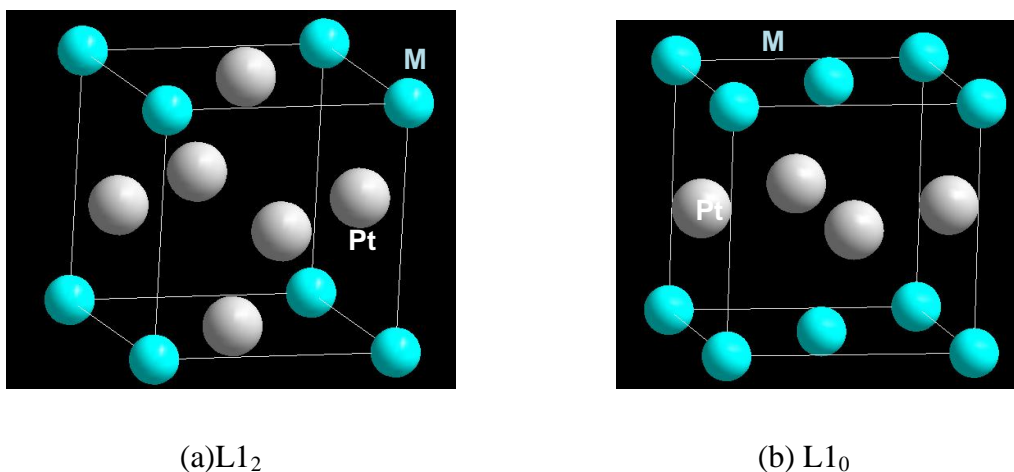


Figure 1.6 $L1_2$ (a) and $L1_0$ (b) intermetallic structure of PtM

1.4 Objectives and outline of this research

In this study several types of electrocatalysts were prepared to make correlation between Pt-Pt distances, electronic states, shapes, inner structures, added metals, concentration of added metals and the ORR activities to know the activity governing factor.

In chapter 2, the detail of newly developed spectroelectrochemical cell suitable for Pt and Au K-edge *in situ* XAFS measurements is described, which allows us to control the potential finely precisely. The *in situ* Pt and Au K-edge XAFS spectra provided us information about bimetallic nanoparticle structure.

In chapter 3, preparation method of Pt/Au/C core-shell electrocatalyst, characterization including structural analysis of XAFS spectra of Pt/Au/C core-shell electrocatalyst obtained with the cell described in chapter 2 are explained. It was determined that area specific activity of prepared Pt/Au/C was twice than that of Pt/C by the rotating disk electrode (RDE) electrochemical testing method. The origin of activity improvement of Pt/Au/C is discussed from the EXAFS structural parameters.

In chapter 4, to clarify the correlation of Pt-Pt distance and area specific activity, several types of, inner structure of, alloyed elements of, alloyed element ratio of electrocatalysts were prepared and characterized. In particular randomly-mixed alloy Pt₅Co/C, Pt₃Cu/C, Pt₉Ni/C without heat treatment and heat treated Pt₃Co/C, Pt₂Co/C and Pt₃Cu/C was prepared changing the heat treatment temperature, the inner structures such as bond distance and coordination numbers. Among them randomly-mixed heat treated alloy Pt₂Co/C showed approximately 10 times higher area specific activity than that of Pt/C. The structures of prepared electrocatalysts were determined by EXAFS curve fitting analysis combining with XRD, STEM, High-Angle-Annular-Dark-Field (HAADF). Then activity governing factor is discussed using those structural parameters.

In chapter 5 I provide general discussions and general conclusions for this thesis.

1.5 References

- ¹ Larminie, J.; Dicks, A., Fuel Cell Systems Explained. J. Wiley: 2003.
- ² Srinivasan, S., Fuel Cells. Springer: 2006.
- ³ Gasteiger, H. A.; Kocha, S. S.; Sompalli, B.; Wagner, F. T., Activity benchmarks and requirements for Pt, Pt-alloy, and non-Pt oxygen reduction catalysts for PEMFCs. *Applied Catalysis B: Environmental* 2005, 56 (1–2), 9-35.
- ⁴ ; J. Sinha et al., “Direct Hydrogen PEMFC Manufacturing Cost Estimation for Automotive Applications”, DOE Hydrogen Program Review/USA, Project ID #FC_31_Sinha, May 21, 2009
- ⁵ Bockris, J. O. M., *Comprehensive treatise of electrochemistry. Vol. 7. Kinetics and mechanisms of electrode processes*. Plenum: 1983.
- ⁶ Lipkowski, J.; Ross, P. N., *Electrocatalysis*. Wiley-VCH: 1998.
- ⁷ Gottesfeld, S.; Zawodzinski, T. A., Polymer Electrolyte Fuel Cells. In *Advances in Electrochemical Science and Engineering*, Wiley-VCH Verlag GmbH: 2008; pp 195-301.
- ⁸ Brankovic, S. R.; Wang, J. X.; Adzic, R. R., New methods of controlled monolayer-to-multilayer deposition of Pt for designing electrocatalysts at an atomic level. *Journal of the Serbian Chemical Society* 2001, 66 (11-12), 887-898.
- ⁹ Wang, J. X.; Markovic, N. M.; Adzic, R. R., Kinetic Analysis of Oxygen Reduction on Pt(111) in Acid Solutions: Intrinsic Kinetic Parameters and Anion Adsorption Effects. *The Journal of Physical Chemistry B* 2004, 108 (13), 4127-4133.
- ¹⁰ Bart, J. C. J.; Vlaic, G., Extended X-Ray Absorption Fine Structure Studies in Catalysis. In *Advances in Catalysis*, D.D. Eley, H. P.; Paul, B. W., Eds. Academic Press: 1987; Vol. Volume 35, pp 1-138.
- ¹¹ Lytle, F. W.; Via, G. H.; Sinfelt, J. H., New application of extended x-ray absorption fine structure (EXAFS) as a surface probe-nature of oxygen interaction with a ruthenium catalyst. *The Journal of Chemical Physics* 1977, 67(8), 3831-3832.
- ¹² van 't Blik, H. F. J.; Prins, R., Characterization of supported cobalt and cobalt-rhodium catalysts: I. Temperature-programmed reduction (TPR) and oxidation (TPO) of Co · RhAl₂O₃. *Journal of Catalysis* 1986, 97(1), 188-199.
- ¹³ Iwasawa, Y.; Asakura, K.; Ishii, H.; Kuroda, H., Dynamic Behaviour of Active Sites of a SiO₂-Attached Mo(VI)-Dimer Catalyst during Ethanol Oxidation Observed by Means of EXAFS. *Zeitschrift für Physikalische Chemie* 1985, 144 (144), 105-115.
- ¹⁴ Asakura, K.; Kitamura-Bando, K.; Isobe, K.; Arakawa, H.; Iwasawa, Y., Metal-assisted CO insertion reaction on a new surface rhodium dimer catalyst observed by an in situ EXAFS technique. *Journal of the American Chemical Society* 1990, 112(8), 3242-3244.
- ¹⁵ Yoshitake, H.; Mochizuki, T.; Yamazaki, O.; Ota, K.-i., Study of the density of the d-state and structure transformation of Pt fine particles dispersed on carbon electrodes by in situ X-ray absorption spectroscopy. *Journal of Electroanalytical Chemistry* 1993, 361 (1-2), 229-237.
- ¹⁶ Yoshitake, H.; Yamazaki, O.; Ota, K.-i., Novel spectroelectrochemical cell for in-situ XAFS spectroscopy on gas generating electrodes. *Ibid.* 1994, 371, 287-290.
- ¹⁷ Mukerjee, S.; Srinivasan, S.; Soriaga, M. P.; McBreen, J., Effect of Preparation Conditions of Pt Alloys on Their Electronic, Structural, and Electrocatalytic Activities for Oxygen Reduction - XRD, XAS, and Electrochemical Studies. *The Journal of Physical Chemistry* 1995, 99 (13), 4577-4589.
- ¹⁸ McBreen, J.; Mukerjee, S., In Situ X-Ray Absorption Studies of a Pt-Ru Electrocatalyst. *Journal of The Electrochemical Society* 1995, 142 (10), 3399-3404.
- ¹⁹ Mukerjee, S.; McBreen, J., Effect of particle size on the electrocatalysis by carbon-supported Pt electrocatalysts: an in situ XAS investigation. *Journal of Electroanalytical Chemistry* 1998, 448 (2), 163-171.

-
- ²⁰ Maniguet, S.; Mathew, R. J.; Russell, A. E., EXAFS of Carbon Monoxide Oxidation on Supported Pt Fuel Cell Electrocatalysts. *The Journal of Physical Chemistry B* **2000**, *104* (9), 1998-2004.
- ²¹ Russell, A. E.; Rose, A., X-ray Absorption Spectroscopy of Low Temperature Fuel Cell Catalysts. *Chemical Reviews* **2004**, *104* (10), 4613-4636.
- ²² Imai, H.; Izumi, K.; Matsumoto, M.; Kubo, Y.; Kato, K.; Imai, Y., In Situ and Real-Time Monitoring of Oxide Growth in a Few Monolayers at Surfaces of Platinum Nanoparticles in Aqueous Media. *Journal of the American Chemical Society* **2009**, *131* (17), 6293-6300.
- ²³ Sasaki, K.; Wang, J. X.; Naohara, H.; Marinkovic, N.; More, K.; Inada, H.; Adzic, R. R., Recent advances in platinum monolayer electrocatalysts for oxygen reduction reaction: Scale-up synthesis, structure and activity of Pt shells on Pd cores. *Electrochimica Acta* **2010**, *55* (8), 2645-2652.
- ²⁴ Mukerjee, S.; Srinivasan, S.; Soriaga, M. P.; McBreen, J., Role of Structural and Electronic Properties of Pt and Pt Alloys on Electrocatalysis of Oxygen Reduction. *Journal of The Electrochemical Society* **1995**, *142* (5), 1409-1422.
- ²⁵ Allen, P. G.; Conradson, S. D.; Wilson, M. S.; Gottesfeld, S.; Raistrick, I. D.; Valerio, J.; Lovato, M., In situ structural characterization of a platinum electrocatalyst by dispersive x-ray absorption spectroscopy. *Electrochimica Acta* **1994**, *39* (16), 2415-2418.
- ²⁶ Allen, P. G.; Conradson, S. D.; Wilson, M. S.; Gottesfeld, S.; Raistrick, I. D.; Valerio, J.; Lovato, M., Direct observation of surface oxide formation and reduction on platinum clusters by time-resolved X-ray absorption spectroscopy. *Journal of Electroanalytical Chemistry* **1995**, *384* (1-2), 99-103.
- ²⁷ Wiltshire, R. J. K.; King, C. R.; Rose, A.; Wells, P. P.; Hogarth, M. P.; Thompsett, D.; Russell, A. E., A PEM fuel cell for in situ XAS studies. *Electrochimica Acta* **2005**, *50* (25-26), 5208-5217.
- ²⁸ Tada, M.; Murata, S.; Asakoka, T.; Hiroshima, K.; Okumura, K.; Tanida, H.; Uruga, T.; Nakanishi, H.; Matsumoto, S.-i.; Inada, Y.; Nomura, M.; Iwasawa, Y., In Situ Time-Resolved Dynamic Surface Events on the Pt/C Cathode in a Fuel Cell under Operando Conditions. *Angewandte Chemie* **2007**, *119* (23), 4388-4393.
- ²⁹ Ishiguro, N.; Saida, T.; Uruga, T.; Nagamatsu, S.-i.; Sekizawa, O.; Nitta, K.; Yamamoto, T.; Ohkoshi, S.-i.; Iwasawa, Y.; Yokoyama, T.; Tada, M., Operando Time-Resolved X-ray Absorption Fine Structure Study for Surface Events on a Pt₃Co/C Cathode Catalyst in a Polymer Electrolyte Fuel Cell during Voltage-Operating Processes. *ACS Catalysis* **2012**, 1319-1330.
- ³⁰ Greco, G.; Witkowska, A.; Minicucci, M.; Olivi, L.; Principi, E.; Dsoke, S.; Moretti, A.; Marassi, R.; Di Cicco, A., Local Ordering Changes in Pt-Co Nanocatalyst Induced by Fuel Cell Working Conditions. *The Journal of Physical Chemistry C* **2012**, *116* (23), 12791-12802.
- ³¹ Nagamatsu, S.-i.; Arai, T.; Yamamoto, M.; Ohkura, T.; Oyanagi, H.; Ishizaka, T.; Kawanami, H.; Uruga, T.; Tada, M.; Iwasawa, Y., Potential-Dependent Restructuring and Hysteresis in the Structural and Electronic Transformations of Pt/C, Au(Core)-Pt(Shell)/C, and Pd(Core)-Pt(Shell)/C Cathode Catalysts in Polymer Electrolyte Fuel Cells Characterized by in Situ X-ray Absorption Fine Structure. *Ibid.* **2013**, *117* (25), 13094-13107.
- ³² Adzic, R. R.; Zhang, J.; Sasaki, K.; Vukmirovic, M. B.; Shao, M.; Wang, J. X.; Nilekar, A. U.; Mavrikakis, M.; Valerio, J. A.; Uribe, F., Platinum Monolayer Fuel Cell Electrocatalysts. *Topics in Catalysis* **2007**, *46* (3-4), 249-262.
- ³³ 32. Kristian, N.; Wang, X., Ptshell-AuCore/C electrocatalyst with a controlled shell thickness and improved Pt utilization for fuel cell reactions. *Electrochemistry Communications* **2008**, *10* (1), 12-15.
- ³⁴ Wang, S.; Kristian, N.; Jiang, S.; Wang, X., Controlled synthesis of dendritic Au@Pt

core-shell nanomaterials for use as an effective fuel cell electrocatalyst.

Nanotechnology **2009**, *20* (2), 025605.

³⁵ Luo, J.; Wang, L.; Mott, D.; Njoki, P. N.; Lin, Y.; He, T.; Xu, Z.; Wanjana, B. N.; Lim, I. I. S.; Zhong, C.-J., Core/Shell Nanoparticles as Electrocatalysts for Fuel Cell Reactions. *Advanced Materials* **2008**, *20* (22), 4342-4347.

³⁶ Zhang, J.; Lima, F. H. B.; Shao, M. H.; Sasaki, K.; Wang, J. X.; Hanson, J.; Adzic, R. R., Platinum Monolayer on Nonnoble Metal–Noble Metal Core–Shell Nanoparticle Electrocatalysts for O₂ Reduction. *The Journal of Physical Chemistry B* **2005**, *109* (48), 22701-22704.

³⁷ Xiu, C.; Shengnan, W.; Scott, J.; Zhibing, C.; Zhenghua, W.; Lun, W.; Yongxin, L., The Deposition of Au–Pt Core–Shell Nanoparticles on Reduced Graphene Oxide and their Catalytic Activity. *Nanotechnology* **2013**, *24*, 295402.

³⁸ Inaba, M.; Tsuji, H., Platinum Core-Shell Catalyst Manufacturing Method, and Fuel Cell using Catalyst, Japan Patent, WO2011115012 A1, March 19 2010.

³⁹ Shao, M.; Peles, A.; Shoemaker, K.; Gummalla, M.; Njoki, P. N.; Luo, J.; Zhong, C.-J., Enhanced Oxygen Reduction Activity of Platinum Monolayer on Gold Nanoparticles. *The Journal of Physical Chemistry Letters* **2010**, *2* (2), 67-72.

⁴⁰ Xing, Y.; Cai, Y.; Vukmirovic, M. B.; Zhou, W.-P.; Karan, H.; Wang, J. X.; Adzic, R. R., Enhancing Oxygen Reduction Reaction Activity via Pd–Au Alloy Sublayer Mediation of Pt Monolayer Electrocatalysts. *Ibid.* *1* (21), 3238-3242.

⁴¹ Mukerjee, S.; Srinivasan, S., Enhanced electrocatalysis of oxygen reduction on platinum alloys in proton exchange membrane fuel cells. *Journal of Electroanalytical Chemistry* **1993**, *357* (1–2), 201-224.

⁴² Shibata, M.; Hayashi, N.; Sakurai, T.; Kurokawa, A.; Fukumitsu, H.; Masuda, T.; Uosaki, K.; Kondo, T., Electrochemical Layer-by-Layer Deposition of Pseudomorphic Pt Layers on Au(111) Electrode Surface Confirmed by Electrochemical and In Situ Resonance Surface X-ray Scattering Measurements. *The Journal of Physical Chemistry C* **2012**, *116* (50), 26464-26474.

⁴³ Sasaki, K.; Naohara, H.; Cai, Y.; Choi, Y. M.; Liu, P.; Vukmirovic, M. B.; Wang, J. X.; Adzic, R. R., Core-Protected Platinum Monolayer Shell High-Stability Electrocatalysts for Fuel-Cell Cathodes. *Angewandte Chemie International Edition* **2010**, *49* (46), 8602-8607.

⁴⁴ Xing, Y.; Cai, Y.; Vukmirovic, M. B.; Zhou, W.-P.; Karan, H.; Wang, J. X.; Adzic, R. R., Enhancing Oxygen Reduction Reaction Activity via Pd–Au Alloy Sublayer Mediation of Pt Monolayer Electrocatalysts. *The Journal of Physical Chemistry Letters* **2010**, *1* (21), 3238-3242.

⁴⁵ Lima, F.; Zhang, J.; Shao, M.; Sasaki, K.; Vukmirovic, M.; Ticianelli, E.; Adzic, R., Pt monolayer electrocatalysts for O₂ reduction: PdCo/C substrate-induced activity in alkaline media. *Journal of Solid State Electrochemistry* **2008**, *12* (4), 399-407.

⁴⁶ Mukerjee, S.; Srinivasan, S., Enhanced electrocatalysis of oxygen reduction on platinum alloys in proton exchange membrane fuel cells. *Journal of Electroanalytical Chemistry* **1993**, *357* (1–2), 201-224.

⁴⁷ Mukerjee, S.; Srinivasan, S.; Soriaga, M. P.; McBreen, J., Role of Structural and Electronic Properties of Pt and Pt Alloys on Electrocatalysis of Oxygen Reduction. *Journal of The Electrochemical Society* **1995**, *142* (5), 1409-1422.

⁴⁸ Xiong, L.; Manthiram, A., Influence of atomic ordering on the electrocatalytic activity of Pt–Co alloys in alkaline electrolyte and proton exchange membrane fuel cells. *Journal of Materials Chemistry* **2004**, *14* (9), 1454-1460.

⁴⁹ Koh, S.; Toney, M. F.; Strasser, P., Activity–stability relationships of ordered and disordered alloy phases of Pt₃Co electrocatalysts for the oxygen reduction reaction (ORR). *Electrochimica Acta* **2007**, *52* (8), 2765-2774.

-
- ⁵⁰ Chen, S.; Sheng, W.; Yabuuchi, N.; Ferreira, P. J.; Allard, L. F.; Shao-Horn, Y., Origin of Oxygen Reduction Reaction Activity on “Pt₃Co” Nanoparticles: Atomically Resolved Chemical Compositions and Structures. *The Journal of Physical Chemistry C* **2008**, *113* (3), 1109-1125.
- ⁵¹ Jeon, M. K.; Zhang, Y.; McGinn, P. J., A comparative study of PtCo, PtCr, and PtCoCr catalysts for oxygen electro-reduction reaction. *Electrochimica Acta* **2010**, *55* (19), 5318-5325.
- ⁵² Rao, C. S.; Singh, D. M.; Sekhar, R.; Rangarajan, J., Pt–Co electrocatalyst with varying atomic percentage of transition metal. *International Journal of Hydrogen Energy* **2011**, *36* (22), 14805-14814.
- ⁵³ Wanjala, B. N.; Fang, B.; Shan, S.; Petkov, V.; Zhu, P.; Loukrakpam, R.; Chen, Y.; Luo, J.; Yin, J.; Yang, L.; Shao, M.; Zhong, C.-J., Design of Ternary Nanoalloy Catalysts: Effect of Nanoscale Alloying and Structural Perfection on Electrocatalytic Enhancement. *Chemistry of Materials* **2012**, *24* (22), 4283-4293.
- ⁵⁴ Jeon, M. K.; McGinn, P. J., Co-alloying effect of Co and Cr with Pt for oxygen electro-reduction reaction. *Electrochimica Acta* **2012**, *64* (0), 147-153.
- ⁵⁵ Oezaslan, M.; Hasché, F.; Strasser, P., Oxygen Electroreduction on PtCo₃, PtCo and Pt₃Co Alloy Nanoparticles for Alkaline and Acidic PEM Fuel Cells. *Journal of The Electrochemical Society* **2012**, *159* (4), B394-B405.
- ⁵⁶ Wang, D.; Xin, H. L.; Hovden, R.; Wang, H.; Yu, Y.; Muller, D. A.; DiSalvo, F. J.; Abruña, H. D., Structurally ordered intermetallic platinum–cobalt core–shell nanoparticles with enhanced activity and stability as oxygen reduction electrocatalysts. *Nat Mater* **2013**, *12* (1), 81-87.
- ⁵⁷ Lima, F. H. B.; de Castro, J. F. R.; Santos, L. G. R. A.; Ticianelli, E. A., Electrocatalysis of oxygen reduction on carbon-supported Pt–Co nanoparticles with low Pt content. *Journal of Power Sources* **2009**, *190* (2), 293-300.
- ⁵⁸ Jia, Q.; Caldwell, K.; Ramaker, D. E.; Ziegelbauer, J. M.; Liu, Z.; Yu, Z.; Trahan, M.; Mukerjee, S., In Situ Spectroscopic Evidence for Ordered Core–Ultrathin Shell Pt₁Co₁ Nanoparticles with Enhanced Activity and Stability as Oxygen Reduction Electrocatalysts. *The Journal of Physical Chemistry C* **2014**, *118* (35), 20496-20503.
- ⁵⁹ Mani, P.; Srivastava, R.; Strasser, P., Dealloyed Pt–Cu Core–Shell Nanoparticle Electrocatalysts for Use in PEM Fuel Cell Cathodes. *Ibid.* **2008**, *112* (7), 2770-2778.
- ⁶⁰ Yu, Z.; Zhang, J.; Liu, Z.; Ziegelbauer, J. M.; Xin, H.; Dutta, I.; Muller, D. A.; Wagner, F. T., Comparison between Dealloyed PtCo₃ and PtCu₃ Cathode Catalysts for Proton Exchange Membrane Fuel Cells. *Ibid.* **2012**, *116* (37), 19877-19885.
- ⁶¹ Xu, Z.; Zhang, H.; Liu, S.; Zhang, B.; Zhong, H.; Su, D. S., Facile synthesis of supported Pt–Cu nanoparticles with surface enriched Pt as highly active cathode catalyst for proton exchange membrane fuel cells. *International Journal of Hydrogen Energy* **2012**, *37* (23), 17978-17983.
- ⁶² Marcu, A.; Toth, G.; Srivastava, R.; Strasser, P., Preparation, characterization and degradation mechanisms of PtCu alloy nanoparticles for automotive fuel cells. *Journal of Power Sources* **2012**, *208* (0), 288-295.
- ⁶³ Stamenkovic, V. R.; Fowler, B.; Mun, B. S.; Wang, G.; Ross, P. N.; Lucas, C. A.; Marković, N. M., Improved Oxygen Reduction Activity on Pt₃Ni(111) via Increased Surface Site Availability. *Science* **2007**, *315* (5811), 493-497.
- ⁶⁴ Wang, C.; Chi, M.; Li, D.; Strmcnik, D.; van der Vliet, D.; Wang, G.; Komanicky, V.; Chang, K.-C.; Paulikas, A. P.; Tripkovic, D.; Pearson, J.; More, K. L.; Markovic, N. M.; Stamenkovic, V. R., Design and Synthesis of Bimetallic Electrocatalyst with Multilayered Pt–Skin Surfaces. *Journal of the American Chemical Society* **2011**, *133* (36), 14396-14403.
- ⁶⁵ Loukrakpam, R.; Luo, J.; He, T.; Chen, Y.; Xu, Z.; Njoki, P. N.; Wanjala, B. N.; Fang, B.; Mott, D.; Yin, J.; Klar, J.; Powell, B.; Zhong, C.-J., Nanoengineered PtCo and PtNi

Catalysts for Oxygen Reduction Reaction: An Assessment of the Structural and Electrocatalytic Properties. *The Journal of Physical Chemistry C* **2011**, *115*(5), 1682-1694.



Chapter 2

Development of spectroelectrochemical cell for
in-situ XAFS experiment

2.1 Introduction

In recent years, core-shell type electrocatalysts have drawn wide attention for improvement in the mass-specific activity of Pt.¹ One effective core-shell electrocatalyst consists of a Au core and a Pt shell supported on a carbon substrate.²⁻¹⁰ In Pt/Au core-shell electrocatalysts, both the mass-specific activity and area-specific activity are increased with respect to the Pt nanoparticle electrocatalyst, which indicates the effectiveness of the core-shell structure to not only increase the Pt fraction on the surface of the electrocatalyst particle (geometric effect), but also to modify the Pt electronic state (electronic effect). The latter can be achieved by electron transfer and/or lattice contraction/expansion induced by interactions between the Au core and the Pt shell. However, it is difficult to directly determine the core-shell structure if the Pt shell thickness is as small as one or two monolayers. Considering the Au lattice, the Pt-Pt distance of the Pt shell in a Pt/Au core-shell electrocatalyst is expected to be longer than that in a simple Pt electrocatalyst. Surface X-ray diffraction analysis has revealed that the Pt-Pt distance in a Pt monolayer deposited on the Au (111) surface is elongated.¹¹ Core-shell structures and lattice mismatch can be determined directly using XAFS. Although XAFS is the most suitable technique to investigate the core-shell structures of nanoclusters and their bond distances, interference between the Pt and Au L_{III} X-ray absorption edges hinders XAFS studies on Pt and Au bimetallic nanoclusters. The separation of the Pt and Au L_{III}-edges is only approximately 400 eV, which results in overlapping of EXAFS oscillation. Hence reliable curve fitting analysis of the Pt and Au L_{III} edges becomes difficult.^{7,12} If Pt and Au K-edge XAFS analyses can be performed, we can obtain well separated Pt and Au spectra (Pt and Au K-edges are located at 78.4 and 80.7 keV, respectively), although this had been considered to be impossible due to machine limitations and finite lifetime broadening. After Ce K-edge XAFS was shown to be possible,¹³ the extension of K-edge XAFS measurements to higher energies has progressed. Nishihata *et al.* reported Pt K-edge XAFS measurements¹⁴ and Nagamatsu *et al.* conducted *ex situ* K-edge XAFS

measurements on fuel cell Pt/Au catalysts.¹⁵ Recently Inaba and coworkers claimed that the simple reaction of a Pt precursor with Au nanoparticles on C without a reducing agent and under inert gas flow allows the selective deposition of Pt on the Au nanoparticles to form core-shell structures.^{9,10}

In this thesis I developed the spectroelectrochemical cell suitable for Pt and Au K-edge EXAFS analysis and prepared the carbon supported Pt/Au core-shell electrocatalyst and characterized the electrocatalyst mainly using EXAFS.

In this 2nd chapter the new cell suitable for the Pt and Au K-edges *in situ* XAFS measurements under the electrochemical conditions are described. It is quite difficult to apply the previously-reported electrochemical EXAFS cells for L_{III}-edge measurements to the K-edge measurements,¹⁶ for the following reasons: 1. Ten times larger amount of electrocatalyst is required for the K-edge measurement than that for the L_{III}-edge measurement to obtain a sufficient signal; therefore, a very thick sample, catalyst layer is required, which is fragile and difficult to hold stable. 2. Even if a thick and robust electrocatalyst layer could be formed, electrochemical equilibrium could not be achieved for all of the Pt/Au core-shell electrocatalyst particles in the catalyst layer, owing to electrochemical inhomogeneity caused by slow diffusion of ion species and internal resistance in the thick layer. 3. In addition, the difficulty in potential control of each Pt/Au core-shell electrocatalyst particle would make it impossible to clean the particle surface and remove contamination by the electrochemical oxidation-reduction cycle (ORC) treatment (0.05–1.2 V). Accordingly, a new method and a new spectroelectrochemical cell suitable for Pt and Au K-edge XAFS measurements are required.

Then the detail preparation process of Pt/Au core-shell and the EXAFS analysis of spectra shown in this chapter are described in following chapter 3.

2.2 Basic concepts for the cell design

The requirements necessary for the K-edge XAFS measurements are summarized as follows:

1. A sufficient quantity of the electrocatalyst can be loaded along the optical axis.
2. The catalyst layers must be robust.
3. The potential of all electrocatalysts in the catalyst layer must be controlled homogeneously.

The basic strategy to achieve these requirements is to utilize the low background absorptions of other elements and other lower-energy edges (L, M, ...edges) than the absorption coefficients of the Pt and Au K-edges.¹⁷ Carbon plates coated with the electrocatalyst, an electrolyte solution and Nafion polymers comprise the background absorption; however, they have very low absorption coefficients around 80 keV and become almost negligible. Thin catalyst layers were prepared on both sides of the thin carbon plates, which were then placed in series at specific intervals along the optical axis, as shown in Figure 2.1 and 2.2 described in section 2.3. The gap between electrocatalyst layers facing each other was filled with sufficient electrolyte solution. Consequently, the system could reach equilibrium swiftly against the potential change.

2.3 Experimental

2.3.1 *In situ* electrochemical cell for Pt and Au K-edge EXAFS measurements

Fig. 2.1 shows photographs of the spectroelectrochemical cell developed for Pt and Au K absorption edge XAFS measurements. The white cell body is made of polychlorotrifluoroethylene (PCTFE), which does not corrode in strong acid solution and is mechanically stronger than polytetrafluoroethylene (PTFE). Fig. 2.1 (b) shows a series of fifteen carbon plates inserted in rectangular slots, which were machined on the top of the cell body. The X-ray goes through the recesses of both sides of the carbon plates which are coated with the electrocatalyst layers including electrocatalyst particles, Nafion ionomer and carbon support. The thickness of the electrocatalyst layer is several hundred micrometers, as shown in Fig. 2(b). The carbon plates were used as part of working electrodes. The interval of the carbon plates is 1.8 mm, which is balanced between low ohmic loss and total X-ray absorption limitation due to thick electrolyte solution.

Figure 2.2 (a) and (b) show schematic drawings of the cell and carbon plates that have recesses coated with electrocatalyst layers respectively. Figure 2.3 (a) and (b) show the drawing of the cell and the carbon plate for the formation of electrocatalyst layer respectively. The catalyst layer was prepared according to the following procedure. An electrocatalyst ink was prepared by mixing the carbon-supported electrocatalyst (a typical carbon support is Ketjenblack.), Nafion ionomer, Milli-Q water and isopropyl alcohol under ultrasonication for 30 min. The ink mixture was then dripped homogeneously into the recessed part (Fig. 2.2 (b), Fig. 2.3 (b)) at one side of the carbon plate, followed by drying in an oven at 60 °C. The dripping and drying operations were repeated until a catalyst layer with several hundred micrometers thick was formed. Another electrocatalyst layer was formed on the other side of the plate by the same process. The desired numbers of plates, depending on the amount of electrocatalyst metal loading and thickness of one catalyst layer, were inserted into the cell to obtain a sufficient edge height; approximately fifteen carbon plates coated with

electrocatalyst layers were required. Each of the carbon plates was electrically connected by wire harnesses at a terminal board for application of the same potential to working electrode (WE). Consequently, the Pt loading in the optical path was approximately 70 mg/cm^2 , which could yield an edge height of 0.6.

Air dissolved in the electrolyte solution and the air space in the cell body was displaced by bubbling the solution for 30 min with 99.99995% Nitrogen gas at a flow rate of $200 \text{ cm}^3/\text{min}$. The Nitrogen gas was continuously introduced into the cell during the XAFS experiment through a PTFE tube from the top of the cell body and was released through gaps between the body and the carbon plates. Accordingly, the inner pressure of the cell was always slightly higher than the atmosphere, which prevents the invasion of outside air. A small PCTFE sub cell block was prepared on one side of the main cell body, as shown in Fig. 2.3(a), where a reversible hydrogen electrode (RHE) was placed. A commercially available glass RHE was used, as shown in the picture of Fig. 2.1(a) and in the drawing of Fig. 2.3(a). A Pt mesh counter electrode (CE) was located in the sub cell block at the opposite side of the main body. The sub cell was fixed to the wall of the cell body through the PCTFE flange and the PTFE connector, as shown in the picture of Fig. 2.1 and in the drawing of Fig. 2.3(a). The electrochemically measured surface area of Pt mesh was $61 \text{ cm}^2\text{-Pt}$ which was 1/25th of that of Pt/Au electrocatalyst at the XAFS measurement.

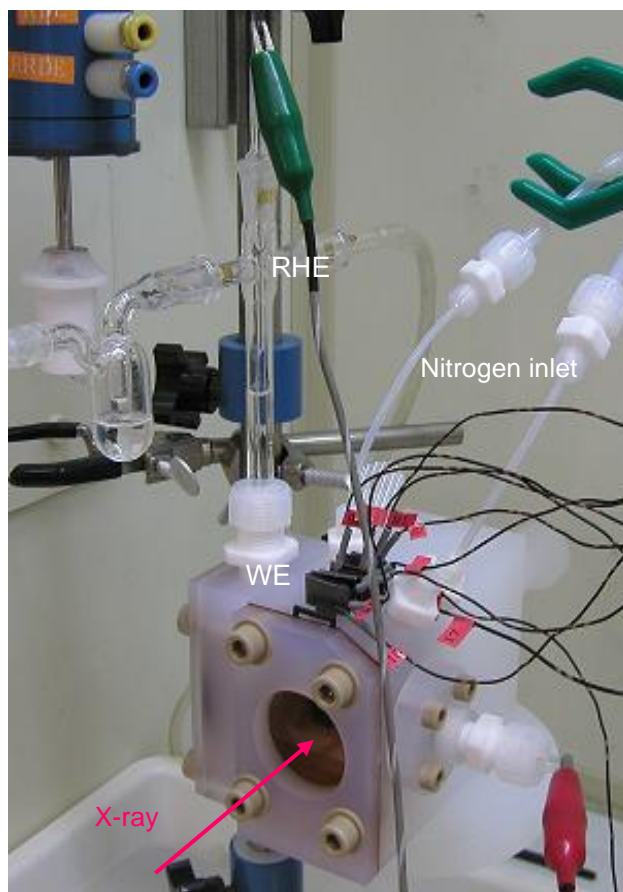
The RHE and CE were located at the opposite side of the main cell and the WE was placed between them as shown in Fig. 2.3(a). The reason of this configuration is as follows. There was a large potential gradient between CE and WE during potential sweep because of large current induced by the large amount of electrocatalyst. However in this configuration there was only definite potential gradient between the WE and RHE because most of the current flows to the other direction. Consequently, the potential of WE was able to be controlled accurately to RHE.

Fig. 2.3(b) is the drawing of the carbon plate for the formation of electrocatalyst layers at the both side specially designed for K-edge experiment. The total thickness

of the carbon plates was 1.5 mm and the depth of the recess was 0.5 mm. The thinnest part of the carbon plate was 0.5 mm to reduce the X-ray absorption by the carbon plates. The shape of the recess was rectangular and the dimension was 6.0 mm width and 2.5 mm height. The longer width was appropriate to the X-ray beam size of beam line BL16B2 of SPring-8.

A mobile PCTFE piston with Kapton window was set at the end of the cell along the optical axis, as shown in Fig. 2.2(a) and Fig. 2.3(a), to adjust the X-ray absorption of the electrolyte solution depending on the number of carbon plates coated with electrocatalyst layer and to reduce the solution thickness. In addition it is possible to reduce the thickness down to *ca.* 0.5 mm to conduct Pt L_{III}-edge XAFS experiment with the same cell. Because there is the large X-ray absorption of electrolyte solution at the Pt L_{III}-edge, it has to be reduced to less than approximately 0.5 mm to obtain analyzable XAFS spectra. The piston was doubly sealed with a corrosion-resistant and low friction Zalac O-ring (Dupont) allowing smooth motion in the direction of the X-rays. At the measurement of Pt L_{III}-edge, only one end slit shown in the Fig. 2.3(a) was used. Fig. 2.3(c) is the drawing of the carbon plate specially designed for Pt L_{III}-edge XAFS experiment. Only one side of the carbon plate had the recess. Comparing the carbon plate designed for Pt L_{III}-edge with that for K-edge, the distinguished difference was the 0.5 mm height protuberance formed on the recess side of the carbon plate. At the XAFS experiment the other flat surface of carbon plate was contacted to the Kapton film of the cell body and the recess side of carbon plate faced to the Kapton film of the mobile piston. Accordingly the piston was slowly moved to the carbon plate and the Kapton film on the piston was contacted with the protuberance. Hence the thickness of electrolyte solution was automatically and easily controlled to the 0.5 mm.

(a)



(b)

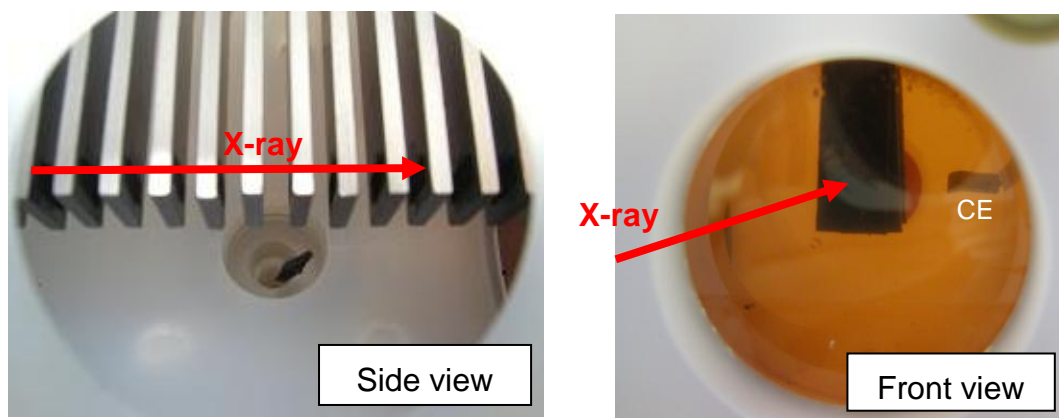
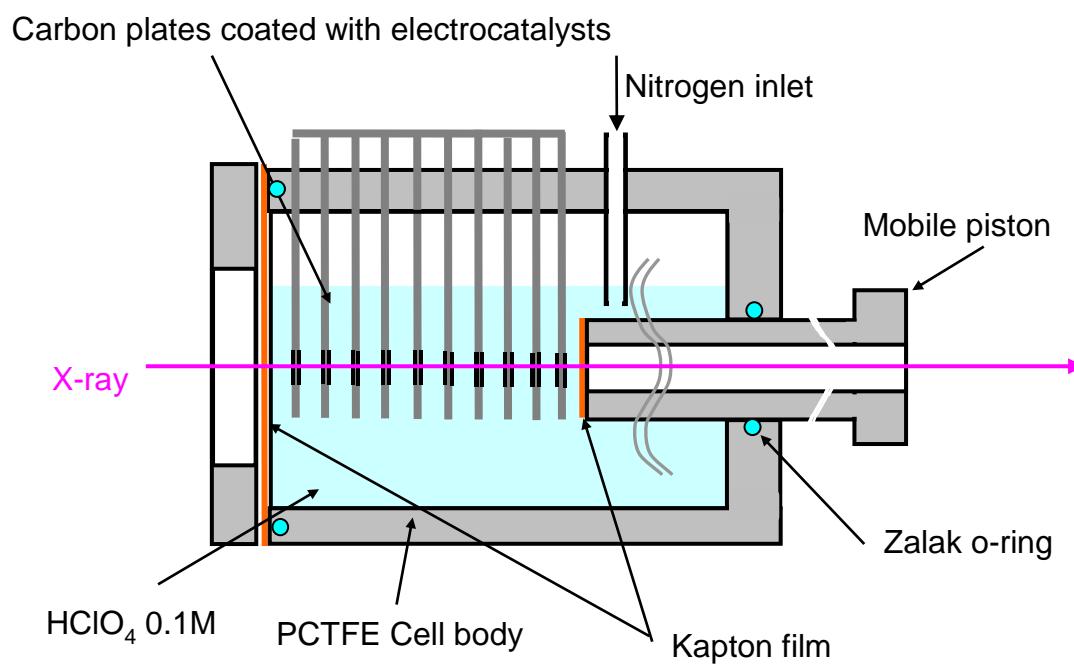


Figure 2.1 Pictures of the spectroelectrochemical cell; (a) Overall view: The cell in the experimental hutch. Red and green clips were connected to the CE and RHE, respectively. Other wires were connected to the WE. X-rays entered from the left side, as indicated by the arrow and (b) Inside view of the cell, left: side view, right: front view.

(a)



(b)

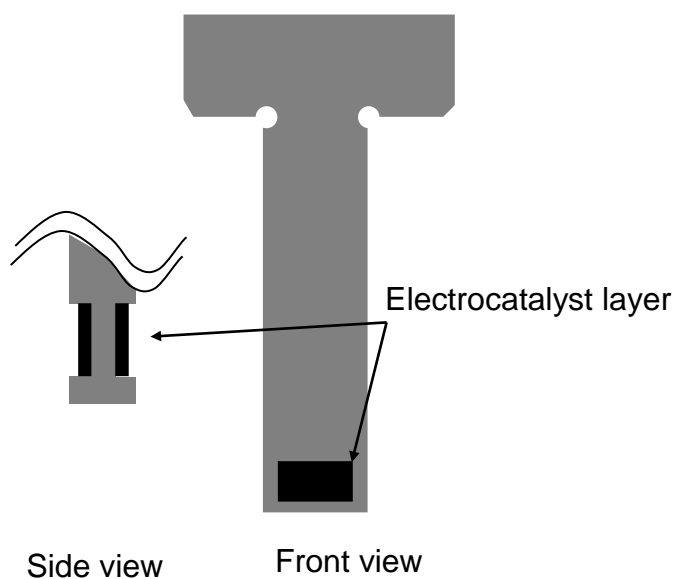


Figure 2.2 Schematic drawing of the spectroelectrochemical cell; (a) Sectional drawing of the cell and (b) Magnified drawing of the carbon plate coated with electrocatalyst (black areas) on both sides of the recesses in the carbon plate.

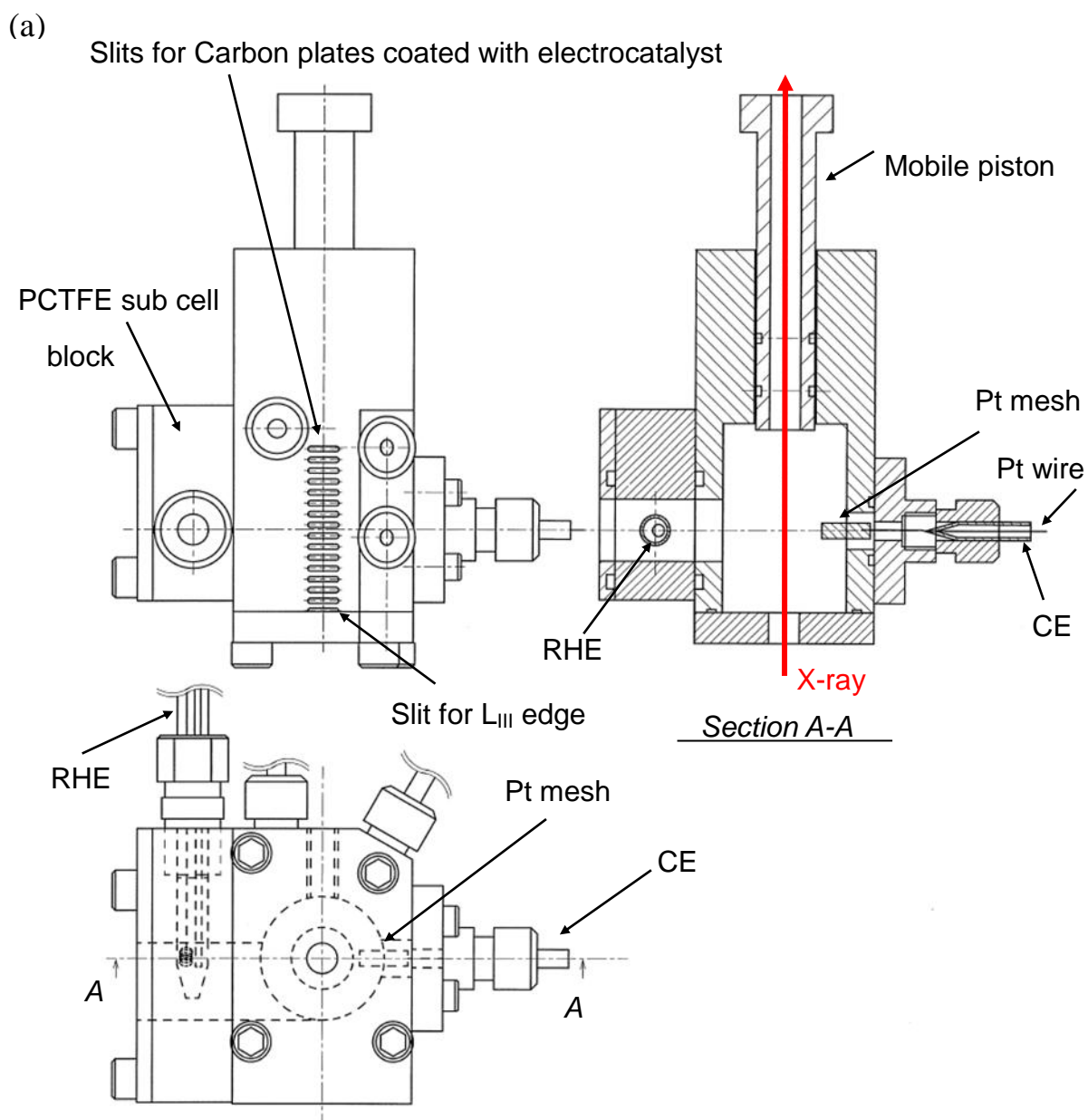


Figure 2.3 (a) Drawing of spectroelectrochemical cell.

(b)

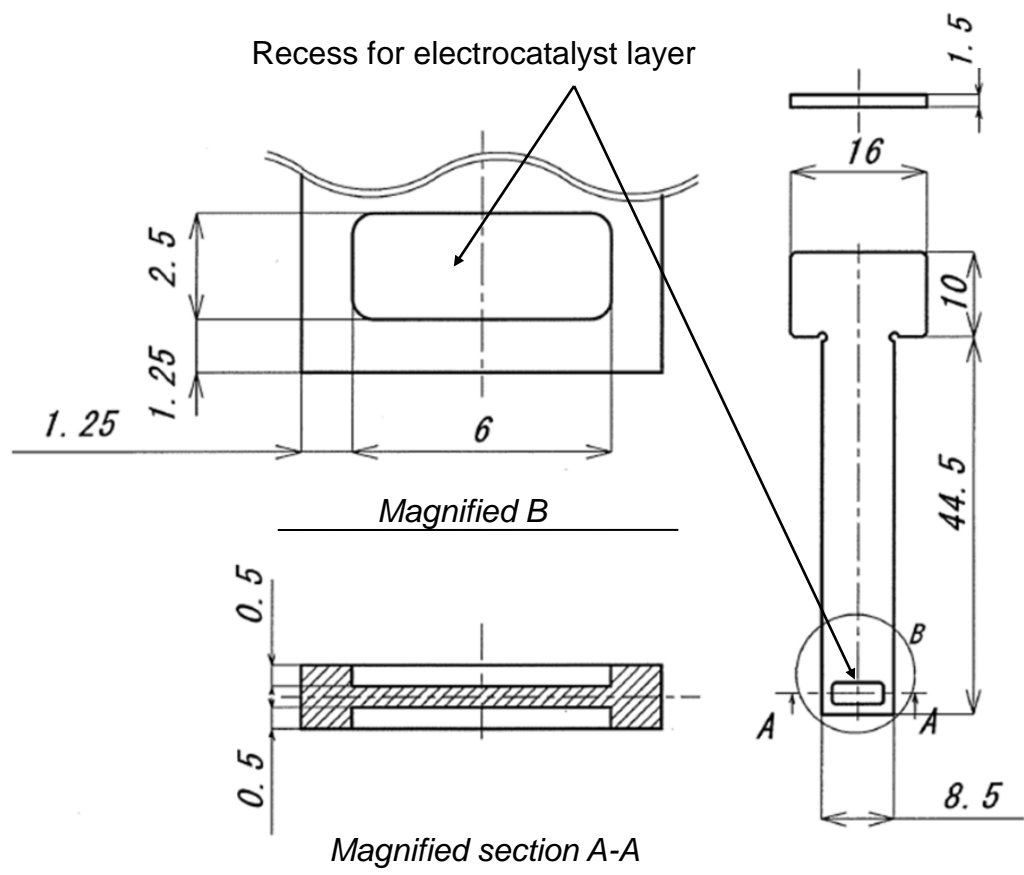


Figure 2.3 (b) Drawing of the carbon plate for K-edge experiment, electrocatalyst layer is formed on both side of the plate.

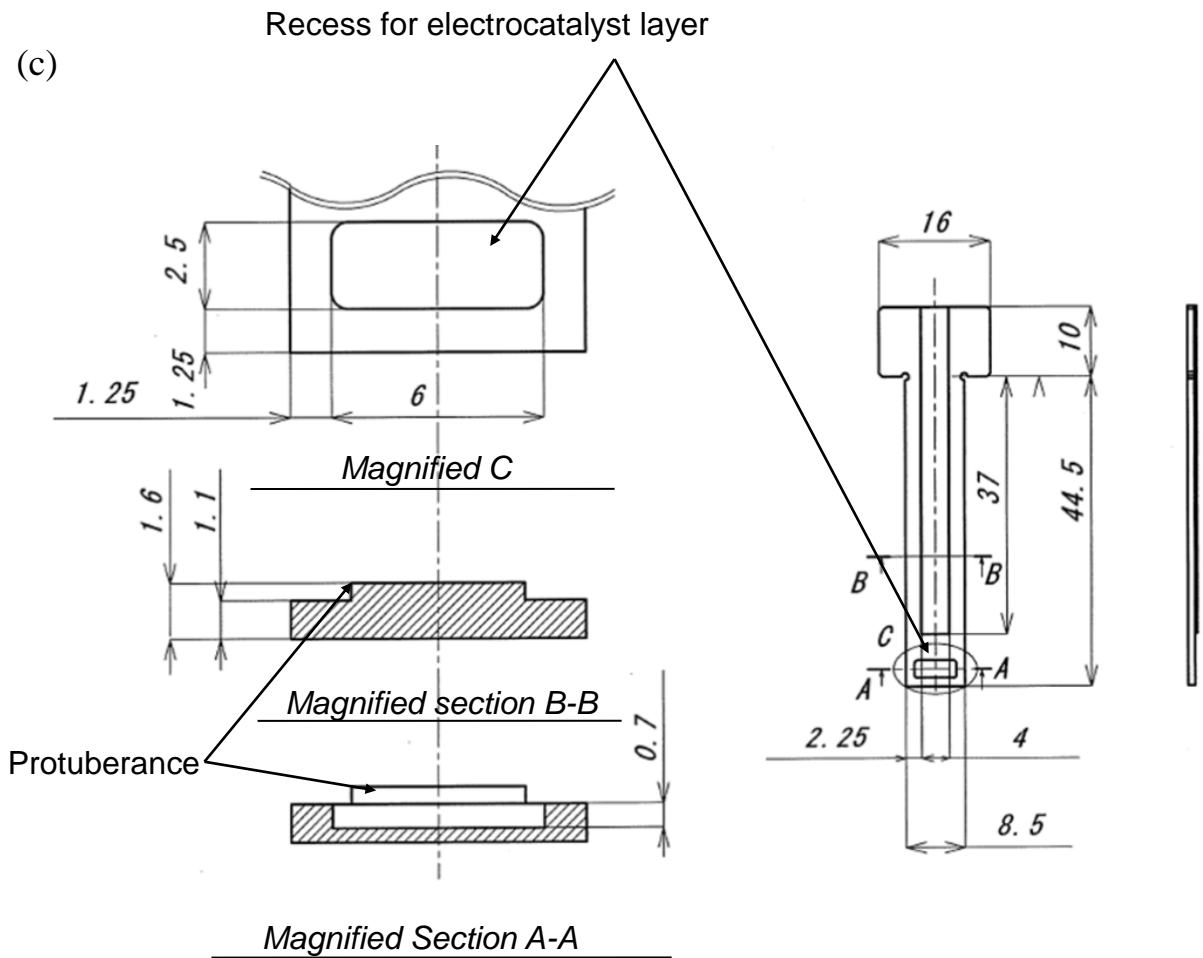


Figure 2.3 (c) Drawing of the carbon plate for L-edge experiment, electrocatalyst layer is formed on one side of the plate.

2.3.2 XAFS measurement

XAFS experiments were conducted at the X-ray bending magnet beamline BL16B2 of SPring-8 in Japan. The ring was operated at 8 GeV with a ring current of 100 mA in a top-up mode. The X-ray beam was monochromatized using a Si (511) double crystal monochromator. The incident and transmitted X-ray intensities were monitored using two ionization chambers filled with Kr before and after the sample, respectively. The spline smoothing method was applied to remove the smooth background followed by normalization according to the edge height.¹⁸ The k^3 -weighted XAFS oscillations were Fourier transformed to the r-space.

2.4 Results and discussion

2.4.1 Electrode performance in the spectroelectrochemical cell

The total masses of the electrocatalyst used in the newly developed *in situ* spectroelectrochemical cell were significantly larger than those typically used in the evaluation of electrocatalysts on a rotating disk electrode (RDE). Therefore, in order to control and reduce the observed current, the potential scan rate was significantly reduced to 0.5 mVs^{-1} , to obtain cyclic voltammogram (CV) which was approximately 1/100th that of a typical scan rate.

Figure 2.4(a) and 2.4(b) are CV obtained in N_2 -saturated $0.1 \text{ molL}^{-1} \text{ HClO}_4$ aqueous solution by RDE and spectroelectrochemical cell respectively. In addition total Pt weight of Fig. 2.4 (a) and (b) is $3.44 \text{ }\mu\text{g}$ and 10.5 mg respectively. Hence in spite of slow sweep rate, the CV of spectroelectrochemical cell shows the larger current than that of RDE. The current was measured during anodic (positive direction) and cathodic (negative direction) potential sweeps from 0.0 to 1.2 V and from 1.2 to 0.0 V , respectively. During the anodic potential sweep, adsorbed hydrogen was desorbed from *ca.* 0.0 V to 0.3 V vs. RHE and oxides were formed on the Pt surface from *ca.* 0.7 V to 1.2 V vs. RHE. During the cathodic potential sweep, the Pt oxides were reduced from *ca.* 1.2 V to 0.4 V vs. RHE and hydrogen was adsorbed on the Pt surface from *ca.* 0.3 V to 0.0 V vs. RHE.

The CV obtained with the new spectroelectrochemical cell was not completely the same as that obtained with a RDE. Comparing the Fig. 2.4(a) with Fig. 2.4(b), around 0.4 V , the difference between the cathodic and anodic currents in the spectroelectrochemical was larger than that of RDE, indicating the larger amount of double layer owing to increasing surface area of the carbon plates contacting electrolyte solution. Another difference of RDE and the spectroelectrochemical cell is the minimum-current potential of cathodic sweep and anodic sweep. In the case of RDE, they are almost the same potential, 0.4 V . However in the case of spectroelectrochemical cell, minimum current potential of anodic sweep was slightly

shifted to higher potential compared with that of RDE. In addition minimum-current potential of cathodic sweep was slightly lower compared with that of RDE. They were induced by larger current and the potential gradient in the electrolyte solution and catalyst layer in spite of aforementioned WE, CE, RHE configuration and slow potential sweep speed. However the characteristic hydrogen adsorption, desorption and oxide formation, reduction responses of Pt were perfectly observed. Moreover the effective electrochemical surface area (ECSA) calculated from the hydrogen adsorption wave of the obtained CV for the spectroelectrochemical cell was 90 % or more of that previously obtained using a RDE, which indicates that most of the large amount of Pt in the catalyst layers was effectively used. Thus in the electrochemical cell, the potential in the electrocatalyst was well controlled.

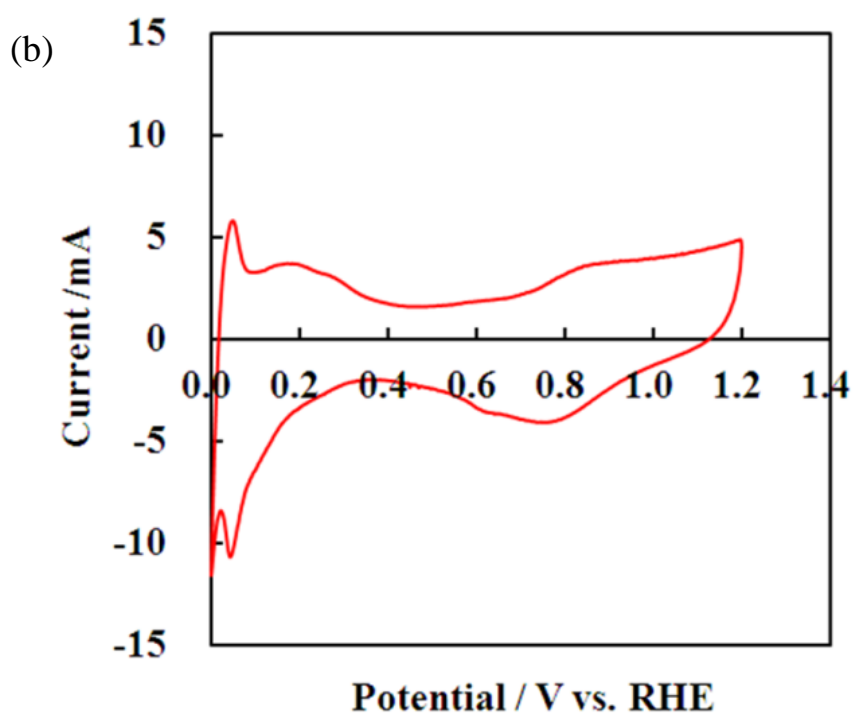
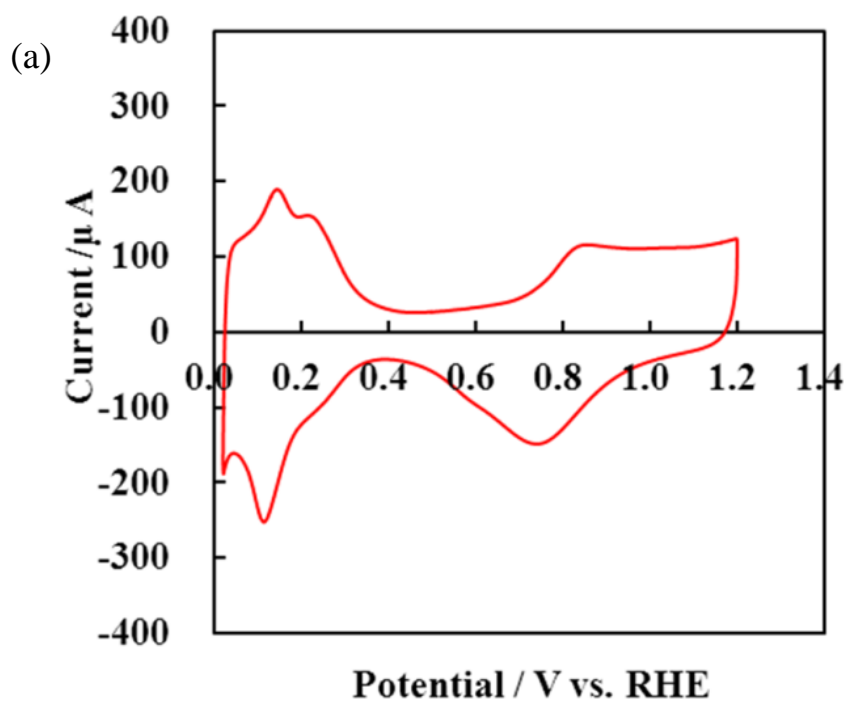


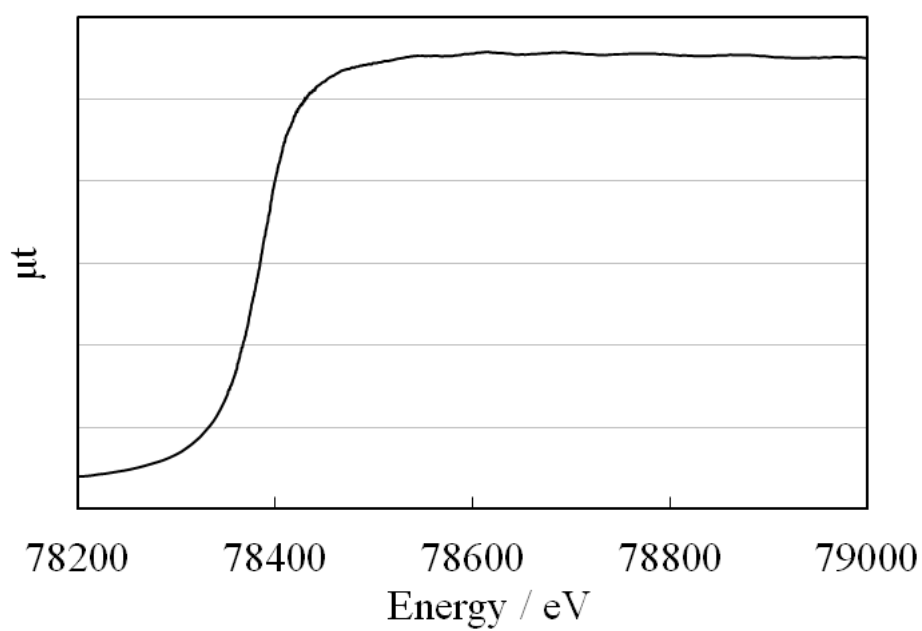
Figure 2.4 Cyclic voltammogram of the Pt/C electrocatalyst; (a) RDE and (b) Spectroelectrochemical cell.

2.4.2 Pt K-edge EXAFS measurement of Pt foil

Figure 2.5 shows the Pt K-edge and L_{III}-edge XAFS spectra of Pt foil. Figure 2.6 shows the Pt K-edge and L_{III}-edge EXAFS oscillations of Pt foil. The Pt K-edge XAFS spectra have a smooth and dull edge jump due to life-time broadening.¹⁴ The K-edge EXAFS oscillations more than 50 nm⁻¹ could be extracted after appropriate background removal, as shown in Fig. 2.6(a). In contrast, the L_{III}-edge spectrum showed clear XAFS oscillations with a sharp white line at the absorption edge.

In the L_{III}-edge, the X-ray transition occurs from $l = 1$ to $l = 2$ (main) and $l = 0$ (minor), while the $l = 0$ to $l = 1$ transition was observed in the K-edge. Hence the EXAFS oscillations of the K and L_{III}-edge oscillations have a π -difference in the phase according to the EXAFS principle.^{19,20} For example, at 100 nm⁻¹, the K-edge has a positive peak, while the L_{III}-edge has a negative peak. The K- and L_{III}-edge data were analyzed based on the FEFF-derived phase shift and amplitude functions.^{19,20} The Pt-Pt bond distance were determined as 0.278 ± 0.001 nm and the errors of which were with a 90 % confidence level by the Hamilton ratio method.²¹ Pt-Pt bond distance of Pt-K was 0.003 nm longer than that of Pt-L_{III} as we mentioned in section 3.3.3 of chapter 3.

(a)



(b)

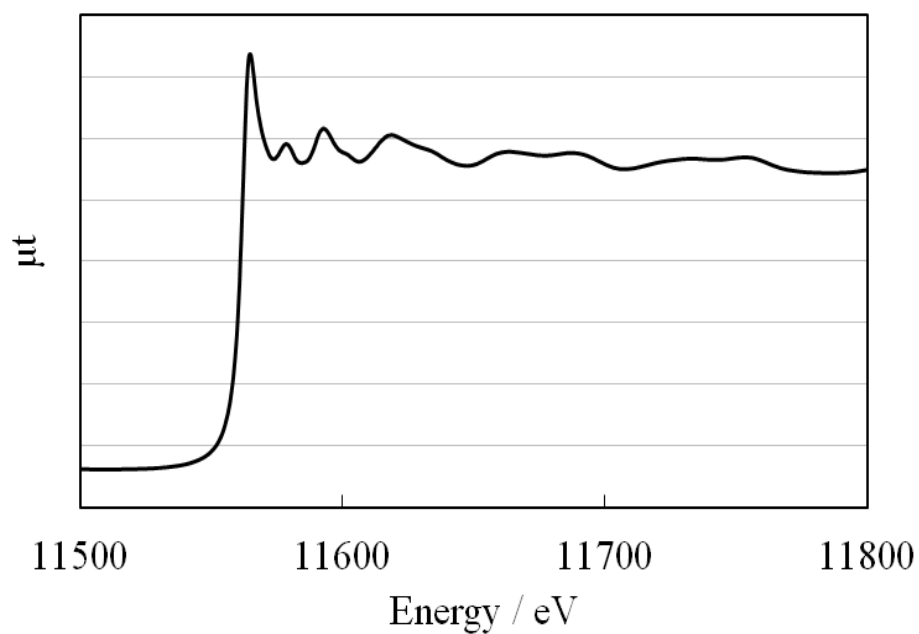
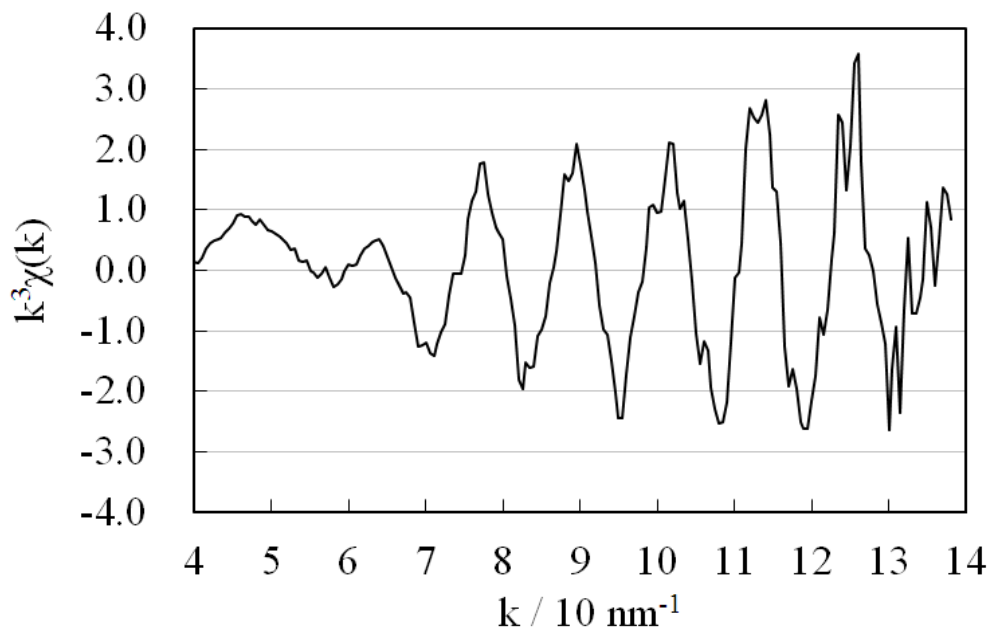


Figure 2.5 X-ray absorption spectra of Pt foil; (a) Pt K-edge and (b) Pt L_{III}-edge.

(a)



(b)

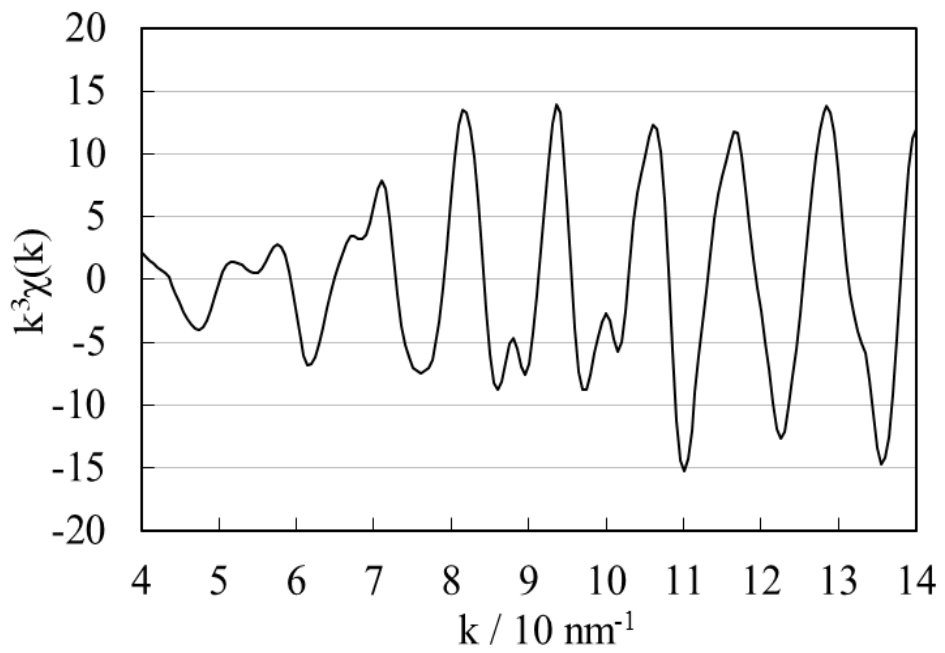


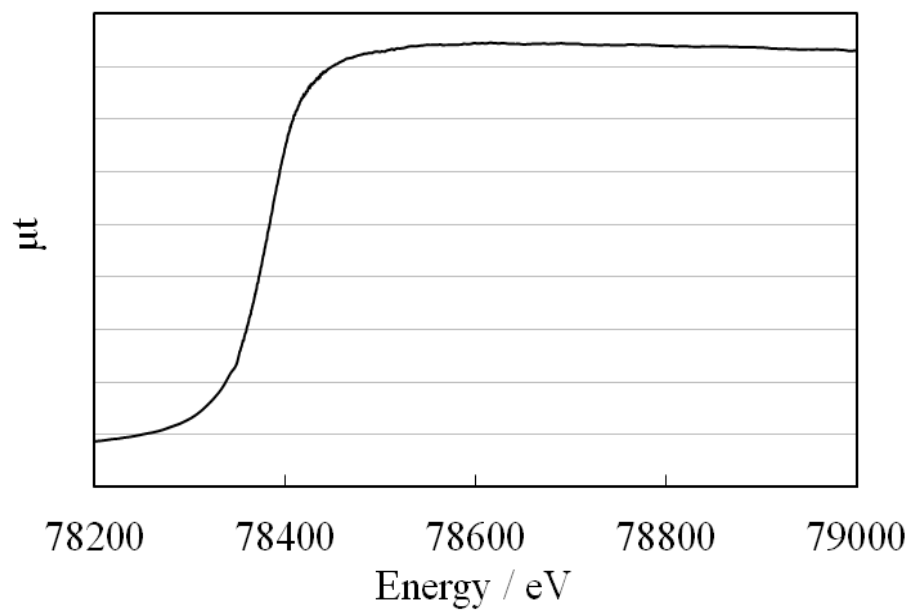
Figure 2.6 EXAFS oscillations of Pt foil; (a) Pt K-edge and (b) Pt L_{III}-edge.

2.4.3 XAFS measurement with the electrochemical cell

The performance of the *in situ* EXAFS measurement cell was evaluated with Pt/C. One advantage of the *in situ* cell is the availability of surface cleaning of the electrocatalyst by oxidation and reduction cycles. Another advantage is the precise control of the potential under fixed electrochemical equilibrium such as the adsorption structure and the oxidation state. Before the XAFS experiment the oxidation and reduction cycles were performed three times between 0.05 and 1.1 V vs. RHE at a sweep rate of 1 mVs⁻¹. After the cleaning process, an anodic sweep was conducted from 0.05 to 0.4 V vs. RHE at a sweep rate of 1 mVs⁻¹, where the sample was free of hydrogen and any oxides. The potential was held for 20 min prior to XAFS measurement so that equilibrium could be obtained completely. In comparison of Pt-L_{III} edge XANES spectra of Pt foil shown in Fig. 2.5(b) and Pt nanoparticle shown in Figure 2.7(b) the difference in the white line was small. This is the indication that the potential of Pt nanoparticles were well controlled at 0.4 V and the Pt particles were well reduced and no oxides were formed.

Fig. 2.7 and Figure 2.8 show the Pt K-edge and L_{III}-edge absorption spectra, and the EXAFS oscillations of Pt/C at 0.4 V vs. RHE, respectively. Compared to the Pt foil EXAFS the oscillations were quite small, which indicates the smaller coordination number and the presence of nanoclusters.

(a)



(b)

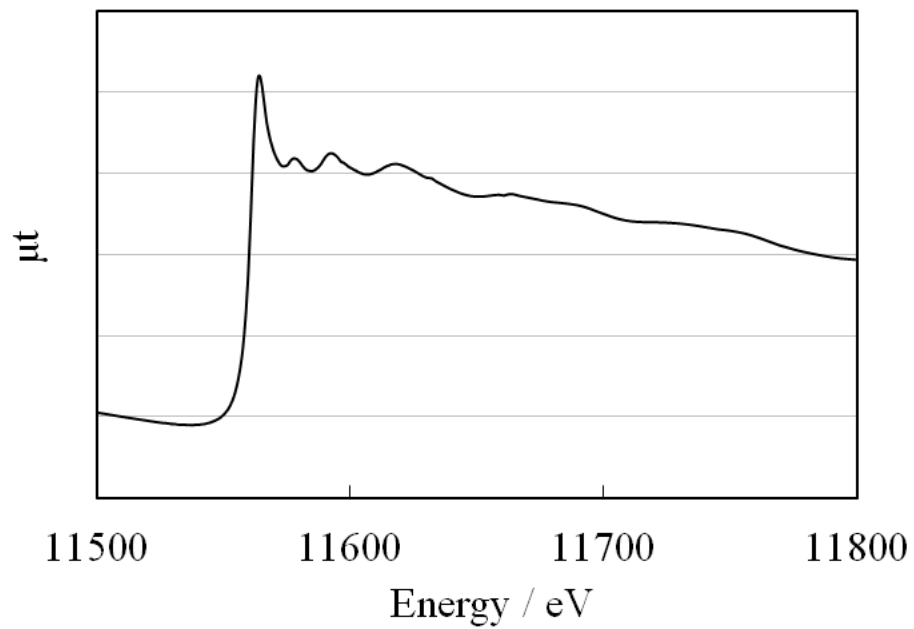


Figure 2.7 *In situ* X-ray absorption spectra of Pt/C at 0.4 V vs. RHE; (a) Pt K-edge and (b) Pt L_{III}-edge.

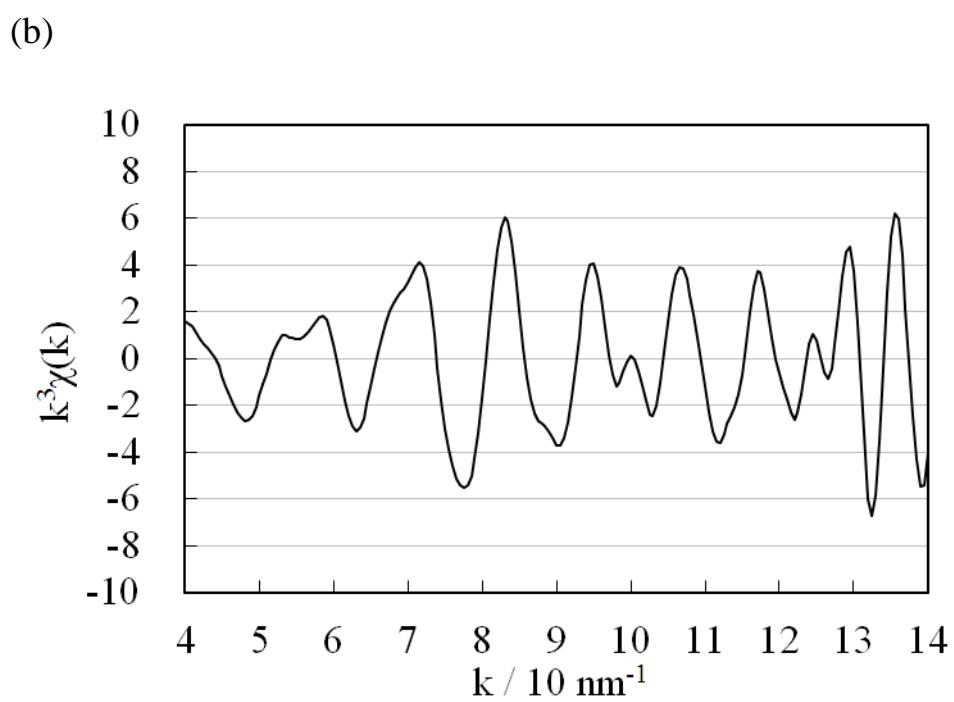
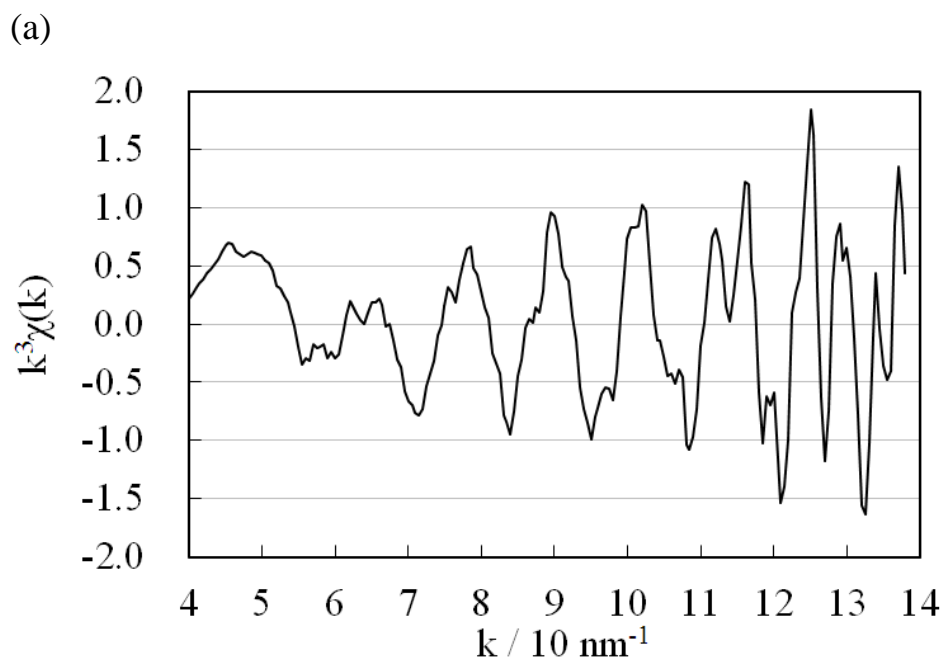


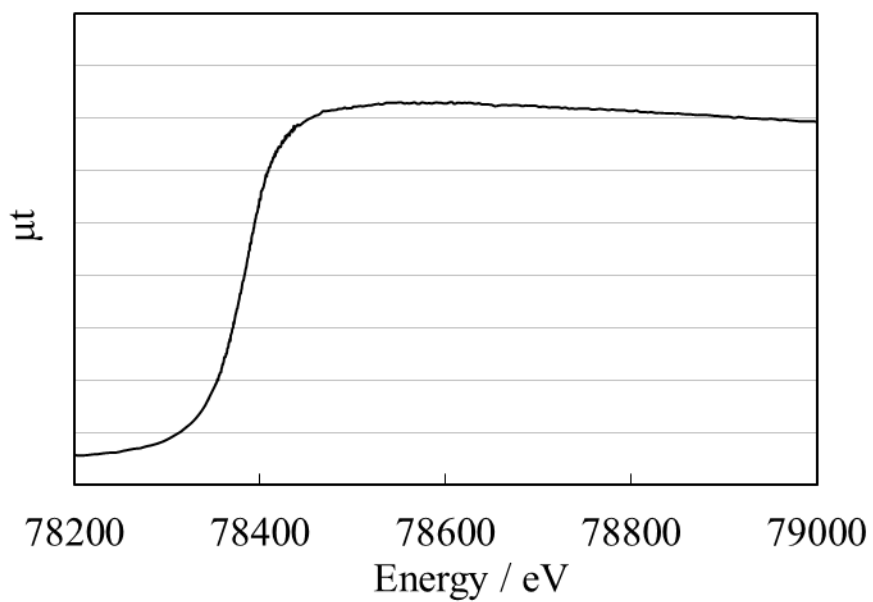
Figure 2.8 EXAFS oscillations of Pt /C at 0.4 V vs. RHE; (a) Pt K-edge and (b) Pt L_{III}-edge

2.4.4 EXAFS measurement of the Pt/Au/C electrocatalyst in the electrochemical cell

Figure 2.9 and 2.10 show the Pt and Au K-edge and L_{III}-edge spectra for the Pt/Au/C electrocatalyst respectively. The Au L_{III}-edge appeared just after the Pt L_{III}-edge as shown in Fig. 2.10. The energy separation of Pt and Au was approximately 400 eV. On the other hand, the energy separation between the Pt and Au for the K-edge was as large as 2300 eV as shown in Fig. 2.9. Figure 2.11 shows the k^3 -weighted EXAFS oscillation of the Pt/Au/C electrocatalyst at 0.4 V vs. RHE. As shown in Fig. 2.10 and Fig. 2.11(a) the Pt L_{III}-edge EXAFS oscillation was interrupted by the Au L_{III}-edge and the EXAFS oscillation was obtained up to only 95 nm⁻¹. On the other hand, in the Pt K-edge EXAFS oscillation, the oscillation reached the k-value more than 120 nm⁻¹ as shown in Fig. 2.11(b).

A detailed analysis of the EXAFS is described in chapter 3. The Pt-Pt, Pt-Au and Au-Au distances were determined to be 0.275 ± 0.003 , 0.279 ± 0.004 and 0.282 ± 0.003 nm with coordination numbers of 7.2 ± 2.9 , 2.0 ± 0.8 , and 9.7 ± 2.9 , respectively, which corresponded well to those of the Au core and Pt shell structure with contracted Pt-Pt bond lengths.

(a)



(b)

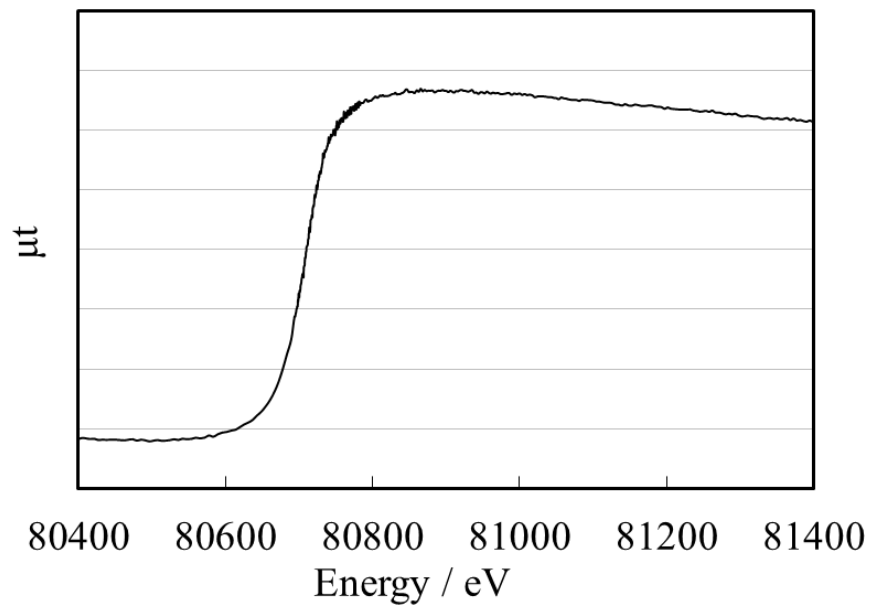


Figure 2.9 *In situ* X-ray absorption spectra of Pt/Au/C at 0.4 V vs. RHE; (a) Pt K-edge, (b) Au K-edge and

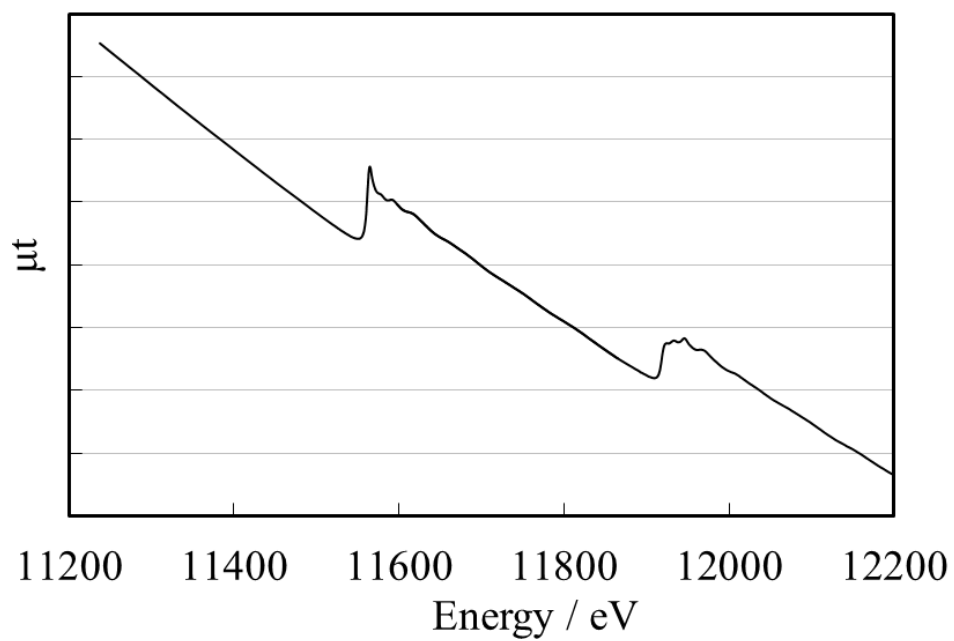


Figure 2.10 *In situ* Pt and Au L_{III}-edges X-ray absorption spectra of Pt/Au/C at 0.4 V vs. RHE.

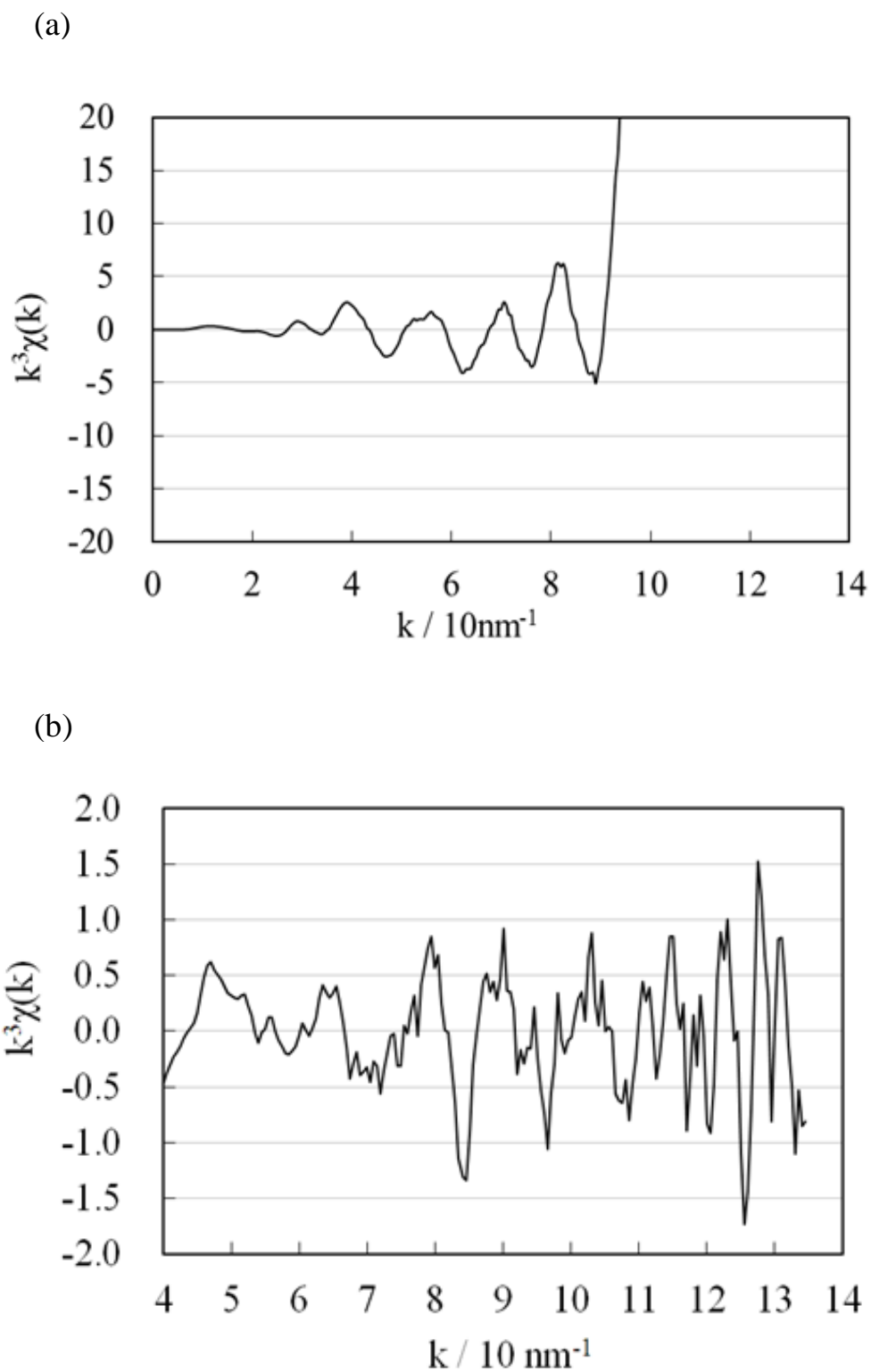


Figure 2.11 EXAFS oscillations of Pt/Au/C at 0.4 V vs. RHE; (a) Pt L_{III}-edge and (b) Pt K-edge.

2.5 Conclusions

I presented an *in situ* spectroelectrochemical cell that facilitates EXAFS measurements of both the K edge of Pt and Pt/Au electrocatalysts under electrochemical equilibrium conditions with a precisely controlled potential. The cell also can be applied to L_{III} edge XAFS. The CV obtained with this cell and ECA calculated from the CV showed that almost all of the electrocatalyst in the spectroelectrochemical cell was effectively used.

Experimental XAFS results for Pt/C and Pt/Au/C core-shell electrocatalysts at 0.4 V vs. RHE showed that the spectroelectrochemical cell allowed us the K-edge EXAFS analyses of Pt and Pt/Au bimetallic clusters under electrochemically well controlled conditions. Such well controlled potential insured the Pt and Au state. Detailed EXAFS analysis of obtained spectra is described in following chapter 3.

2.6 References

- ¹ Adzic, R. R.; Zhang, J.; Sasaki, K.; Vukmirovic, M. B.; Shao, M.; Wang, J. X.; Nilekar, A. U.; Mavrikakis, M.; Valerio, J. A.; Uribe, F., Platinum Monolayer Fuel Cell Electrocatalysts. *Topics in Catalysis* **2007**, *46*(3-4), 249-262.
- ² Brankovic, S. R.; Wang, J. X.; Adzic, R. R., New methods of controlled monolayer-to-multilayer deposition of Pt for designing electrocatalysts at an atomic level. *Journal of the Serbian Chemical Society* **2001**, *66*(11-12), 887-898.
- ³ Kristian, N.; Wang, X., Ptshell–Au core/C electrocatalyst with a controlled shell thickness and improved Pt utilization for fuel cell reactions. *Electrochemistry Communications* **2008**, *10*(1), 12-15.
- ⁴ Wang, S.; Kristian, N.; Jiang, S.; Wang, X., Controlled synthesis of dendritic Au@Pt core–shell nanomaterials for use as an effective fuel cell electrocatalyst. *Nanotechnology* **2009**, *20*(2), 025605.
- ⁵ Luo, J.; Wang, L.; Mott, D.; Njoki, P. N.; Lin, Y.; He, T.; Xu, Z.; Wanjana, B. N.; Lim, I. I. S.; Zhong, C.-J., Core/Shell Nanoparticles as Electrocatalysts for Fuel Cell Reactions. *Advanced Materials* **2008**, *20*(22), 4342-4347.
- ⁶ Zhang, J.; Lima, F. H. B.; Shao, M. H.; Sasaki, K.; Wang, J. X.; Hanson, J.; Adzic, R. R., Platinum Monolayer on Nonnoble Metal–Noble Metal Core–Shell Nanoparticle Electrocatalysts for O₂ Reduction. *The Journal of Physical Chemistry B* **2005**, *109*(48), 22701-22704.
- ⁷ Nagamatsu, S.-i.; Arai, T.; Yamamoto, M.; Ohkura, T.; Oyanagi, H.; Ishizaka, T.; Kawanami, H.; Uruga, T.; Tada, M.; Iwasawa, Y., Potential-Dependent Restructuring and Hysteresis in the Structural and Electronic Transformations of Pt/C, Au(Core)-Pt(Shell)/C, and Pd(Core)-Pt(Shell)/C Cathode Catalysts in Polymer Electrolyte Fuel Cells Characterized by in Situ X-ray Absorption Fine Structure. *The Journal of Physical Chemistry C* **2013**, *117*(25), 13094-13107.
- ⁸ Xiu, C.; Shengnan, W.; Scott, J.; Zhibing, C.; Zhenghua, W.; Lun, W.; Yongxin, L., The Deposition of Au–Pt Core–Shell Nanoparticles on Reduced Graphene Oxide and their Catalytic Activity. *Nanotechnology* **2013**, *24*, 295402.
- ⁹ Inaba, M.; Tsuji, H., Platinum Core-Shell Catalyst Manufacturing Method, and Fuel Cell using Catalyst, Japan Patent, WO2011115012 A1, March 19 2010.
- ¹⁰ Tsuji, H.; Kaneko, A.; Banno, M.; Yamada, H.; Saito, M.; Tasaka, A.; Inaba, M., A Novel Technique for Preparation of Pt shell/Au core/C Core-Shell Catalysts and Their Activity for Oxygen Reduction Reaction. In 218th ECS Meeting Abstracts Las Vegas, 2010,; Vol. MA2010-02, p. 858.
- ¹¹ Shibata, M.; Hayashi, N.; Sakurai, T.; Kurokawa, A.; Fukumitsu, H.; Masuda, T.; Uosaki, K.; Kondo, T., Electrochemical Layer-by-Layer Deposition of Pseudomorphic Pt Layers on Au(111) Electrode Surface Confirmed by Electrochemical and In Situ Resonance Surface X-ray Scattering Measurements. *The Journal of Physical Chemistry C* **2012**, *116*(50), 26464-26474.
- ¹² Zhang, J.; Sasaki, K.; Sutter, E.; Adzic, R. R., Stabilization of Platinum Oxygen-Reduction Electrocatalysts Using Gold Clusters. *Science* **2007**, *315*(5809), 220-222.
- ¹³ Asakura, K.; Satow, Y.; Kuroda, H., CE K-EDGE EXAFS SPECTRUM OF CEO₂. *Journal De Physique* **1986**, *47*(C-8), 185-188.
- ¹⁴ Nishihata, Y.; Emura, S.; Maeda, H.; Kubozono, Y.; Harada, M.; Uruga, T.; Tanida, H.; Yoneda, Y.; Mizuki, J.; Emoto, T., XAFS spectra in the high-energy region measured at SPring-8. *Journal of Synchrotron Radiation* **1999**, *6*(3), 149-151.
- ¹⁵ Nagamatsu, S.-I.; Arai, T.; Yamamoto, M.; Oyanagi, H.; Daimaru, A.; Ishizaka, T.; Kawanami, H.; Uruga, T.; Tada, M.; Iwasawa, Y., In Situ XAFS Study on PEFC Catalysts: Structure and Behavior of Pt-M/C (M=Au, Pd) in the Stepwise Voltage

-
- Operation. In *220th ECS Meeting Abstracts*, Boston, 2011, MA2011-02, 1055.
- ¹⁶ McBreen, J.; O'Grady, W. E.; Pandya, K. I., EXAFS: A new tool for the study of battery and fuel cell materials. *Journal of Power Sources* **22** (3-4), 323-340.
- ¹⁷ Satow, Y.; Asakura, K.; Kuroda, H., MEASUREMENTS OF THE EXTENDED X-RAY ABSORPTION FINE-STRUCTURE (EXAFS) SPECTRA AT THE K EDGES OF CERIUM, PRASEODYMIUM AND SAMARIUM COMPOUNDS WITH SYNCHROTRON RADIATION. *Journal of Physics C-Solid State Physics* **1987**, *20* (31), 5027-5035.
- ¹⁸ K. Asakura, In *X-ray Absorption Fine Structure for Catalysts and Surfaces*; 1 ed.; Iwasawa, Y., Ed.; World Scientific: Singapore, 1996; Vol. 2, p. 33.
- ¹⁹ J. J. Rehr, J. J. Kas, M. P. Prange, A. P. Sorini, Y. Takimoto, and F. Vila, *Comptes Rendus Physique*, *10*(6), 548 (2009).
- ²⁰ Rehr, J. J.; Albers, R. C., Theoretical approaches to x-ray absorption fine structure. *Reviews of Modern Physics* **2000**, *72* (3), 621-654.
- ²¹ Hamilton, W., Significance tests on the crystallographic R factor. *Acta Crystallographica* **1965**, *18* (3), 502-510.



Chapter 3

**K-edge X-ray Absorption Fine Structure Analysis of
Pt/Au Core-Shell Electrocatalyst**

- Evidence for Short Pt-Pt Distance -

3.1 Introduction

In this chapter, detailed preparation process of Pt/Au core-shell on carbon support which is similar to that reported by Inaba and coworkers^{1,2}, and the characterization of resultant carbon-supported Pt-Au electrocatalyst using *in situ* Pt and Au K-edge XAFS spectroscopic measurements together with physical and electrochemical analyses are described. The analysis of EXAFS spectra shown in chapter 2 is described in this chapter. I discussed the structural parameters obtained by curve fitting and the origin of the enhanced area-specific activity of Pt/Au/C.

3.2 Materials and methods

3.2.1 Preparation of Pt/Au/C core-shell electrocatalyst

The following procedure was used to prepare the Pt/Au/C electrocatalyst samples. Au nanoclusters were first prepared using the sputter-deposition-onto-ionic-liquid method^{3,4,5} which produces small homogeneous Au nanoclusters. A sputter coater (SC-704, Sanyu Electron; acceleration voltage =1 kV, ion current = 20 mA) was used to sputter Au into 3 mL of ionic liquid (1-butyl-3-methylimidazolium tetrafluoroborate; C₄mimBF₄) at 328 K for 180 minutes. Then 0.78 g of carbon black (XC-72R, Vulcan) was impregnated with the Au nanoparticles in C₄mimBF₄ solution for 24 hours, followed by stirring in 200 mL acetone (Wako, reagent grade) for 10 min to remove C₄mimBF₄, and the suspension was then filtered. This washing process was conducted three times to completely remove the ionic liquid. The resultant Au/C was dried in an oven at 333 K for 24 hours. 0.1 g of Au/C was suspended in 200 mL of ultrapure water and the solution was stirred with a magnetic stirrer for 15 minutes. The Au/C-suspended solution was then slowly added to 2 L of ultrapure water, which was deaerated by bubbling with Nitrogen for 30 minutes. 1.0 g of 7.2 wt% H₂PtCl₆ aqueous solution was added dropwise to the solution; the resulting solution was stirred under a Nitrogen atmosphere for 24 hours at room temperature. The resulting Pt/Au/C was filtered and dried for more than 4 hours at 333 K. Finally, the Pt/Au/C product was scraped from the filter paper, yielding carbon-supported electrocatalyst powder. Commercially available Pt/C was used as a reference (nominal Pt loading 50 wt%, Ketjen black carbon support; TEC10E50E, Tanaka Kikinzoku Kogyo K.K.).

3.2.2 Characterization of Pt/C and Pt/Au/C core-shell electrocatalysts

The resulting catalysts were characterized using transmission electron microscopy (TEM; HF-2000 field emission TEM Hitachi High-Technologies) with energy dispersive X-ray spectroscopy (EDS; KeveX), inductively coupled plasma-mass spectrometry (ICP-MS; SPS-3520, SII NanoTechnology), and electrochemical methods.

TEM was used to determine the particle diameter distribution and average diameter of the electrocatalyst particles. Microscopic elemental analysis of the Pt/Au core-shell nanoclusters was conducted using EDS. The amounts of Pt and Au electrocatalysts were measured using ICP-MS. The surface composition of Pt and Au was derived by electrochemical methods using a three-electrode glass cell and a rotating disk electrode (RDE) measurement apparatus (HZ-5000, Hokuto Denko). For the electrochemical experiments, a reversible hydrogen electrode (RHE) and Pt mesh were used as the reference and counter electrodes, respectively. Cyclic voltammograms were obtained in deaerated 0.1 M HClO₄ solutions. Polarization curves were recorded in an Oxygen-saturated HClO₄ solution.

3.2.3 XAFS measurements

XAFS experiments were conducted at the X-ray bending magnet beamline BL16B2 of SPring-8. The ring was operated in a top-up mode at 8 GeV with the ring current at 100 mA. The X-ray beam was monochromated using a Si (511) double crystal monochromator. The incident and transmitted X-ray intensities were monitored using two ionization chambers filled with Kr before and after the sample, respectively. The setting of the samples in the *in situ* measurement cells has been described elsewhere. Prior to the *in situ* measurements, air was removed by passing pure Nitrogen (99.99995%) through the electrolyte solution and the XAFS cell for 30 minutes. During the measurements, Nitrogen gas was continuously flowed over the electrolyte solution to prevent air contamination. The electrode potential was swept cathodically from the rest potential (ca. 1.0 V) to 0.05 V at a slow scan rate (1 mVs⁻¹) to avoid large current and potential variations in the catalyst layer and between the carbon plates. An oxidation-reduction cycle (ORC) treatment (0.05–1.2 V) was conducted three times to remove contamination from the surface of the electrocatalyst. Following the ORC treatments, XAFS measurements were performed at 0.4 V after holding the electrode potential at 0.4 V for 10 minutes. Pt foil, Au foil, and a Pt/Au random alloy foil

containing 10 at% Pt were also measured as reference samples for curve-fitting analyses.

3.2.4 XAFS analyses

XAFS analyses were conducted using the REX2000 (Rigaku) analysis package. The XAFS oscillation $\chi(k)$ was extracted from the observed data $\mu(E)$ by subtracting the smoothly varying part $\mu_s(E)$, which was estimated from cubic splines.⁶ The difference was then normalized using the edge height $\mu_0(E)$:⁷

$$\chi(k) = \frac{\mu(E) - \mu_s(E)}{\mu_0(E)} \quad (1)$$

where k is the wavenumber of the photoelectron, which is related to the photon energy E , and the threshold energy E_0 , by

$$k = \frac{1}{\hbar} \sqrt{2m(E - E_0)} \quad (2)$$

where m is the mass of the electron. The quantity $k^3\chi(k)$ was Fourier transformed to r space, the peak in the transform was filtered, and then an inverse Fourier transform was applied to convert the filtered peak back to k space. The Fourier-filtered data were then analyzed with a curve-fitting technique using the following theoretical XAFS equations:⁷

$$k^3\chi(k) = \sum_j \frac{k_j^2 S_{0j} N_j F_j(k_j) \exp(-2k_j^2 \sigma_j^2)}{r_j^2} \sin(2k_j r_j + \phi_j(k)) \quad (3)$$

$$k_j = \left(k^2 - \frac{2m\Delta E_{0j}}{\hbar^2} \right)^{\frac{1}{2}} \quad (4)$$

In Eqs.(3) and (4), j denotes each coordination shell, N_j is the coordination number, r_j is the bond length, ΔE_{0j} is the difference between the theoretical and experimental threshold energies, and σ_j is the Debye-Waller factor for the j^{th} coordination shell. The quantities $\phi_j(k)$ and $F_j(k)$ are phase shifts and amplitude functions, respectively, both of which were derived from FEFF8 calculations.⁸ The amplitude reduction factor S_j arises from many-body effects and from inelastic losses during the scattering process. Many-body effects and inelastic losses are dependent on k in opposite ways, so that S_j can be regarded as a constant function of k .

In the curve-fitting analyses, S_j and ΔE_{0j} were fixed at the values obtained for the Pt and Au foils. The quality of the fit was evaluated according to the R -factor:

$$R = \frac{\sum (k^3 \chi_{\text{obs}}(k) - k^3 \chi_{\text{calc}}(k))^2}{\sum (k^3 \chi_{\text{obs}}(k))^2} \quad (5)$$

where $\chi_{\text{obs}}(k)$ and $\chi_{\text{calc}}(k)$ are the observed and curve-fitted $\chi(k)$, respectively.

In the curve-fitting analyses of bimetallic alloys, the following equations must be satisfied within the error:^{9,10,11}

$$N_{\text{XY}} C_{\text{X}} = N_{\text{YX}} C_{\text{Y}} \quad (6)$$

$$R_{\text{XY}} = R_{\text{YX}} \quad (7)$$

where N_{XY} is the coordination number of atom Y around absorber atom X, C_{X} is the mole fraction of atom X, and R_{XY} is the interatomic distance between atoms X and Y on the X absorption edge. Errors in these structural parameters were determined at the 90% confidence level by the Hamilton ratio method.¹²

3.3 Results

3.3.1 Characterization of Pt/C and Pt/Au/C core-shell electrocatalysts

Figures 3.1-3.3 show TEM micrographs of Pt/C, Au/C, and Pt/Au/C, and their particle diameter distributions. The average diameter of Pt nanoclusters was estimated to be 2.2 nm from TEM image analyses of 261 Pt particles. The Au content of Au/C was 8.6 wt% and the average diameter of the Au nanoclusters was determined to be 2.6 nm from image analyses of 339 Au particles. Nanoclusters of Au on carbon had almost the same sizes as that of Au in solution. The Pt and Au contents in the Pt/Au/C catalyst were 4.2 and 3.8 wt%, respectively, as estimated from ICP data. The average diameter of Pt/Au nanoclusters was estimated to be 3.0 nm from TEM image analyses of 195 nanoclusters. Comparison of the average diameter of Au/C with that of Pt/Au/C indicated that the thickness of the Pt shell would be two atomic layers.

The Pt/Au/C was dispersed in a solvent of ultrapure water and Nafion by ultrasonication for 30 minutes. The suspension was deposited on the pre-cleaned glassy carbon substrate of the RDE to satisfy the $5.0 \mu\text{g-Ptcm}^{-2}$ Pt loading and allowed to dry at 60 °C. Figure 3.4 shows cyclic voltammograms for Pt/Au/C recorded over a potential range of 0-1.6 V at a sweep rate of 50 mVs^{-1} . The potential was first swept anodically up to 1.6 V and then the sweep direction was reversed. A small AuO reduction peak was observed at 1.2 V in the cathodic sweep. The total surface area of the Pt/Au core-shell was the sum of the Pt surface area, S_{Pt} , and the Au surface area, S_{Au} . The percentage of Pt coverage was calculated using $S_{\text{Pt}}/(S_{\text{Pt}} + S_{\text{Au}})$, and S_{Pt} was 0.76 cm^2 as calculated from the hydrogen underpotential deposition (HUPD) charge of Fig. 3.4, divided by the hydrogen desorption and/or adsorption density on polycrystalline Pt ($210 \mu\text{Ccm}^{-2}$). S_{Au} was determined to be 0.11 cm^2 from the AuO reduction charge around 1.2 V in Fig. 3.4, divided by $386 \mu\text{Ccm}^{-2}$. The Pt coverage percentage was approximately 88%. The electrochemical surface area (ECSA) was calculated to be $71.9 \text{ m}^2\text{g}^{-1}\text{-Pt}$ from S_{Pt} and the Pt loading on the RDE.

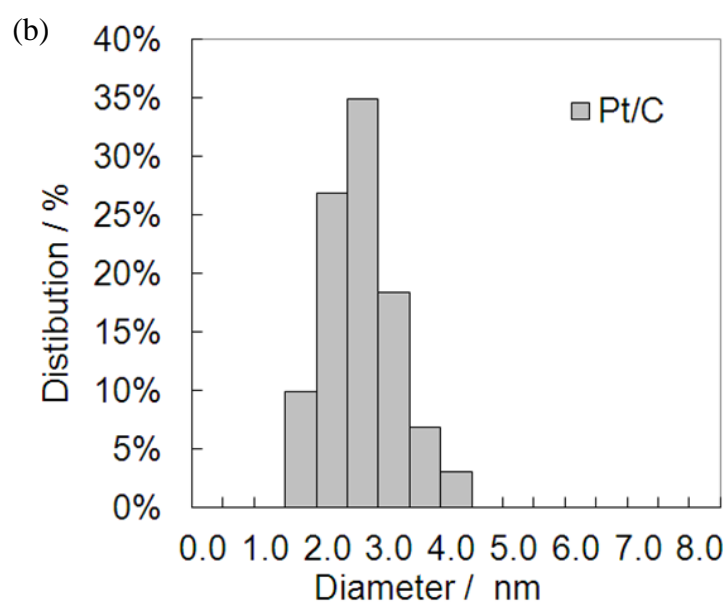
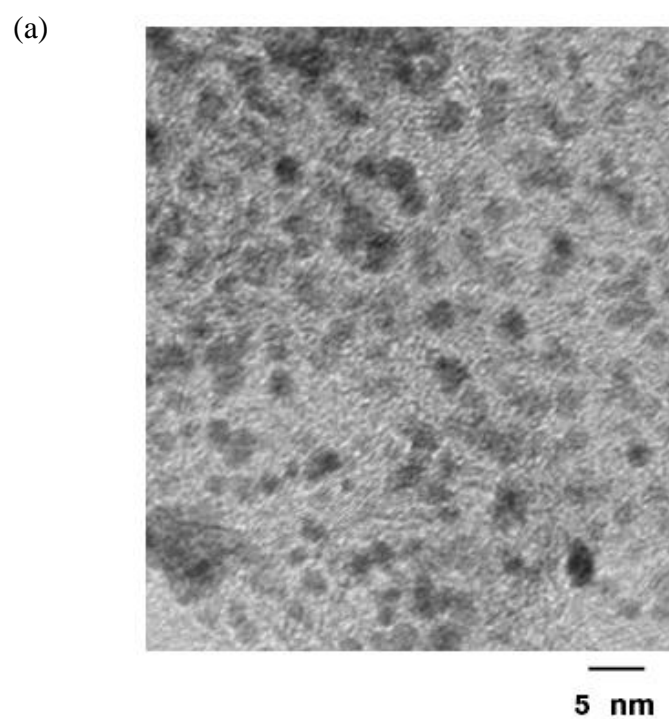


Figure 3.1 (a) TEM image of commercially available Pt/C electrocatalyst, and (b) particle size distribution of Pt/C estimated from (a).

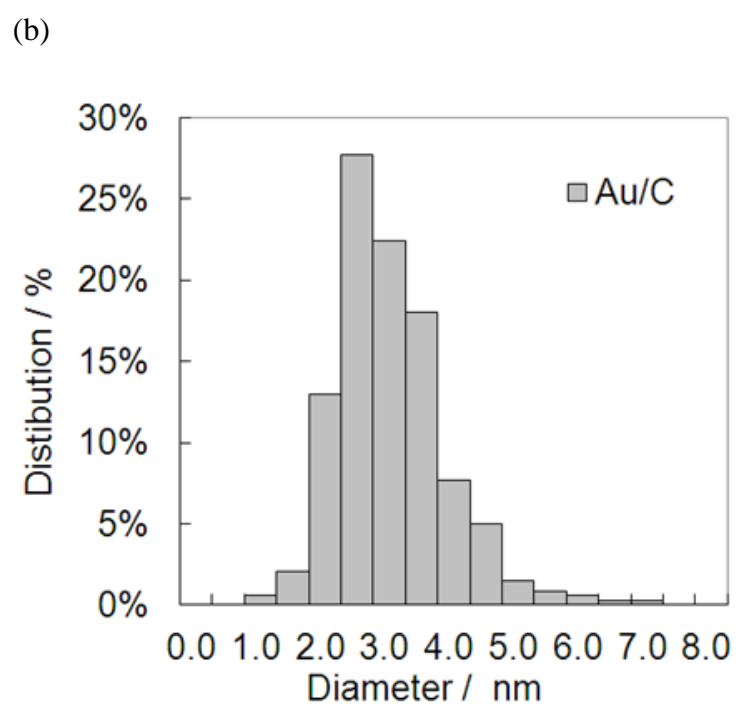
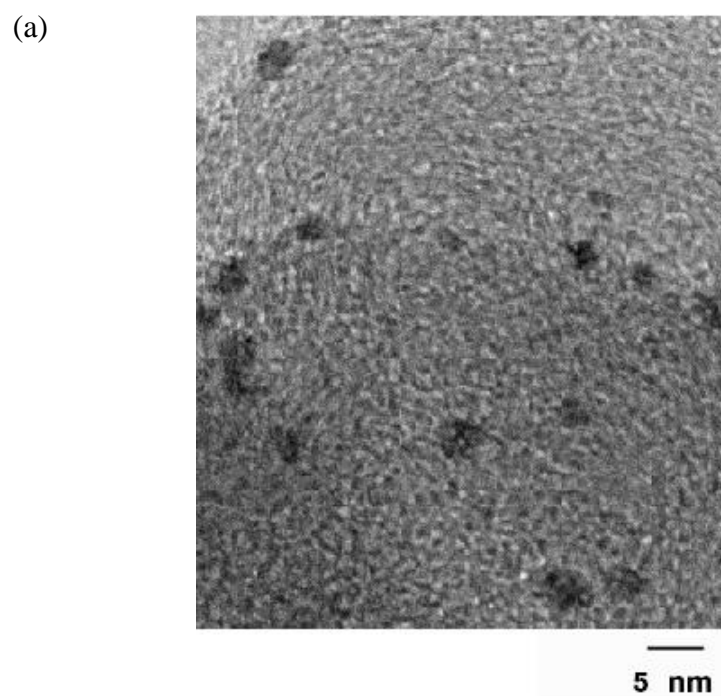


Figure 3.2 (a) TEM image of the Au/C prepared in this study, and (b) particle size distribution of Au/C estimated from (a).

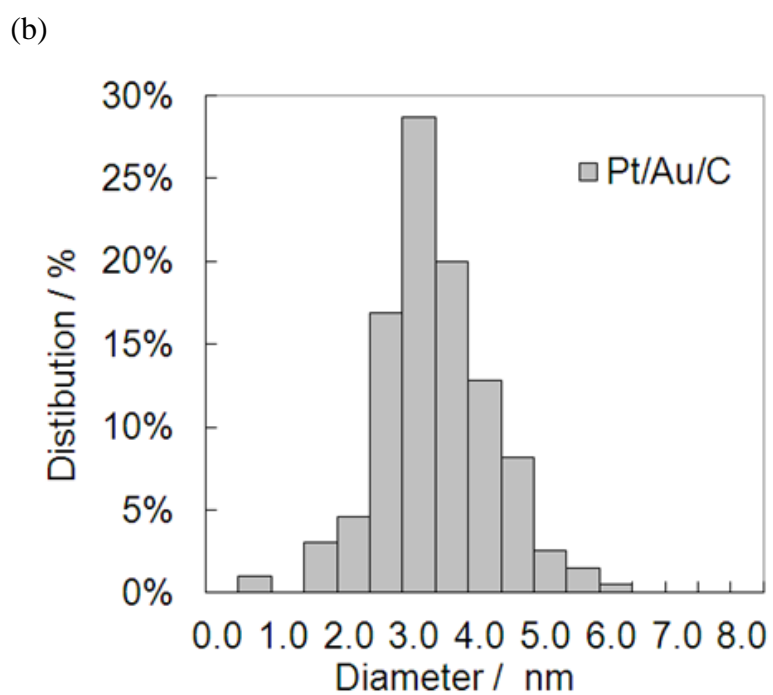
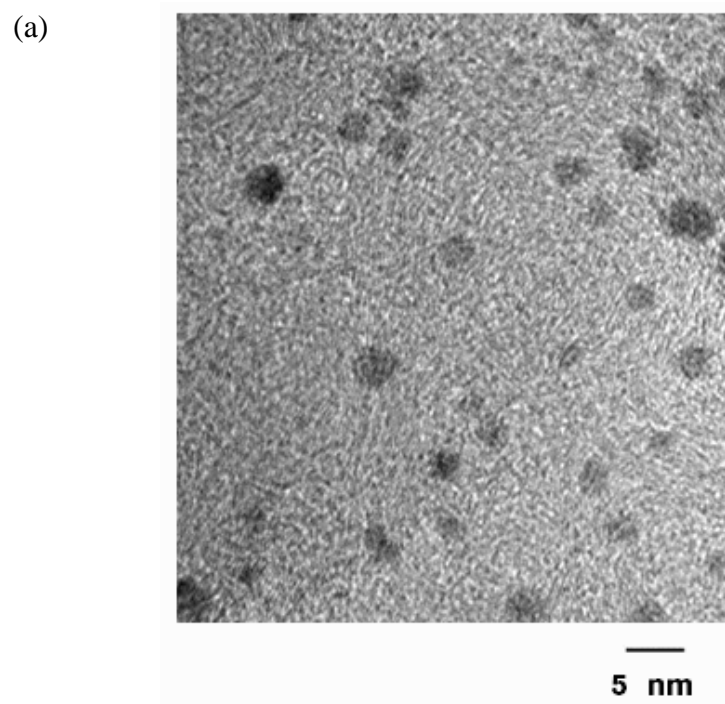


Figure 3.3 (a) TEM image of the Pt/Au/C prepared in this study, and (b) particle size distribution of Pt/Au/C estimated from (a).

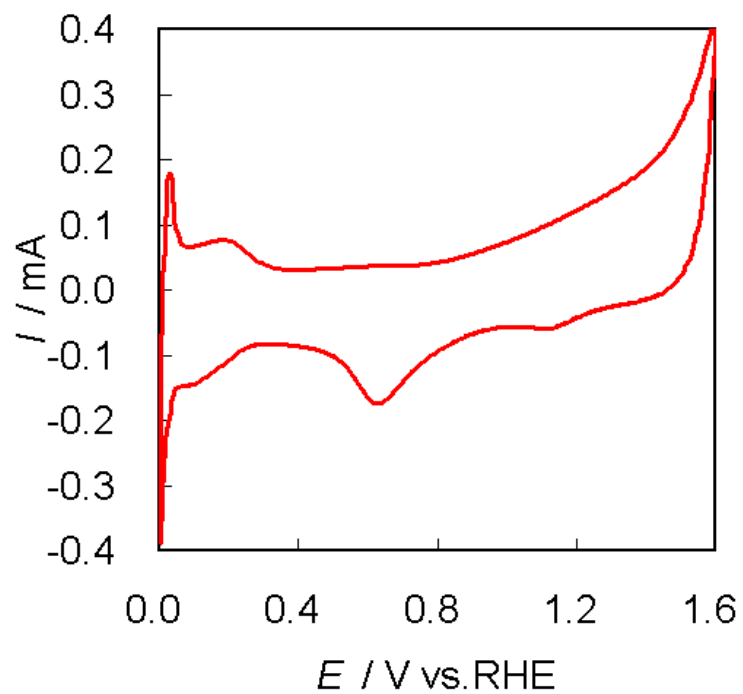


Figure 3.4 Cyclic voltammogram for the Pt/Au/C prepared core-shell electrocatalyst measured at a sweep rate of 50 mVs^{-1} .

3.3.2 ORR activity of Pt/Au/C core-shell electrocatalysts

Figure 3.5(a) shows polarization curves measured with the RDE for the Pt/Au/C electrocatalyst in 0.1 M HClO₄ solution purged with 99.99% Oxygen at various rotation speeds and at a sweep rate of 10 mVs⁻¹. The Pt loading was 5.0 μg-Ptcm⁻².

Figure 3.5(b) shows Koutecky-Levich plots, i.e., the inverse current density (1/j) plotted as a function of the inverse square root of the rotation rate ($\omega^{1/2}$) using the data in Fig. 3.5(a). The linearity and parallelism of these plots indicate first-order kinetics with respect to molecular Oxygen. The specific activity of the Pt/Au/C electrocatalyst was evaluated at an electrode potential of 0.9 V and was 571 μAcm⁻², so that the mass-specific activity was 411 Ag⁻¹. In contrast, the area-specific and mass-specific activities for the commercial Pt/C electrocatalyst were 298 μAcm⁻² and 251 Ag⁻¹, respectively. Thus, the area-specific and mass-specific activities of the Pt/Au/C electrocatalyst were 1.9 times and 1.6 times larger than those of the Pt/C electrocatalyst, respectively.

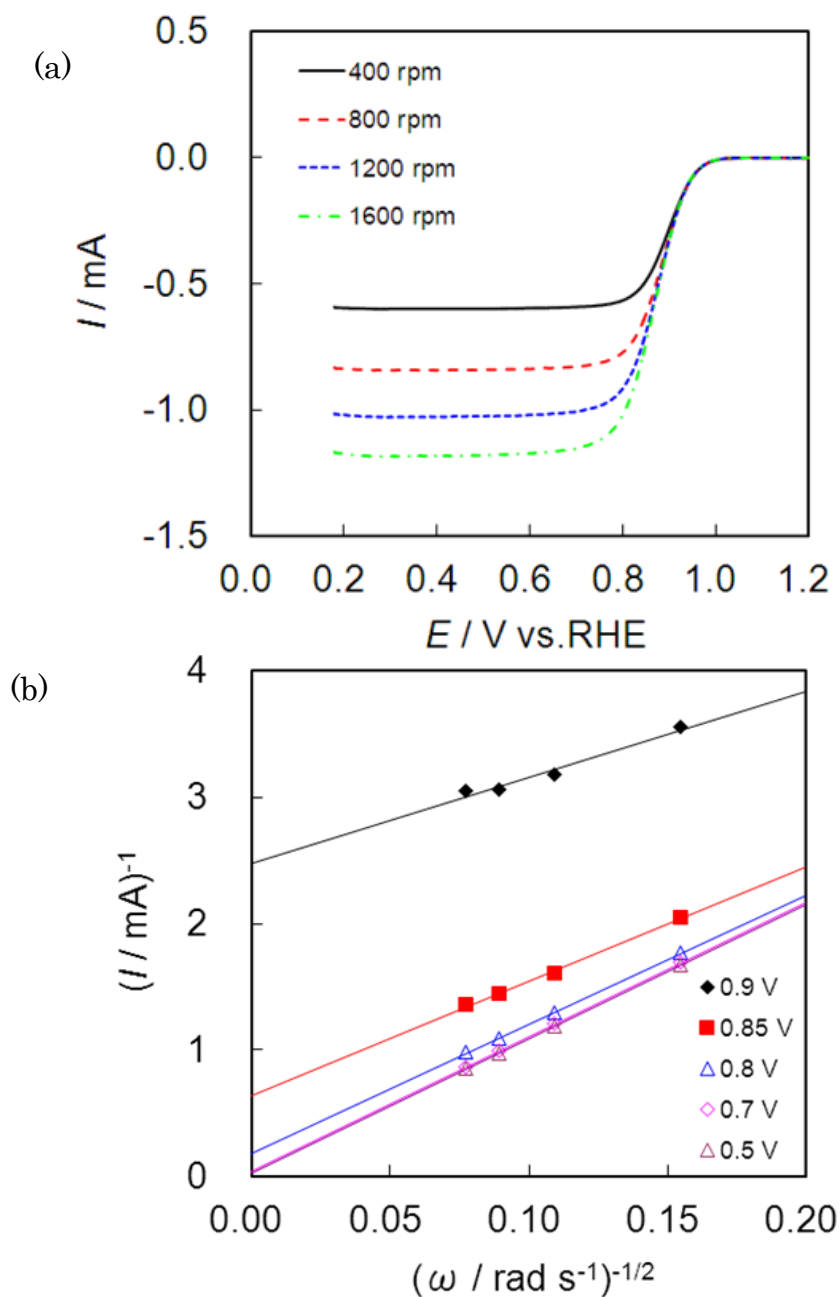


Figure 3.5 (a) ORR polarization curves measured using a RDE for Pt/Au/C core-shell electrocatalyst in 0.1 M HClO_4 . Black solid line: 400 rpm, Red broken line: 800 rpm, Blue dotted line: 1200 rpm, Green chain line: 1600 rpm. (b) Koutecky-Levich plots for ORR obtained from (a). Applied voltages were following. Black close diamond: 0.9 V, Red close square: 0.85 V, Blue open triangle: 0.8 V, Purple open diamond: 0.7 V, Brown open triangle: 0.5 V

3.3.3 XAFS analysis

3.3.3.1 Reference foils

Figure 3.6 shows the Pt K-edge XAFS spectrum and its oscillations for Pt foil. Although the Pt K-edge XAFS spectrum has a smooth edge jump due to lifetime broadening, XAFS oscillations could be observed after the appropriate background was removed, as shown in Fig. 3.6(b). The K-edge data were analyzed on the basis of the FEFF-derived phase shift and amplitude functions.¹³ The resulting values for the Pt-Pt bond distance, coordination number, and Debye-Waller factor are shown in Table 3.1. Since Au and Pt have a face-centered cubic (fcc) structure, the coordination number of the first nearest neighbor atoms is 12. To obtain this coordination number, the mean free path was set to 0.24 nm, which was shorter than the mean free path of 0.65 nm in the L_{III}-edge XAFS, due to the lifetime broadening effect as reported by Nishihata *et al.*¹⁴ This free path value (0.24 nm) was used for further curve fitting of the Pt K-edge data.

Figures 3.7(a) and (b) show the Au K-edge XAFS spectrum and its oscillations for Au foil. A smooth edge jump was observed, as for the Pt foil in Fig. 3.6(a). The K-edge data were analyzed on the basis of the FEFF-derived phase shift and amplitude functions.¹³ The resulting values for the Au-Au bond distance, coordination number, and Debye-Waller factor are shown in Table 3.1. The mean free path was set to 0.21 nm to give a coordination number of 12.

Comparing the Pt-Pt distances for the K-edge and L_{III}-edge shown in Table 3.1, the Pt-Pt distance of the L_{III}-edge was 0.003 nm shorter than that of the K-edge. The same tendency was also observed in the Au-Au bond distances. Accordingly, the bond distance obtained from curve fitting of the K-edge was considered to be longer than that derived from the L_{III}-edge, though the reason for this discrepancy remains unknown and elusive.

Figures 3.8(a) and (b) show the Pt K-edge XAFS spectrum and its oscillations for Au-Pt (1/9) foil. Although the phase shifts $\phi_j(k)$ and amplitude functions $F_j(k)$ of Pt

and Au atoms are so close that discrimination is difficult, the metallic radii of Pt and Au differ by about 0.005 nm; this is sufficient to create a phase difference in the oscillations, so that Pt-Pt and Pt-Au contributions can be distinguished with careful analysis. A one-shell curve fitting for the Pt-Au bond was first conducted for the Au-Pt foil in an attempt to distinguish Pt and Au by the difference in bond distance. The resulting curve-fitting parameters are shown in Table 3.1. The coordination number was less than 12, probably because residual Pt-Pt interactions were neglected. A two-shell curve fit was then conducted using different bond distances to separate the Pt-Pt and Pt-Au shells. In the two-shell fitting, the value of ΔE_0 for the Pt-Pt bond was fixed at the value for Pt foil. Consequently, a total coordination number of almost 12 was obtained. The Pt-Au bond distance obtained from the curve fitting was between the Pt-Pt and Au-Au bond distances of the pure foils.

Table 3.1 Curve-fitting results for reference foils

Sample	Edge	Bond	Coordination number	Inter atomic distance / nm	Debye-Waller factor / nm	
Pt foil	Pt-L _{III}	Pt-Pt	(12)	0.275 ± 0.001	0.0071 ± 0.0004	
	Pt-K	Pt-Pt	(12)	0.278 ± 0.001	0.0065 ± 0.0004	
Au foil	Au-L _{III}	Au-Au	(12)	0.284 ± 0.001	0.0080 ± 0.0002	
	Au-K	Au-Au	(12)	0.286 ± 0.001	0.0080 ± 0.0005	
Au-Pt (1/9) foil	One Shell	Pt-K	Pt-Au	10.5 ± 1.3	0.282 ± 0.001	0.0078 ± 0.0003
		Pt-K	Pt-Pt	1.2 ± 0.7	0.277 ± 0.003	0.0072 ± 0.0023
	Two shell	Pt-K	Pt-Au	10.8 ± 1.1	0.283 ± 0.001	0.0077 ± 0.0003

* Values in parenthesis were fixed.

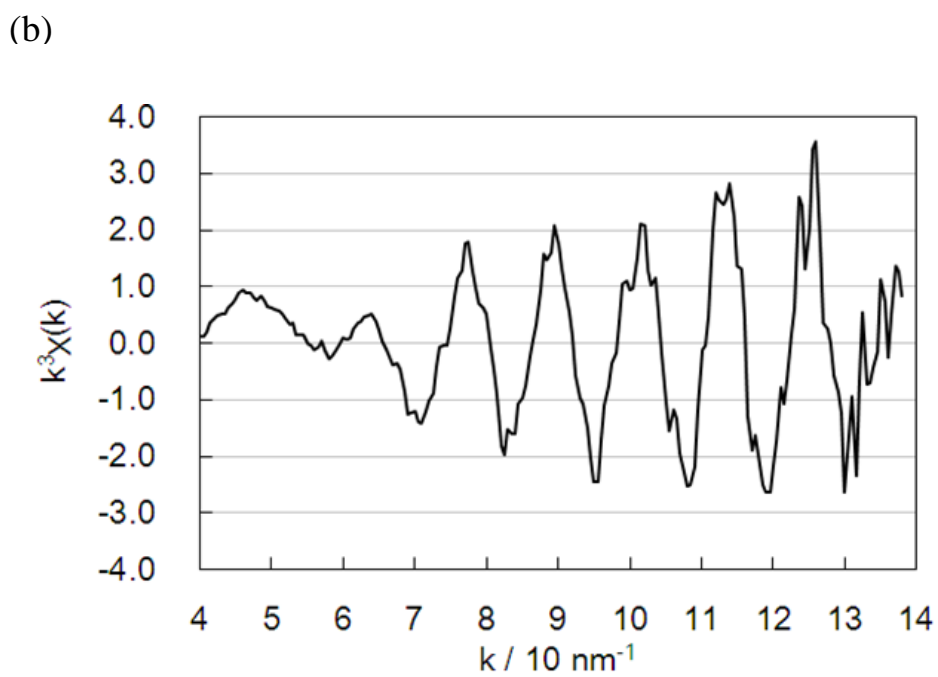
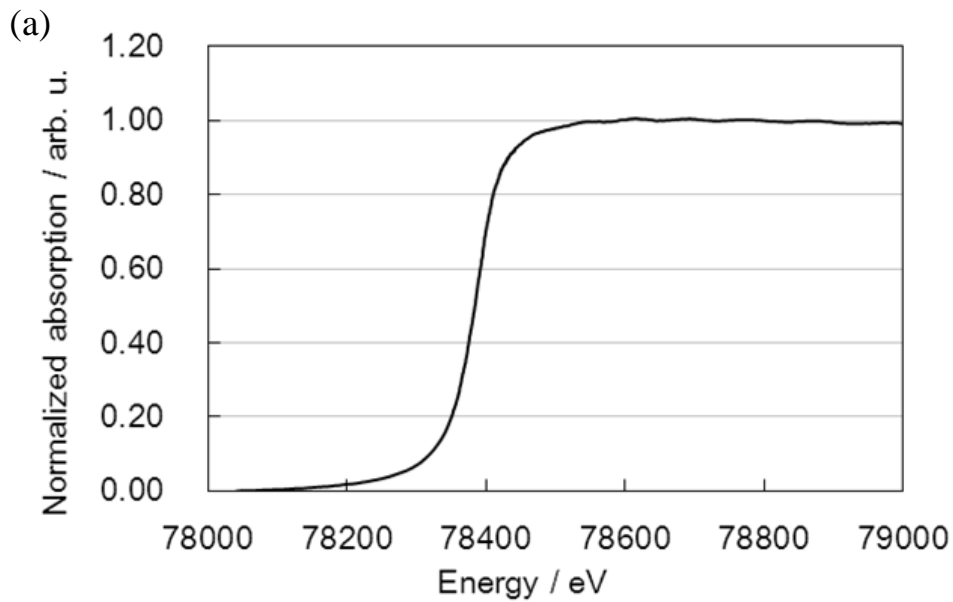


Figure 3.6 (a) Pt K-edge spectra for Pt foil, and (b) k^3 -weighted XAFS oscillation after background subtraction of spectrum (a).

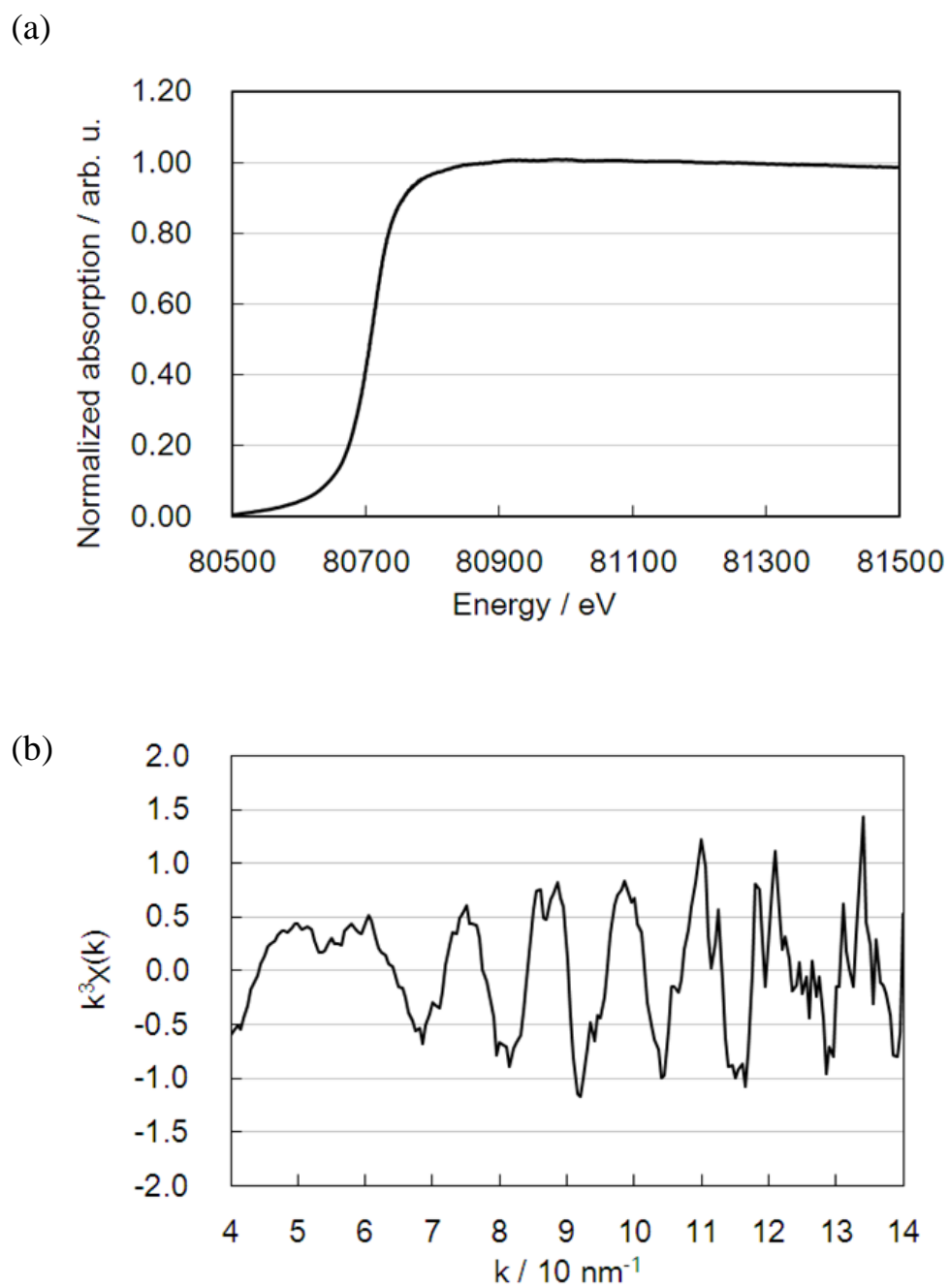


Figure 3.7 (a) Au K-edge spectra for Au foil, and (b) k^3 -weighted XAFS oscillation after background subtraction of spectrum (a).

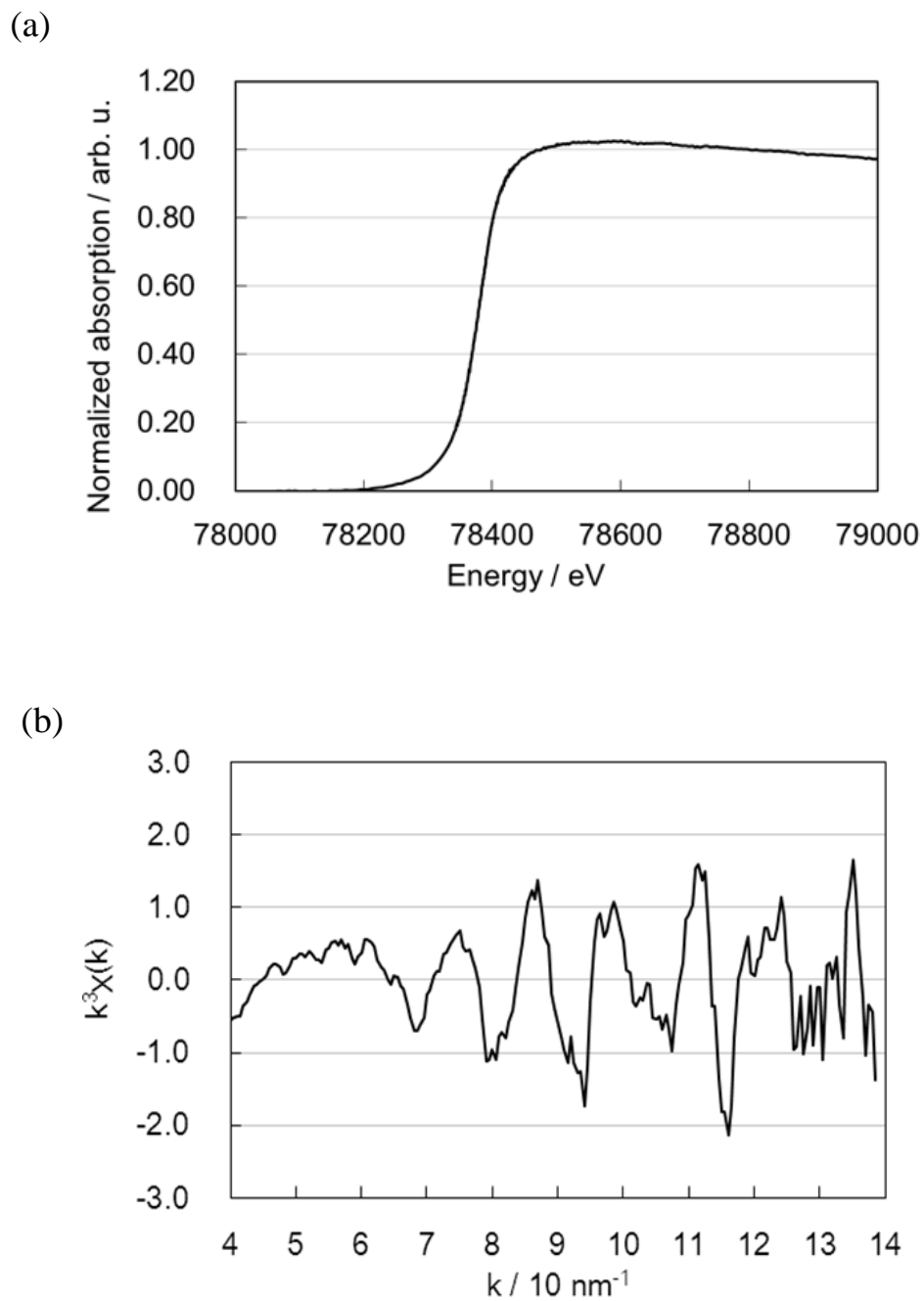


Figure 3.8 (a) Pt K-edge spectra for Pt/Au (1/9) random alloy solid solution foil, and (b) k^3 -weighted XAFS oscillation after background subtraction of spectrum (a).

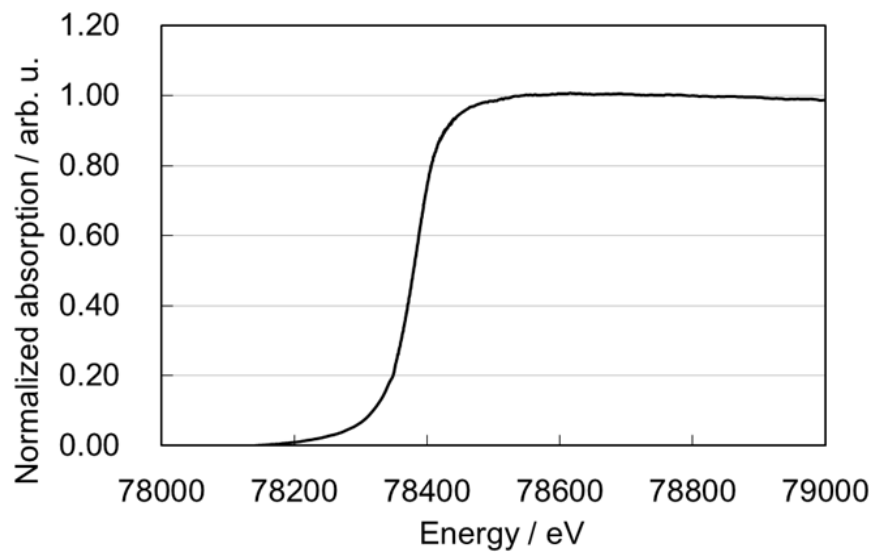
3.3.3.2 Pt/C electrocatalyst

Figures 3.9 and 3.10 show the Pt K-edge and L_{III}-edge absorption spectra and the k³-weighted XAFS oscillations for Pt/C, respectively. The oscillations amplitude for Pt/C were smaller than those for the Pt foil, which indicates a smaller coordination number and the presence of nanoparticles. The coordination number and bond distance given in Table 3.2 have errors of 2.3 and 0.001 nm, respectively. However, the bond distance obtained from a K-edge curve fitting was 0.004 nm longer than that for the L_{III}-edge. The longer distance from the K-edge analysis than that from the L_{III} edge corresponds to that found in the XAFS analyses of the Pt foil and Au foil.

Table 3.2 Curve-fitting results for Pt/C at 0.4 V vs. RHE

Sample	Edge	Bond	Coordination number	Interatomic distance / nm	Debye-Waller factor / nm
Pt/C	Pt-L _{III}	Pt-Pt	9.3 ± 2.3	0.273 ± 0.001	0.0085 ± 0.0006
	Pt-K	Pt-Pt	9.6 ± 2.0	0.277 ± 0.001	0.0078 ± 0.0003

(a)



(b)

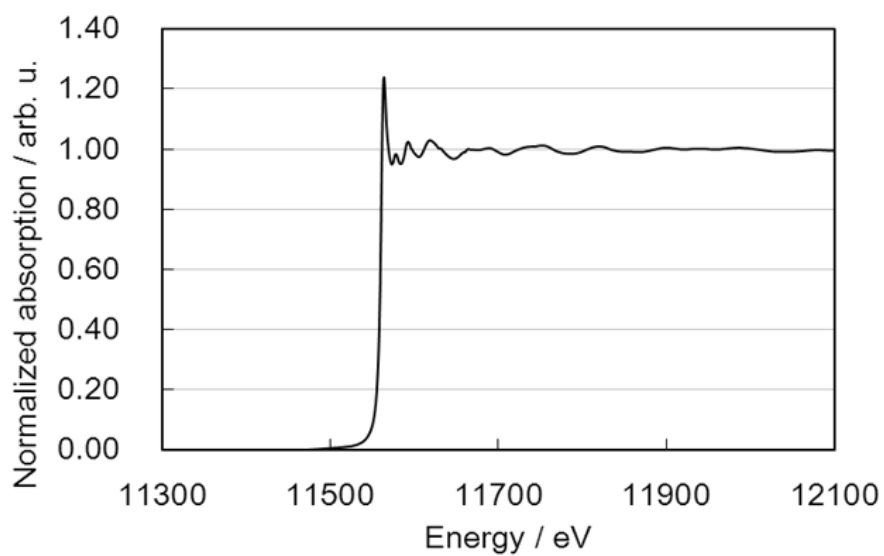


Figure 3.9 (a) Pt K-edge and (b) Pt L_{III}-edge XAFS spectra for Pt/C at 0.4 V vs. RHE.

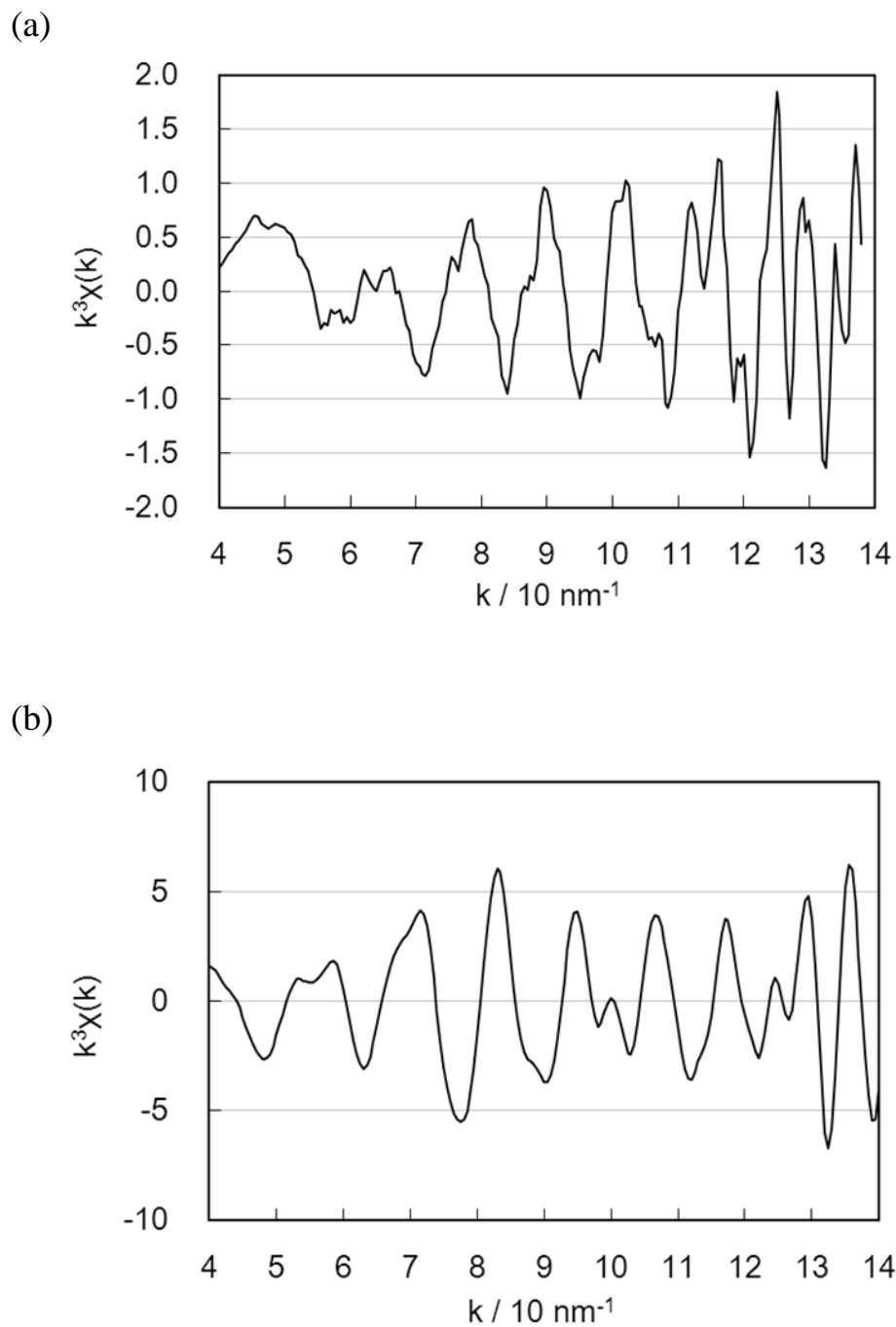


Figure 3.10. (a) Pt K-edge and (b) Pt L_{III}-edge k^3 -weighted XAFS oscillations for Pt/C at 0.4 V vs. RHE after background subtraction and normalization of the spectrum in Fig. 3.9.

3.3.3.3 Pt/Au/C core-shell electrocatalyst

Figures 3.11(a) and (b) show the Pt and Au K-edge k^3 -weighted XAFS oscillations for Pt/Au/C. The Pt K-edge XAFS oscillations with $S/N > 1$ were observed up to 120 nm^{-1} , as shown in Fig. 3.11(a). Compared with Pt and Au K-edge XAFS, the oscillation of the Au K-edge was larger and lasted longer, which was more evident in the inversely Fourier filtered data in Figure 3.12. This means that Au had a larger coordination number and less disorder than Pt. The data were further analyzed by curve fitting to obtain structural parameters. Because the difference of phase shift and amplitude functions are not so much in Au and Pt, one-shell curve-fitting analyses of the Pt and Au K-edges were conducted for the Pt-Pt and Au-Au bonds, respectively in order to have an approximate image. The results are given in Table 3.3. The Pt-Pt bond distance in the Pt/Au/C alloy was almost the same as that for Pt/C. However, the Au-Au bond distance was shorter than that for the Au foil, and the contraction in bond distance was 0.006 nm . In addition, the coordination number for Au-Au was large (almost 12), which was close to that for the Au foil and was significantly different from that for Au nanoclusters. In contrast, the coordination number for Pt-Pt was around 6. These coordination numbers are consistent with the core-shell model, in which more Pt than Au is on the surface.

Table 3.3 Results from one-shell curve fit for Pt/Au/C

Absorbing metal	Scattering metal	Coordination number	Bond distance / nm	Debye-Waller factor / nm
Pt	Pt	6.8 ± 1.2	0.278 ± 0.002	0.0096 ± 0.0006
Au	Au	11.3 ± 3.4	0.280 ± 0.002	0.0072 ± 0.0011

To probe the structures in more detail, two-shell curve-fitting analyses for Pt and Au K-edges were conducted. To reduce the number of fitting parameters, values of ΔE_0 for Au-Au, Pt-Pt, and Pt-Au were fixed to those for the corresponding reference foils,

and the value of ΔE_0 for Au-Pt was fixed at 5.0 eV. The uncertainty (± 10 eV) in ΔE_0 for the Au-Pt bond gave rise to errors in bond lengths of approximately 1%. Table 3.4 shows the structural parameters obtained from the curve-fitting analysis. The bond distances and coordination numbers of Pt-Au and Au-Pt obtained from Pt and Au K-edge fits satisfied the conditions given in Eqs. (6) and (7) of section 3.2.4 within the error. The distance for Pt-Au was longer than that for Pt-Pt obtained from the one-shell curve fitting. The Au-Au bond distance from the two-shell curve fitting was longer than that from the one-shell fitting. This can be explained by the presence of Au-Pt bonding, which should have a bond length between those of Pt-Pt and Au-Au. The Au-Au distance was shorter than that for the Au foil, and the total coordination number of Au-Au + Au-Pt = 12.4 was close to that expected from the model of the Au core. However, the total coordination number of Pt-Au + Pt-Pt (=9.2) was much smaller than that for the Pt foil; these coordination numbers demonstrate the Pt shell/Au core structure. As discussed later in section 3.4.1, the “two-shell Pt on Au core” model nanocluster with a diameter of 3.0 nm provided a total coordination number of 8.7, which corresponds to the observed value.

Table 3.4 Results from two-shell curve fits for Pt/Au/C

Absorber	Scattering metal Pt			Scattering metal Au		
	N	r / nm	DW / nm	N	r / nm	DW / nm
Pt	7.2	0.275	0.0097	2.0	0.279	0.008
	± 2.9	± 0.003	± 0.0006	± 0.8	± 0.004	± 0.001
Au	2.7	0.279	0.005	9.7	0.282	0.007
	± 2.7	± 0.005	± 0.001	± 2.9	± 0.003	± 0.001

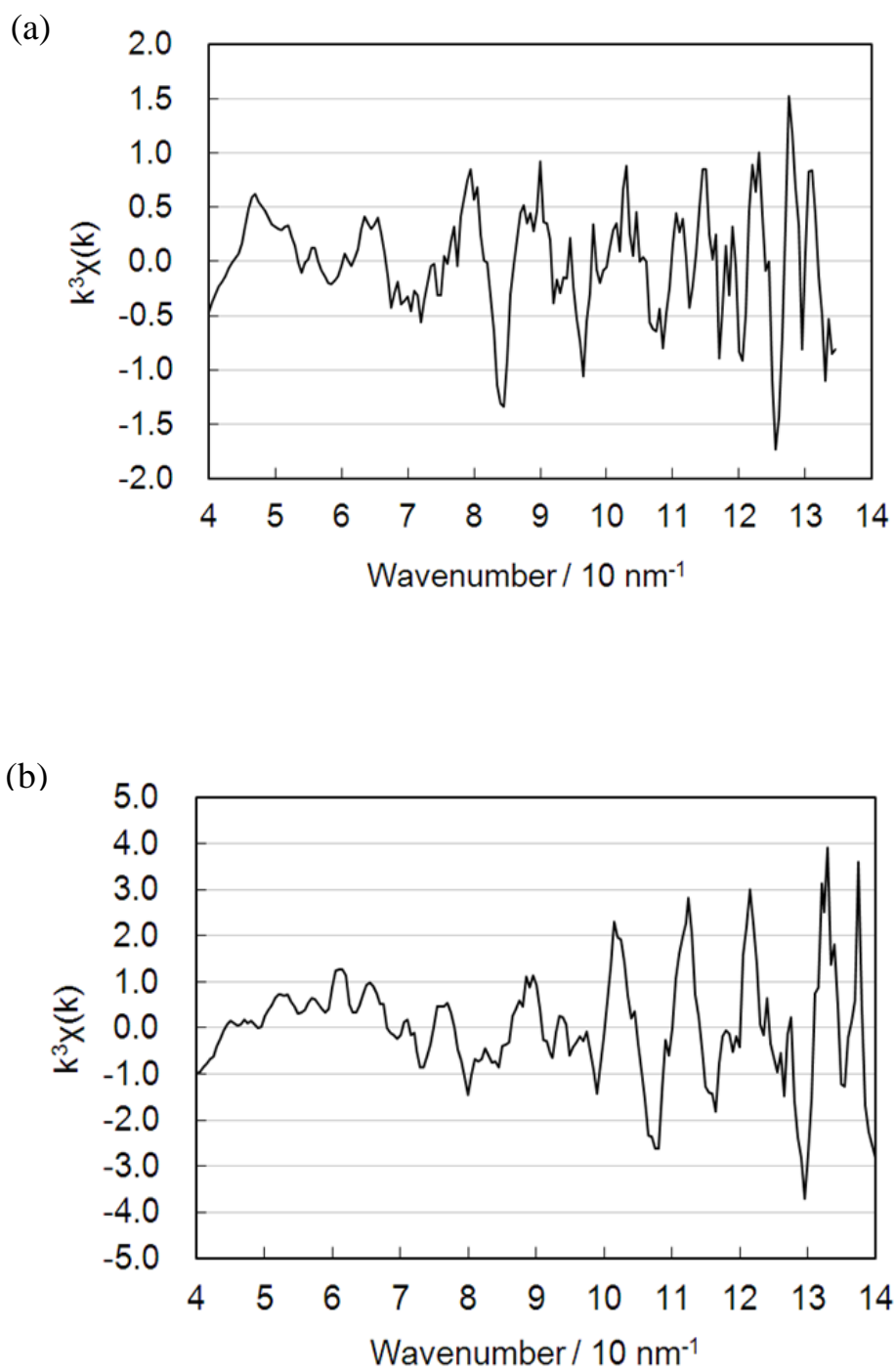


Figure 3.11 (a) Pt K-edge and (b) Au K-edge k^3 -weighted XAFS oscillations of Pt/Au/C at 0.4V vs. RHE.

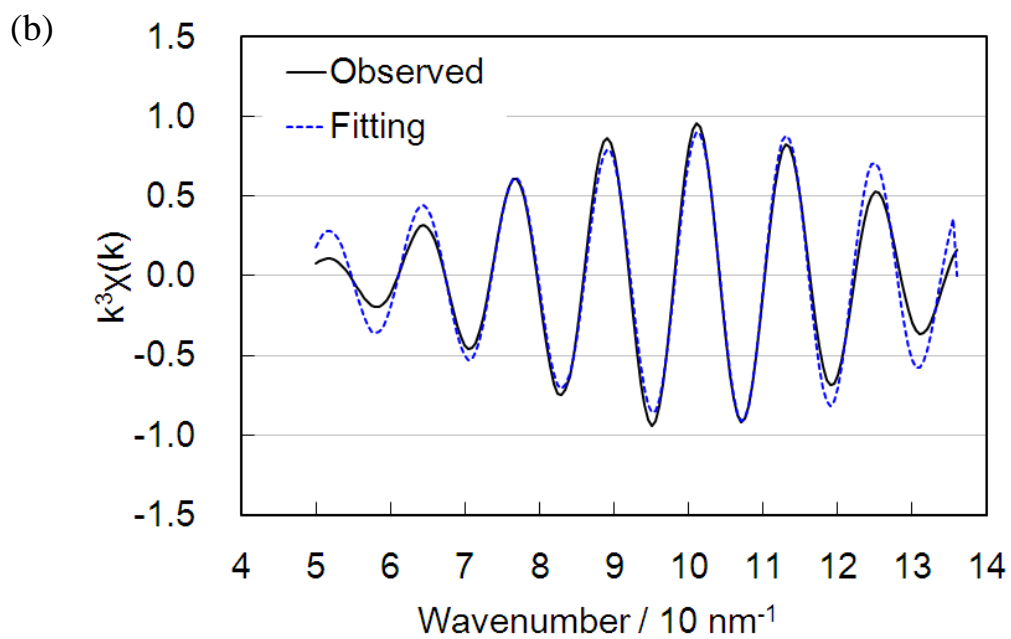
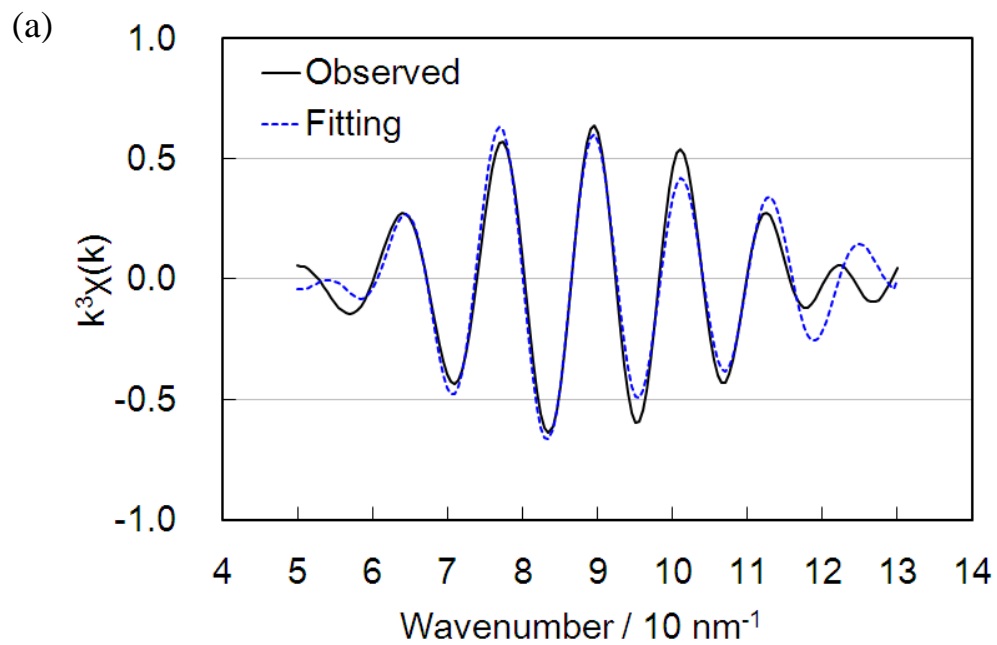


Figure 3.12 Curve fitting data of (a) Pt K-edge and (b) Au K-edge XAFS. Black solid line is Fourier filtered data and Blue broken line is fitted data. Fourier range = 50-130 nm^{-1} and inverse Fourier range = 0.15-0.35 nm for Pt and Fourier range = 50-136 nm^{-1} and inverse Fourier range = 0.15-0.35 nm for Au.

3.4 Discussions

3.4.1 Estimation of Pt/C and Pt/Au/C core-shell electrocatalyst structures

3.4.1.1 Estimation of the structure of Pt/C nanocluster

There are two possible structures in nanoclusters, icosahedral and cuboctahedral structure in the literature. Judging from the particle size, we assumed the cuboctahedral structure in this paper.¹⁵ Based on an average diameter of 2.2 nm and the cuboctahedron model, the particles have 4-atom edges (1.9 nm in diameter, 147 atoms) or 5-atom edges (2.4 nm in diameter, 309 atoms). Figure 3.12(a) shows a 309-atom cuboctahedron with 5-atom edges. The average coordination numbers for all Pt atoms calculated from the 4-atom edge and 5-atom edge models were 9.0 and 9.6, respectively, which are in good agreement with those obtained from the K-edge/L_{III}-edge XAFS curve fit given in Table 3.2 (9.6±2.0 and 9.3±2.3, respectively). Therefore, the Pt-on-carbon nanocluster was a cuboctahedral structure with 4-atom or 5-atom edges.

3.4.1.2 Estimation of the structure of Pt/Au/C

The XAFS results revealed that the coordination number derived from Au K-edge EXAFS oscillations was larger than that derived from the Pt K-edge data, which indicates a structure composed of a Au-rich core and a Pt-rich shell. Although Strbac *et al.* suggested that the Au (111) single crystal was partially covered with Pt,¹⁶ the total coordination number of Au was almost 12, which indicates that the Au nanoparticle was almost fully covered with Pt. Cyclic voltammetry also showed that mostly Pt occupied the surface of the nanocluster surface. Although the reaction mechanism of H₂PtCl₆ with the Au nanoparticle is still unknown, a Pt shell can be easily prepared around the Au core by this simple reaction.

The Pt/Au core-shell structure was further analyzed based on the XAFS, ICP, and TEM data. ICP analysis showed that the bulk Au:Pt ratio was 1.1. From the particle sizes of Au and Pt/Au (2.6 and 3.0 nm, respectively), we propose a cuboctahedral model

with 659 atoms, as shown in Fig. 3.12(b) and (c). In this structure, 309 Au atoms are located inside the nanocluster, while 350 Pt atoms cover the Au nanoclusters in two layers. The estimated core-shell model is shown in Fig. 3.12(c). The coordination numbers of the Pt/Au structure in Fig. 3.12(c) are given in Table 3.5. The coordination numbers obtained from the curve fits in Table 3.4 correspond to those expected. Thus, we propose the model structure shown in Fig. 3.12(c), where the Au core is partially covered with two layers of Pt atoms.

Table 3.5 Coordination numbers of estimated Pt/Au/C structure

Coordination number		
Absorbing metal	Scattering metal Pt	Scattering metal Au
Pt	6.7	2.1
Au	2.3	9.6

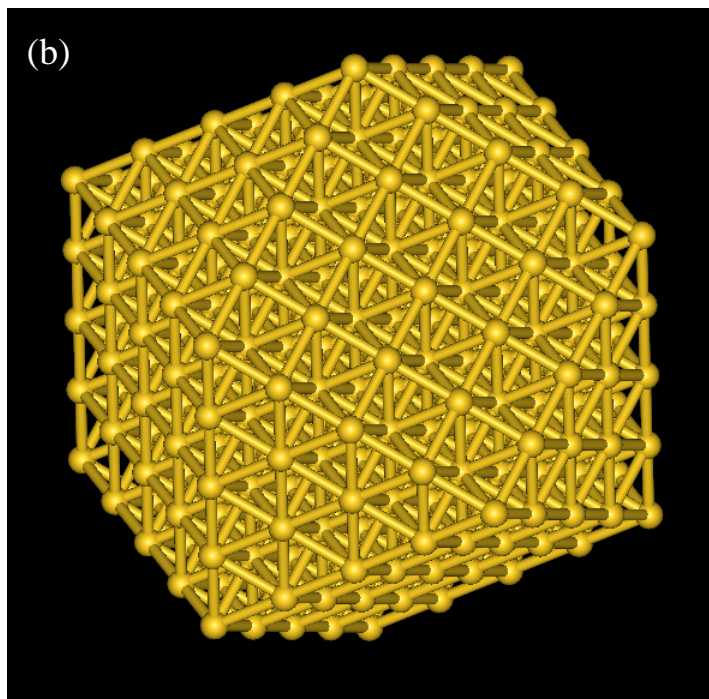
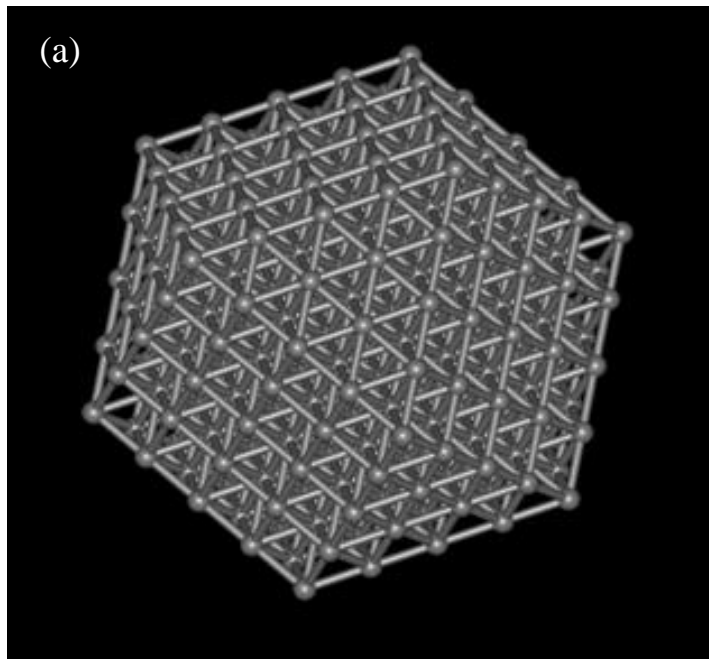


Figure 3.12 Estimated structures of (a) Pt cuboctahedron, (b) Au cuboctahedron,

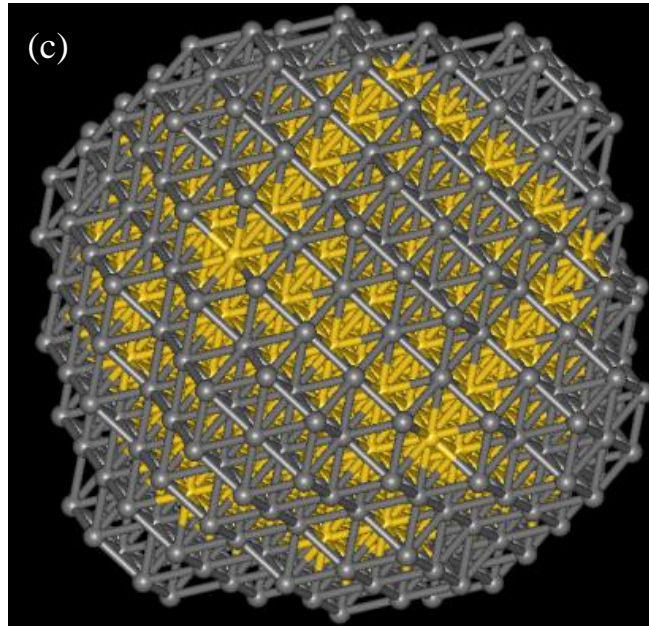


Figure 3.12 Estimated structures of (c) Pt/Au core-shell particle.

3.4.2 Bond length and electrochemical ORR activity of Pt/Au/C

Table 3.4 shows that the Au-Au and Pt-Pt distances for the Pt/Au/C core-shell electrocatalyst were shorter than the corresponding distances in the Au and Pt foils. The Pt-Pt distance in Pt/C was slightly shorter than that in the Pt foil, as shown in Table 3.3. The Pt-Pt distance for Pt/Au/C was even shorter than that for Pt/C. The Au-Au bond distance in the Pt/Au/C was also shorter than that in the Au foil. Pt and Au atoms generally form fcc lattices, where the Pt lattice constant is smaller than that of the Au lattice; therefore, a Pt atomic layer on an Au lattice is expected to have elongated Pt-Pt distances due to the influence of the Au lattice. This expansion of the Pt-Pt distance was observed in epitaxially grown Pt on an Au (111) surface. However, the Pt-Pt distance obtained for the two-shell curve fitting was not elongated, but instead the Au-Au distance was largely contracted. This is due to the strong Pt-Pt bond, which induces contraction of the Au core. This may be due to the labile properties of nanoclusters.

According to Adzic *et al.*¹⁷ and Mukerjee *et al.*¹⁸, shorter Pt-Pt distances contribute to enhanced area-specific activity for the ORR. A comparison of the Pt-Pt distance obtained in Pt/Au/C with the relationship between the Pt-Pt distance and ORR area-specific activity reported by Mukerjee *et al.*¹⁸ indicates that the Pt-Pt distance found in Pt/Au/C was in the range that can explain the high area-specific activity. The XAFS results suggest that the core-shell structure and contraction of the Pt-Pt distances, which are considered to be related to the high ORR area-specific activity in the Pt/Au/C core-shell electrocatalysts. The Pt-Au nanocluster has an unexpected structure, *i.e.*, the Pt-Pt distance is shorter than that of Pt foil. The X-ray near edge structure of Pt L_{III}-edge was measured and showed a larger d-vacancy than those for Pt foil and Pt/C, as shown in Fig. 3.13. Pt 5d vacancies were determined by the procedure reported by Mansour *et al.*^{19,20} This is another unexpected result because electron transfer from Au to Pt should occur. The Pt L_{III} edge for Pt-Au foil shows a smaller d vacancy by electron transfer from Au, as shown in Fig. 3.13. However, it can be confirmed that

the Pt/Au nanoparticle should have a different structure and electronic properties from those of Pt deposited on an Au single crystal surface and PtAu bulk alloy.

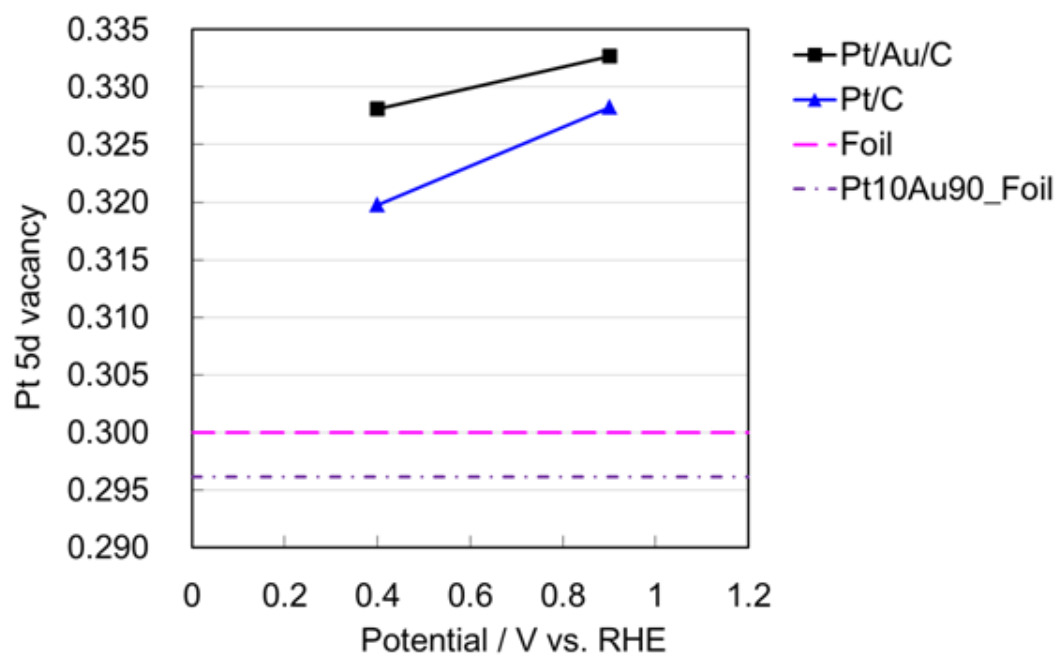


Figure 3.13 Pt d vacancy calculated from Pt L_{III} and Pt L_{II} edge XANES

3.4.3 The origin of Pt-Pt contraction of Pt/Au/C

As describe in the previous section Pt-Pt distance of Pt shell of Pt/Au was much shorter than that of Au core. In addition it was shorter than that of Pt/C. However the reason of contraction remains still elusive. To reveal the mechanism of contraction Ohwaki *et al.* studied²¹ using large-scale density functional theory calculation, which is the natural bond orbitals (NBOs) method^{22,23} with calculation program of Open MX.²⁴ NBOs method provides a Lewis-structure type orbital representation expressing localized bonding and lone pair. Hence one can analyze properties of chemical bonds, intermolecular interactions, and chemical reactivity. They constructed the Pt₃₅₀/Au₃₀₉ core-shell model shown in Fig. 3.12, then conducted the structural relaxation calculation.

According to their result surface Pt-Pt distance was less than 0.280 nm. On the other hand, although the Au-Au distance of Au core was mainly less than 0.290 nm, Au-Au distance of the some atoms of the surface of Au core, which directly interact with the Pt shell, was shorter than 0.290 nm. Au-Au distance was contracted by the existence of Pt shell which has atomic distance shorter than that of Au-Au. The experimental result was validated and justified by the theoretical calculation.

The remaining elusive question is the reason of contraction of Pt-Pt distance of Pt shell. The reason of Pt-Pt contraction is thought to be the weak interaction energy between Pt shell and Au core. Pt atoms are considered to be easily slipped on the Au core. In order to reveal it, the interaction energy between Pt shell and Au core has to be calculated and compared with that of Pt nanocluster. Interaction energy would be determined by subtracting the total energy of Pt₃₅₀ hollow structure only and Au₃₀₉ core structure only from the total energy of Pt₃₅₀Au₃₀₉ core-shell structure. To determine the interaction energy of Pt nanocluster, the energy of Pt₃₅₀ hollow, Pt₃₀₉ cuboctahedral core only, and Pt₆₅₉ nanocluster has to be calculated, respectively. The interaction energy of Pt shell and Pt core would be determined by subtracting the total energy of Pt₃₀₉ and Pt₃₅₀ from that of Pt₆₅₉ nanocluster as in the case of Pt/Au core-shell. This is

the future work.

3.5 Conclusions

A carbon-supported Pt-shell Au-core electrocatalyst (Pt/Au/C) was prepared by sequential deposition of Pt ions on the surface of Au nanoclusters. The nanoclusters were prepared by the sputter-deposition-onto-ionic-liquid method and supported on carbon. The ORR area-specific activity for the prepared Pt/Au/C in 0.1 M HClO₄ aqueous solution was approximately 2 times higher than that of a commercial carbon-supported Pt/C electrocatalyst. The Pt/Au core-shell structure was confirmed by electrochemical methods and XAFS analysis. The Pt-Pt bond distance for Pt/Au/C obtained from the XAFS analysis was not elongated by interactions with the Au atoms in the core. Instead, the Pt-Pt bond distance was slightly contracted even compared to that of Pt/C. The core-shell structure and the contraction of the Pt-Pt distance on the Au core must cause high area-specific activity.

3.6 References

- ¹ Inaba, M.; Tsuji, H., Platinum Core-Shell Catalyst Manufacturing Method, and Fuel Cell using Catalyst, Japan Patent, WO2011115012 A1, March 19 2010.
- ² Tsuji, H.; Kaneko, A.; Banno, M.; Yamada, H.; Saito, M.; Tasaka, A.; Inaba, M., A Novel Technique for Preparation of Pt shell/Au core/C Core-Shell Catalysts and Their Activity for Oxygen Reduction Reaction. In 218th ECS Meeting Abstracts Las Vegas, 2010; Vol. MA2010-02, p. 858.
- ³ Torimoto, T.; Okazaki, K.-i.; Kiyama, T.; Hirahara, K.; Tanaka, N.; Kuwabata, S., Sputter deposition onto ionic liquids: Simple and clean synthesis of highly dispersed ultrafine metal nanoparticles. *Applied Physics Letters* **2006**, *89*(24), 243117-3.
- ⁴ Hatakeyama, Y.; Takahashi, S.; Nishikawa, K., Can Temperature Control the Size of Au Nanoparticles Prepared in Ionic Liquids by the Sputter Deposition Technique? *The Journal of Physical Chemistry C* **2010**, *114*(25), 11098-11102.
- ⁵ Hatakeyama, Y.; Onishi, K.; Nishikawa, K., Effects of sputtering conditions on formation of gold nanoparticles in sputter deposition technique. *RSC Advances* **2011**, *1*(9), 1815-1821.
- ⁶ Cook, J. J. W.; Sayers, D. E., Criteria for automatic x-ray absorption fine structure background removal. *Journal of Applied Physics* **1981**, *52*(8), 5024-5031.
- ⁷ Asakura, K., Analysis of XAFS, in *X-ray Absorption Fine Structure for Catalysts and Surfaces*, Iwasawa, Y. Ed.; World Scientific: Singapore, 1996; pp 35-58.
- ⁸ Rehr, J. J.; Albers, R. C., Theoretical approaches to x-ray absorption fine structure. *Reviews of Modern Physics* **2000**, *72*(3), 621-654.
- ⁹ Bian, C.-R.; Suzuki, S.; Asakura, K.; Ping, L.; Toshima, N., Extended X-ray Absorption Fine Structure Studies on the Structure of the Poly(vinylpyrrolidone)-Stabilized Cu/Pd Nanoclusters Colloidally Dispersed in Solution. *The Journal of Physical Chemistry B* **2002**, *106*(34), 8587-8598.
- ¹⁰ Asakura, K.; Yamazaki, Y.; Kuroda, H.; Harada, M.; Toshima, N., A "Cluster-in-Cluster" Structure of the SiO₂-Supported PtPd Clusters. *Japanese Journal of Applied Physics* **1993**, *32*(S2), 448.
- ¹¹ Via, G. H.; Drake, K. F.; Meitzner, G.; Lytle, F. W.; Sinfelt, J. H., Analysis of EXAFS data on bimetallic clusters. *Catalysis Letters* **1990**, *5*(1), 25-33.
- ¹² Hamilton, W., Significance tests on the crystallographic R factor. *Acta Crystallographica* **1965**, *18*(3), 502-510.
- ¹³ Teo, B. K.; Antonio, M. R.; Averill, B. A., Molybdenum K-edge extended x-ray absorption fine structure studies of synthetic molybdenum-iron-sulfur clusters containing the MoS₄ unit: development of a fine adjustment technique based on models. *Journal of the American Chemical Society* **1983**, *105*(12), 3751-3762.
- ¹⁴ Nishihata, Y.; Emura, S.; Maeda, H.; Kubozono, Y.; Harada, M.; Uruga, T.; Tanida, H.; Yoneda, Y.; Mizuki, J.; Emoto, T., XAFS spectra in the high-energy region measured at SPring-8. *Journal of Synchrotron Radiation* **1999**, *6*(3), 149-151.
- ¹⁵ Baletto, F.; Ferrando, R., Structural Properties of Nanoclusters: Energetic, Thermodynamic, and Kinetic Effects, *Rev. Mod. Phys.* **2005**, *77*, 371-423.
- ¹⁶ Strbac, S.; Petrovic, S.; Vasilic, R.; Kovac, J.; Zalar, A.; Rakocevic, Z., Carbon monoxide oxidation on Au(111) surface decorated by spontaneously deposited Pt. *Electrochimica Acta* **2007**, *53*(2), 998-1005.
- ¹⁷ Adzic, R. R.; Zhang, J.; Sasaki, K.; Vukmirovic, M. B.; Shao, M.; Wang, J. X.; Nilekar, A. U.; Mavrikakis, M.; Valerio, J. A.; Uribe, F., Platinum Monolayer Fuel Cell Electrocatalysts. *Topics in Catalysis* **2007**, *46*(3-4), 249-262.
- ¹⁸ Mukerjee, S.; Srinivasan, S.; Soriaga, M. P.; McBreen, J., Role of Structural and Electronic Properties of Pt and Pt Alloys on Electrocatalysis of Oxygen Reduction. *Journal of The Electrochemical Society* **1995**, *142*(5), 1409-1422.

-
- ¹⁹ Mansour, A. N.; Cook, J. W.; Sayers, D. E., Quantitative technique for the determination of the number of unoccupied d-electron states in a platinum catalyst using the L2,3 x-ray absorption edge spectra. *The Journal of Physical Chemistry* **1984**, *88*(11), 2330-2334.
- ²⁰ Mansour, A. N.; Cook Jr, J. W.; Sayers, D. E.; Emrich, R. J.; Katzer, J. R., Determination of support and reduction effects for PtAl₂O₃ and PtSiO₂ by X-ray absorption spectroscopy. *Journal of Catalysis* **1984**, *89*(2), 462-469.
- ²¹ Ohwaki, T.; Kiyotaka, A. *et al.*, preparing paper is scheduled to be submitted to the Journal of Physical chemistry C.
- ²² Weinhold, F.; Landis, C. R., NATURAL BOND ORBITALS AND EXTENSIONS OF LOCALIZED BONDING CONCEPTS. *Chemistry Education Research and Practice* **2001**, *2*(2), 91-104.
- ²³ Ohwaki, T.; Otani, M.; Ozaki, T., A method of orbital analysis for large-scale first-principles simulations. *The Journal of Chemical Physics* **2014**, *140*(24), -.
- ²⁴ Ozaki, T.; Kino, H., Efficient projector expansion for the *ab initio* LCAO method. *Physical Review B* **2005**, *72*(4), 045121.



Chapter 4

**In situ X-Ray Absorption Fine Structure Analysis of
PtCo, PtCu and PtNi Alloy Electrocatalyst-The
origin for Enhanced Activity of Oxygen Reduction
Reaction**

4.1 Introduction

In this chapter I have studied carbon supported randomly-mixed alloy Pt₅Co/C without heat treatments and Pt₃Co/C, Pt₂Co/C with heat treatment. Randomly-mixed heat treated alloy Pt₂Co/C showed approximately 10 times higher area specific activity than that of Pt/C. For comparison I have prepared Pt₃Cu and Pt₉Ni. I applied XAFS analysis to this system. XAFS is a way to identify the total structure in average compared to XRD which only gives me information about crystalline ordered intermetallic phase. By changing the heat treatment temperature, the inner structures such as bond distance and coordination numbers are continuously changed. I have made a correlation with the activity. I discussed the structure of the prepared PtCo, PtCu and PtNi electrocatalysts by structural parameters obtained by EXAFS curve fitting analysis combining with XRD, STEM, High-Angle-Annular-Dark-Field (HAADF) and the origin of enhanced area specific activities determined from rotating disk electrode (RDE) electrochemical testing method with Pt 5d vacancy determined from X-ray absorption near edge structure (XANES)

4.2 Materials and methods

4.2.1 Preparation of PtCo/C, PtCo/C-HT, PtCu/C, PtCu/C-HT and PtNi/C electrocatalyst

I have prepared two different Pt/Co ratio samples with different treatment temperatures as follows. 1 L of ultrapure water was poured into a beaker and stirred on a magnetic stirrer. Then 22.3 g of 2.4 wt% CoCl_2 aqueous solution was poured into the beaker followed by the addition of 0.6 g of 40.6 wt% H_2PtCl_2 aqueous solution. After stirring 5 minutes for mixing, 100 mL of reducing agent (mixture of 0.4 g of NaBH_4 and 1.2 g of $\text{C}_6\text{H}_5\text{Na}_3\text{O}_7 \cdot 2\text{H}_2\text{O}$ dissolved in ultrapure water) was slowly poured into the beaker. After 30 minutes stirring both Pt and Co ions were reduced to the PtCo alloy particles. 0.2 g of Ketjenblack having been stirred in the 100 mL of ultrapure water in advance was slowly poured into the beaker. After 72 hours of continuous stirring at room temperature, the resulting PtCo/C was filtered and dried for more than 4 hours at 60 °C. Finally, PtCo/C on the filter was scratched, yielding carbon-supported electrocatalyst powder. The sample was then heated in Argon atmosphere at appropriate temperatures, i.e., 600, 700 and 800 °C. The sample thus obtained was denoted as PtCo/C-HT-600, for example, in which the last numeral indicated the heat treatment temperature. The process was changed for the preparation of PtCo/C with the higher Co concentration. The amount of CoCl_2 aqueous solution was doubled. The sample thus obtained was denoted as PtCo/C-HT-600h, in which the last alphabet means the higher Co concentration.

For the preparation of PtCu/C electrocatalyst the source material CoCl_2 was changed to CuCl_2 . The poured amount of the solution and their wt% and the process times were all the same as the preparation process of PtCo/C. However the heat treatment atmosphere was changed from in Argon to in Hydrogen at 600 °C.

The preparation process of PtNi/C electrocatalyst was slightly different from those of PtCo/C and PtCu/C electrocatalyst. 1 L of ultrapure water was poured into a beaker and stirred on a magnetic stirrer. Then 22.3 g of 2.4 wt% NiCl_2 aqueous solution was

poured in the beaker. 100 mL of reducing agent used for the preparation of PtCo and PtCu was poured into the beaker and stirred for 30 minutes for the prior reduction of Ni ions. After that 0.6 g of 15.3 wt% H_2PtCl_2 aqueous solution was poured into the beaker and stirred for 30 minutes. Similar to PtCo/C, the 0.2 g of Ketjenblack having been stirred in the 100 mL of ultrapure water in advance was slowly poured into the beaker. After 72 hours of continuous stirring at room temperature, the resulting PtNi/C was filtered and dried for more than 4 hours at 60 °C. Finally, PtNi/C on the filter was scratched, yielding carbon-supported electrocatalyst powder.

On the other hand commercially available Pt/C was used for a reference sample (nominal Pt loading 50 wt%, Ketjenblack carbon support; TEC10E50E, Tanaka Kikinzoku Kogyo K.K.) as described in chapter 3. Table 1 summarizes the samples' preparation conditions, their average diameters and atomic percentages of Pt, Co, Cu and Ni after *in situ* XAFS experiment. Although PtCo/C was the source material for the PtCo/C-HT-600, -700, -800, atomic ratio of PtCo/C was different from that of PtCo/C-HTs. The reason is the dissolution of Co atoms from PtCo/C during the preparation process of electrocatalyst ink, because electrocatalyst ink to form electrocatalyst layer is acid solution ascribing the contained Nafion ionomer. In addition Co atoms were not well alloyed with other atoms without heat treatments. On the other hand Pt/Cu ratio of PtCu/C and PtCu/C-HT was the same maybe because Cu atoms were rather well alloyed with other atoms in a particle. Detailed explanation is described in section 4.3.3.1 combined with XANES spectra of added metals. The temperatures of heat treatment were 600, 700 and 800 °C. Although the heating time for 600, 700 °C-treated sample was 2 hours, the heating time for the 800 °C-treated sample was reduced to 1 hour to avoid coalescence. For the PtNi/C the heating process was not conducted to maintain its specific hollow structure described in section 4.3.2.

Table 4.1 Heat treatment conditions, average diameters, and atomic percentages of Pt/C, PtCo/C, PtCo/C-HTs, PtCu/C, PtCu/C-HT and PtNi/C

	Pt _x M atomic ratio	Temperature / °C	heating time / hour	Average diameter / nm	at %			
					Pt	Co	Cu	Ni
Pt/C	Pt	-	-	2.2	100	-	-	-
PtCo/C	Pt ₃ Co	-	-	2.4	82	18	-	-
PtCo/C-HT-600	Pt ₃ Co	600	2.0	4.5	75	25	-	-
PtCo/C-HT-700	Pt ₃ Co	700	2.0	4.4	74	26	-	-
PtCo/C-HT-800	Pt ₃ Co	800	1.0	4.2	74	26	-	-
PtCo/C-HT-600h	Pt ₂ Co	600	2.0	3.9	70	30	-	-
PtCu/C	Pt ₃ Cu	-	-	2.2	73	-	27	-
PtCu/C-HT-600	Pt ₃ Cu	600	2	4.0	73	-	27	-
PtNi/C	Pt ₉ Ni	-	-	6.8	88	-	-	12

4.2.2 Characterization of Pt/C, PtCo/C, PtCo/C-HTs, PtCu/C, PtCu/C-HT and PtNi/C electrocatalysts

The prepared electrocatalysts were characterized by Transmission electron microscopy (TEM), STEM-EDX (Energy dispersion X-ray spectroscopy), High-Angle-Annular-Dark-Field (HAADF)-STEM, inductively coupled plasma mass spectrometer (ICP-MS), X-ray diffraction (XRD), and electrochemical methods. The particle diameter distribution and the average diameter of electrocatalysts were obtained using TEM (HF-2000 field emission TEM Hitachi High-Technologies Corporation). Sectional elemental distribution of PtCo/C-HTs and PtNi/C electrocatalyst particles was analyzed by STEM-EDX, STEM-HAADF (HD-2700 Hitachi High-Technologies Corporation). The mass ratio of Pt, Co, Cu and Ni was measured by an ICP-MS, (SPS-3520, SII NanoTechnology Inc.). Electrochemical analysis was conducted with a rotating disk electrode (RDE) measurement apparatus (HZ-5000, Hokuto Denko

Corporation). For the electrochemical experiments, Reversible hydrogen electrode (RHE) and a Pt mesh were used as the reference electrode and the counter electrode, respectively. Cyclic voltammograms (CVs) was obtained in deaerated 0.1-M HClO₄ solutions at the sweep rate 50 mVs⁻¹. Polarization curves were recorded in an Oxygen-saturated 0.1-M HClO₄ solution at the sweep rate 10 mVs⁻¹.

4.2.3 XAFS measurements

The XAFS experiments were conducted at the X-ray bending magnet beam line BL16B2 of SPring-8 in Japan. The ring was operated at 8 GeV with its ring current at 100 mA in a top-up mode. The X-ray beam was monochromatized using a Si (111) double crystal monochromator. The incident and transmitted X-ray intensities were monitored using two ionization chambers filled with Nitrogen and mixture of Nitrogen 85 % and Argon 15 % for incident X-ray and transmitted X-ray measurements, respectively.

I set the samples in the *in-situ* measurement spectroelectrochemical cells described in chapter 2. Prior to the *in situ* measurements, air was removed by passing pure Nitrogen (99.99995%) through the electrolyte solution in the XAFS cell for 30 minutes. During experiments, Nitrogen gas was continuously flowed over the electrolyte solution to prevent air contamination. The electrode potential was swept cathodically from the rest potential (*ca.* 1.0 V vs. RHE) to 0.05 V vs. RHE at a slow scan rate (1 mVs⁻¹) to avoid large current and potential inhomogeneity in the catalyst layer. Then an oxidation-reduction cycle (ORC) treatment (0.05–1.2 V vs. RHE) was conducted three times to remove contamination from the surface of the electrocatalyst. After the ORC treatments, XAFS measurements were performed at 0.4 V vs. RHE after holding the electrode potential at 0.4 V vs. RHE for 20 minutes. As reference samples for curve-fitting analyses, Pt, Co, Cu foils and PtCo, PtCu, PtNi random alloy foils containing 90 atomic percent (at%) Pt, were also measured to determine the fitting parameters of EXAFS (amplitude reduction factor S_j and energy difference ΔE_{0j}) and

confirm the validity of theoretical phase shift and amplitude parameters.

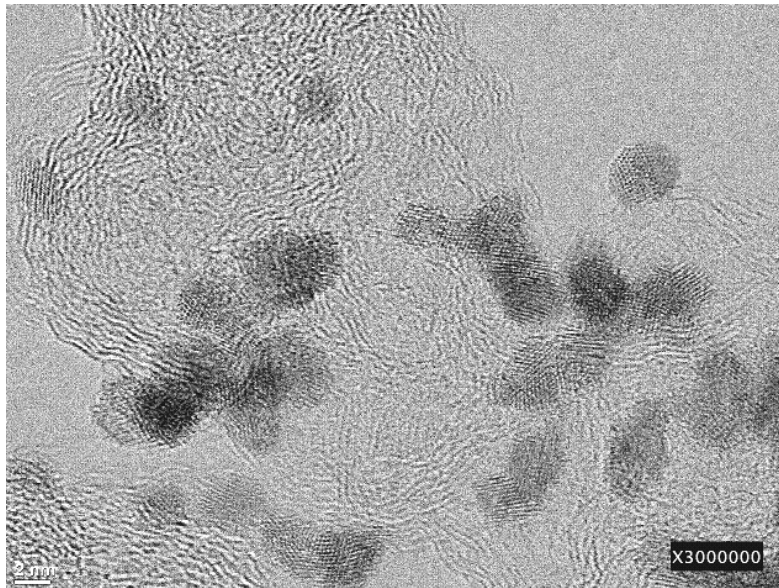
4.3. Results

4.3.1 Characterization of PtCo/C, PtCo/C-HT, PtCu/C, PtCu/C-HT and PtNi/C electrocatalysts

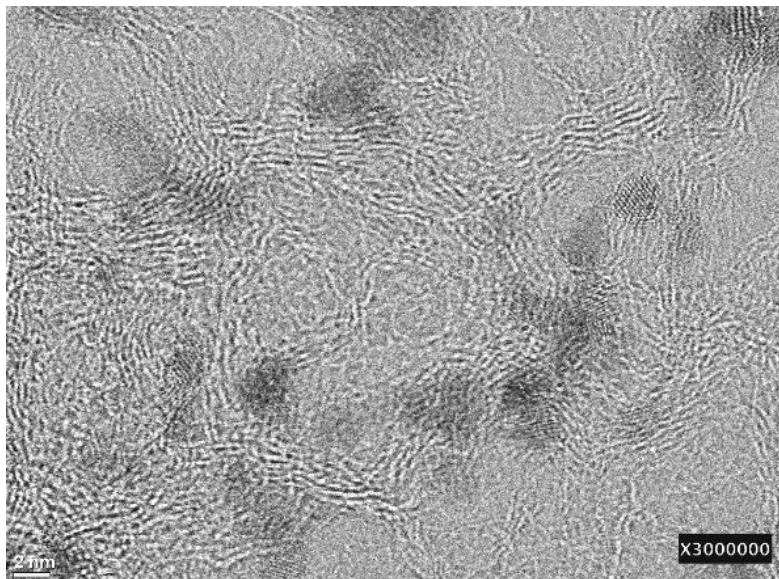
Figure 4.1 (a)-(h) shows the TEM images of PtCo/C, PtCu/C, PtNi/C without heat treatment process, PtCo/C-HT-600, PtCo/C-HT-700, PtCo/C-HT-800, PtCo/C-HT-600h and PtCu/C-HT-600 after heat treatment process. Figure 4.2 shows the particle diameter distribution of PtCo/C, PtCu/C, PtNi/C without heat treatment process, PtCo/C-HT-600, PtCo/C-HT-700, PtCo/C-HT-800, PtCo/C-HT-600h and PtCu/C-HT-600 after heat treatment process. As shown in Fig. 4.1 (a), (b) and average diameter of Table 4.1 in section 4.2.1, the diameter of PtCo and PtCu alloy particles before heat treatment was small and diameter distribution was narrow, however after the heat treatment the average diameter and diameter distribution of particles became larger as shown in Table 4.1 and Fig. 4.2 because of the coalescence. On the other hand as shown in Fig. 4.1 (c) the diameter distribution of PtNi/C was narrower however the diameter was larger than that of PtCo/C and PtCu/C. Additionally, HAADF-STEM observation and STEM-EDX line profile measurement were conducted on PtCo/C-HTs and PtNi/C samples after RDE testing experiments. As far as I observed, no pure Pt or Co or Cu or Ni particle were observed by EDX. HAADF image and STEM-EDX line profile of PtCo/C-HT-600 after RDE testing are shown in Figure 4.3 to show Pt atoms and Co atoms were well mixed in a particle though the surface Pt concentration seemed to be larger than Co. Figure 4.4 shows the HAADF image and STEM-EDX line profile of one PtNi/C particle after RDE testing. As shown in the HAADF image the core of the particle was dark hence the Pt was considered that mainly located at the outer shell part of the particles. The core part was considered to be Ni or hollow. According to the following STEM-EDX line profile the Pt intensity at the center of the particle was weak as expected from the HAADF image. In addition the intensity of Ni was quiet weak. Hence the shape of the PtNi particle was considered to be hollow structure. The thickness of the shell was approximately 2.5 nm. The structure of

prepared PtNi/C was similar to the Pt hollow structure reported by Wang *et al.*¹

Figure 4.5 shows XRD diffraction peaks of Pt/C, PtCo/C, PtCo/C-HT-600, PtCo/C-HT-700 and PtCo/C-HT-800. No peak indicating the existence of Co particle was observed at 43.6 degree. After heat treatment, XRD peak became sharper by the enhancement of crystallization and shows the typical Pt FCC structure. From the diffraction peak depicted, it was clarified that no Co metal particles were synthesized on carbon support in the preparation process, and crystallization of PtCo alloy was advanced by the heat treatment. The prominent peaks of PtCo/C without heat treatment were shifted to higher 2θ angles compared with Pt/C, and that of PtCo/C-HTs was shifted to much higher angle compared with the peak of PtCo/C, indicating the contraction of lattice constant by alloying and heat treatment. In addition, compared with Pt₃Co intermetallic theoretical diffraction pattern, the peaks around 33 and 23 degree were slightly observed in the PtCo/C-HT samples.

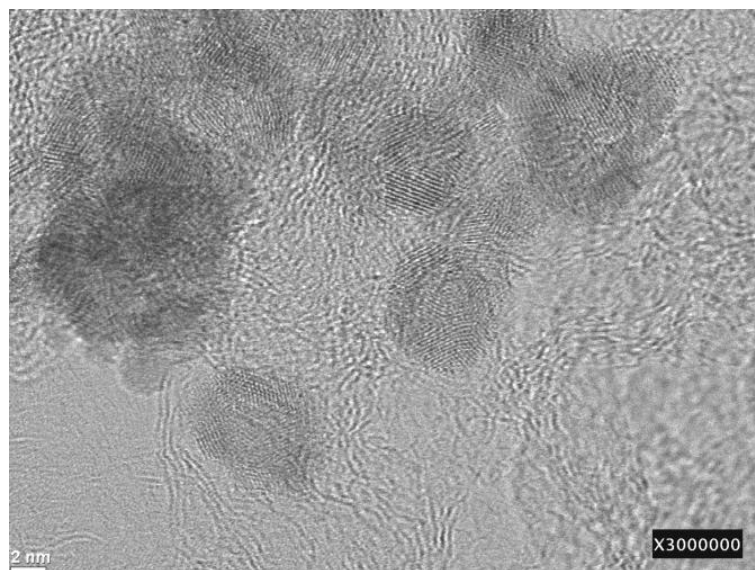


(a) PtCo/C

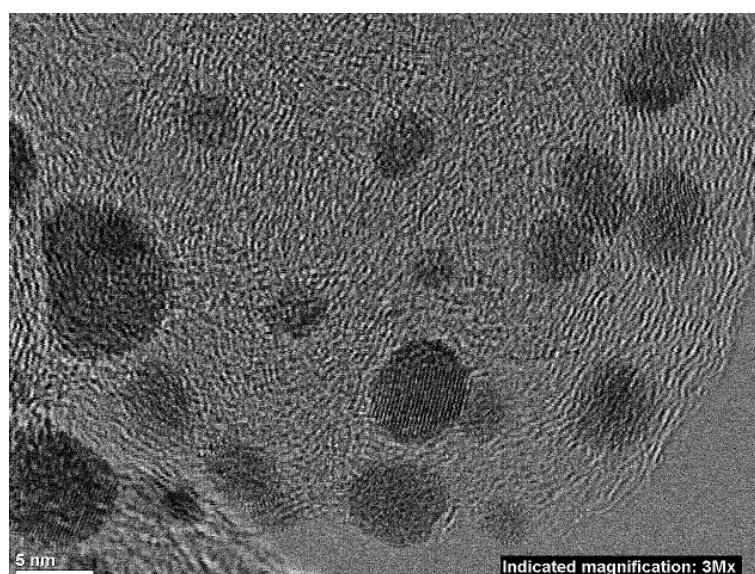


(b) PtCu/C

Figure 4.1 TEM images of (a) PtCo/C, (b) PtCu/C.

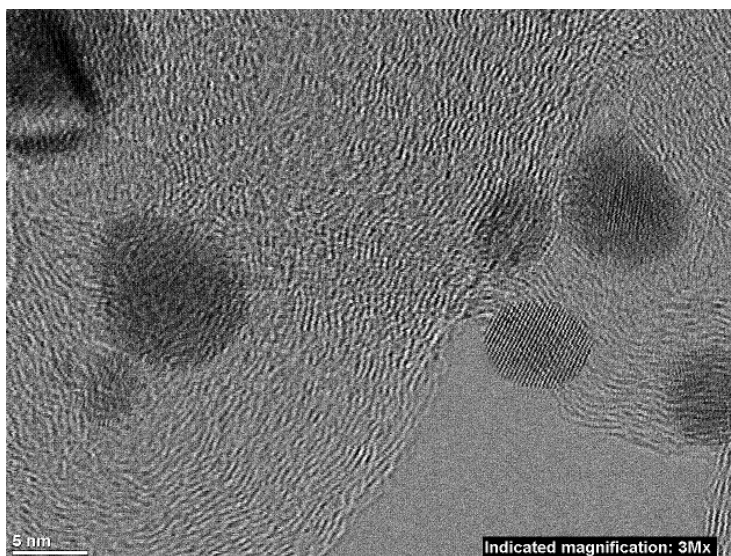


(c) PtNi/C

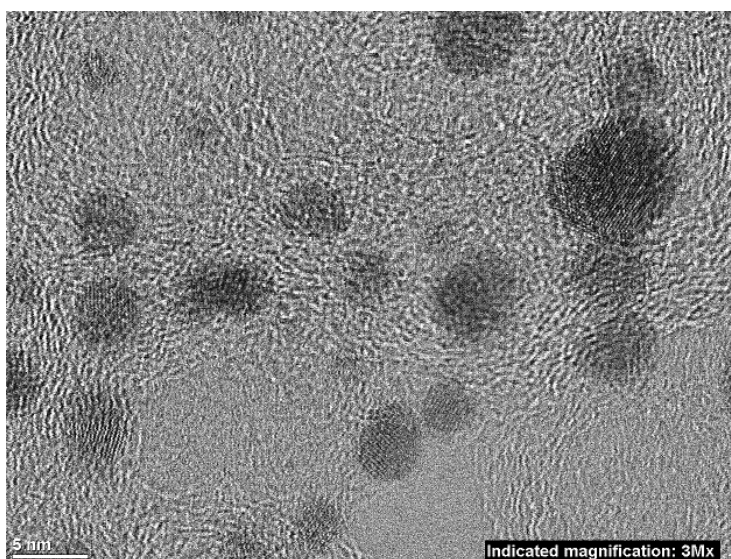


(d) PtCo/C-HT-600

Figure 4.1 TEM images of (c) PtNi/C without heat treatment, (d) PtCo/C-HT-600.

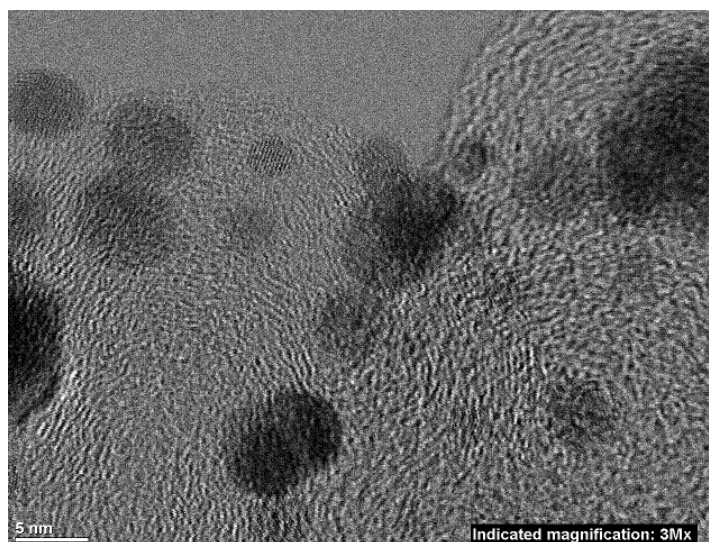


(e) PtCo/C-HT-700

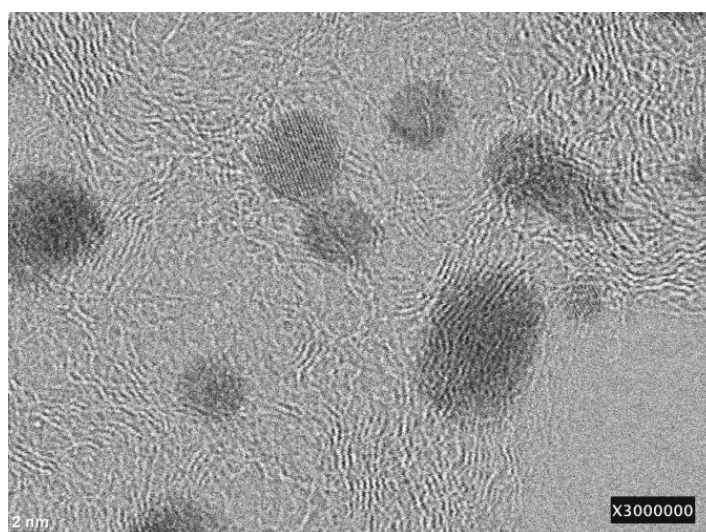


(f) PtCo/C-HT-800

Figure 4.1 TEM images of (e) PtCo/C-HT-700, (f) PtCo/C-HT-800.

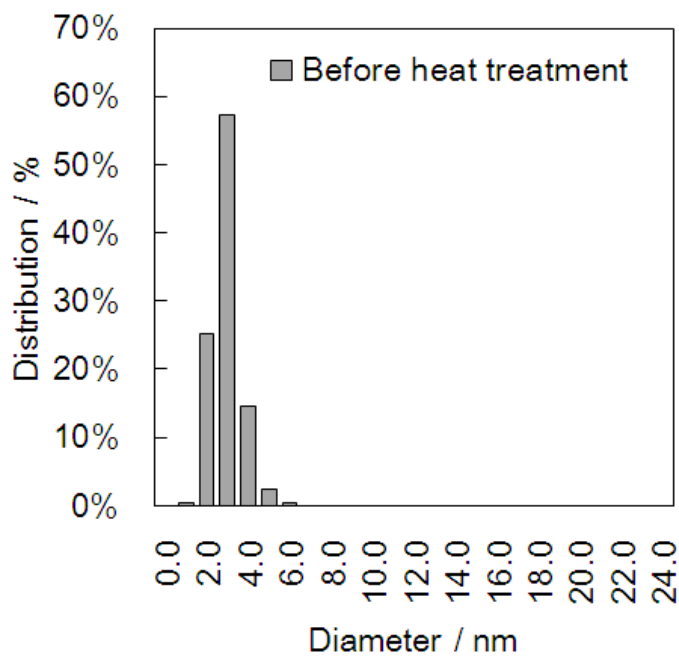


(g) PtCo/C-HT-600h

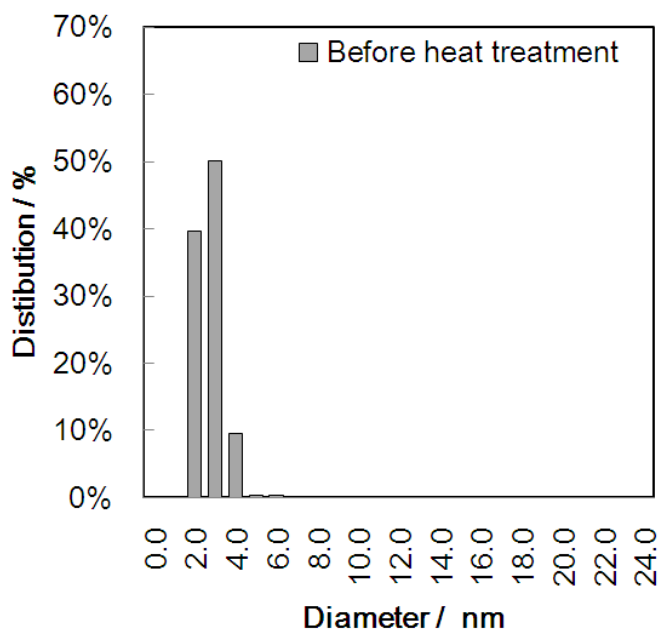


(h) PtCu/C-HT-600

Figure 4.1 TEM images of (g) PtCo/C-HT-600h and (h) PtCu/C-HT-600 with heat treatment process.

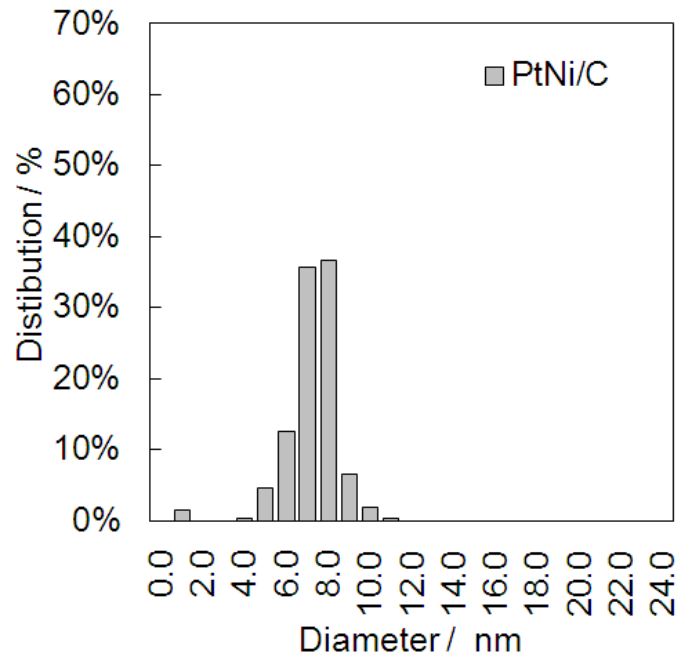


(a) PtCo/C

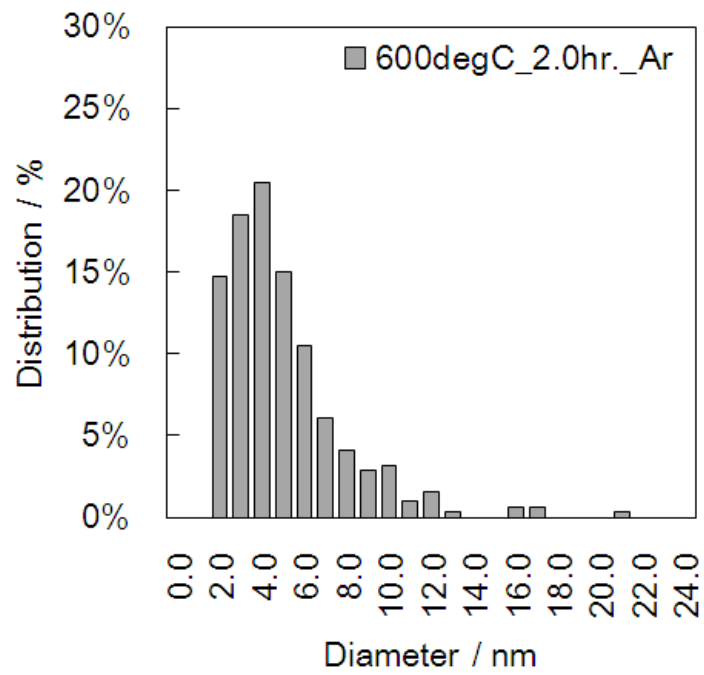


(b) PtCu/C

Figure 4.2 Diameter distributions of (a) PtCo/C, (b) PtCu/C.

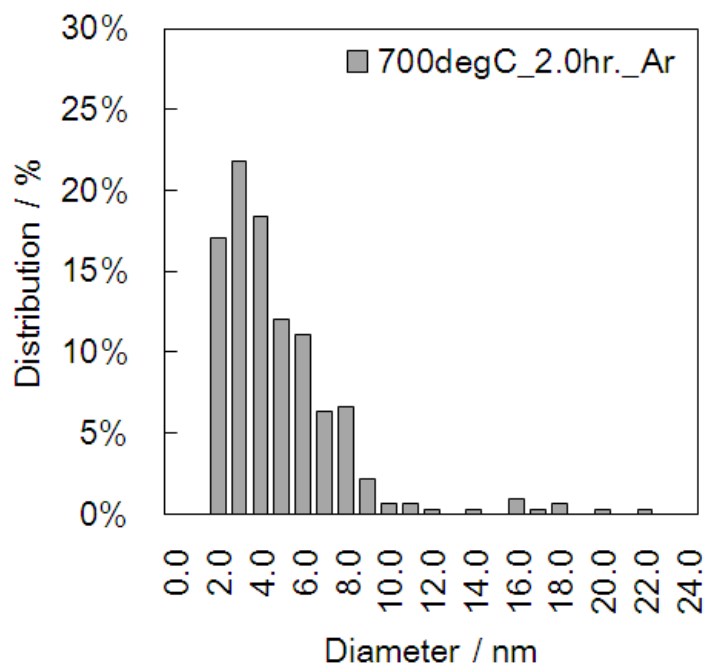


(c) PtNi/C

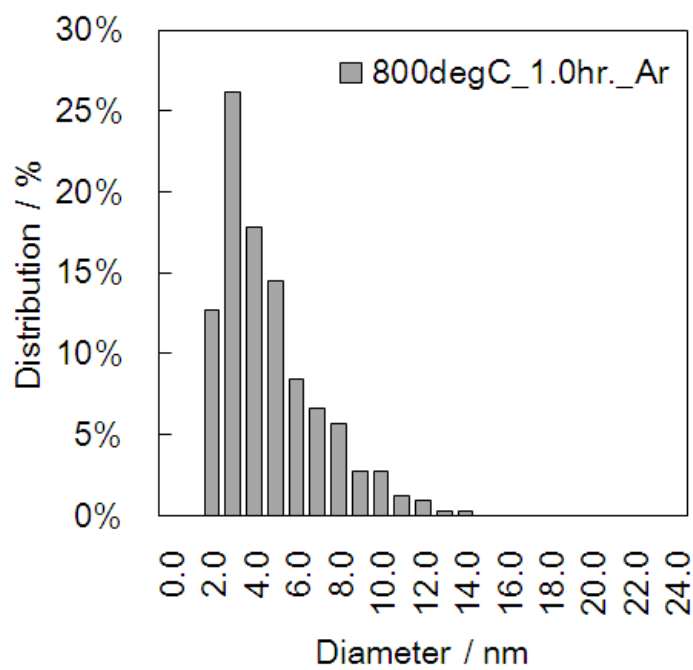


(d) PtCo/C-HT-600

Figure 4.2 Diameter distributions of (c) PtNi/C without heat treatment, (d) PtCo/C-HT-600.

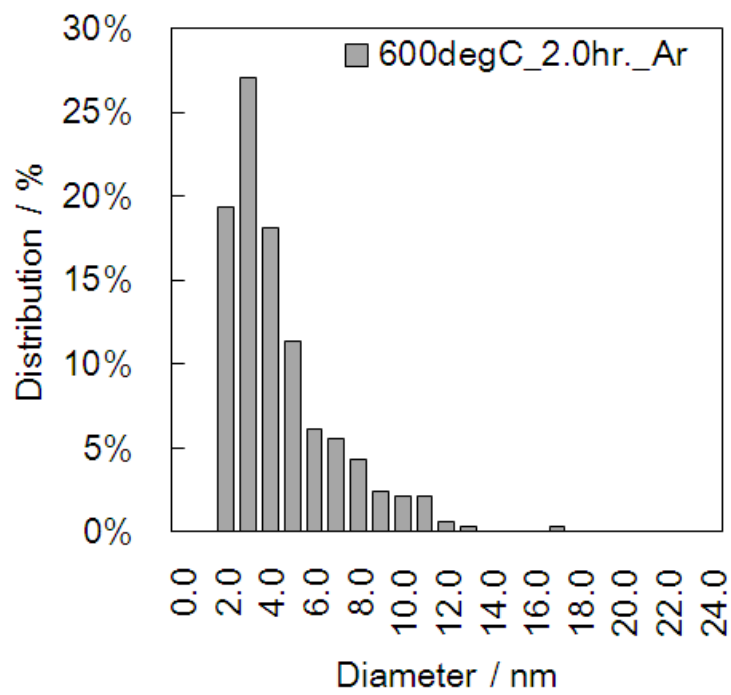


(e) PtCo/C-HT-700

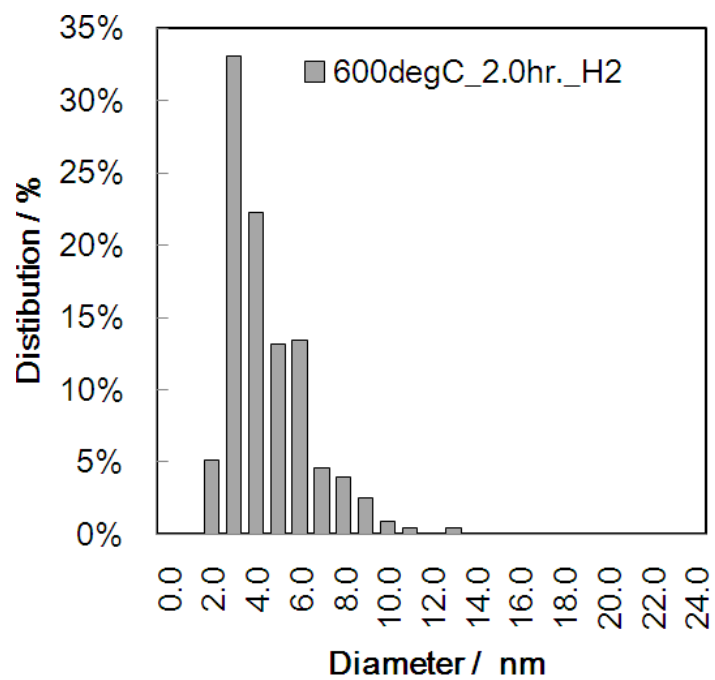


(f) PtCo/C-HT-800

Figure 4.2 Diameter distributions of (e) PtCo/C-HT-700, (f) PtCo/C-HT-800.

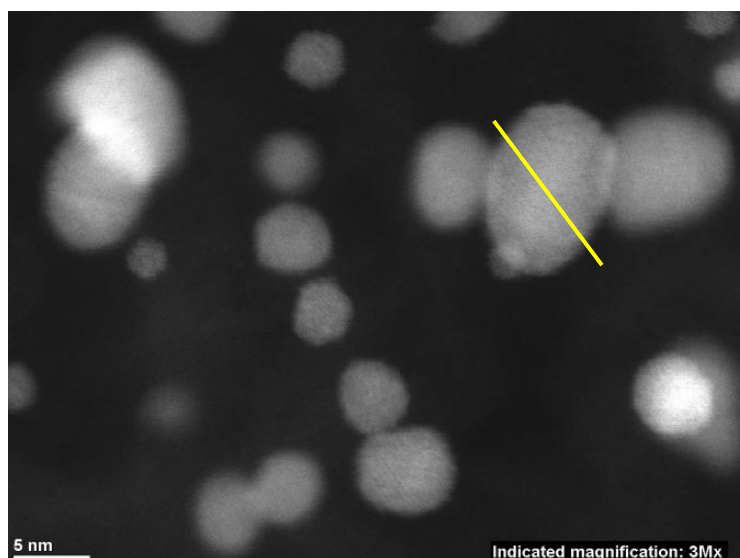


(g) PtCo/C-HT-600h

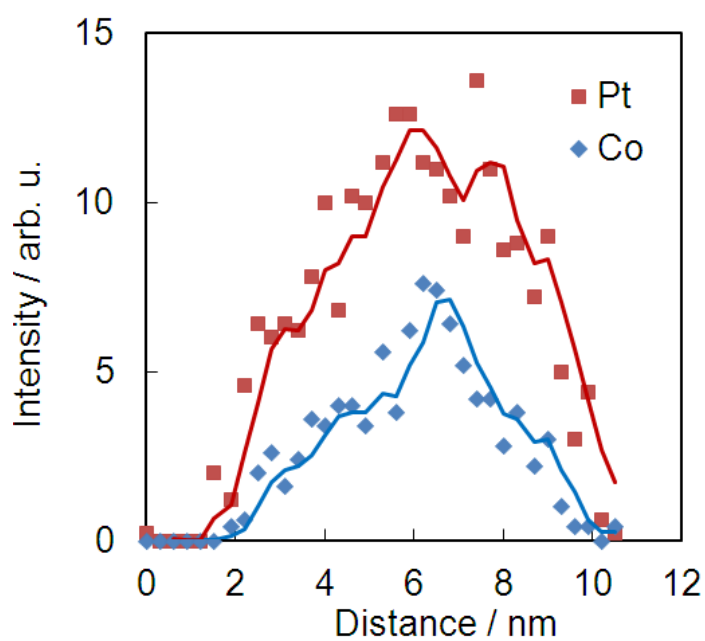


(h) PtCu/C-HT-600

Figure 4.2 Diameter distributions of (g) PtCo/C-HT-600h and (h) PtCu/C-HT-600 with heat treatment process.

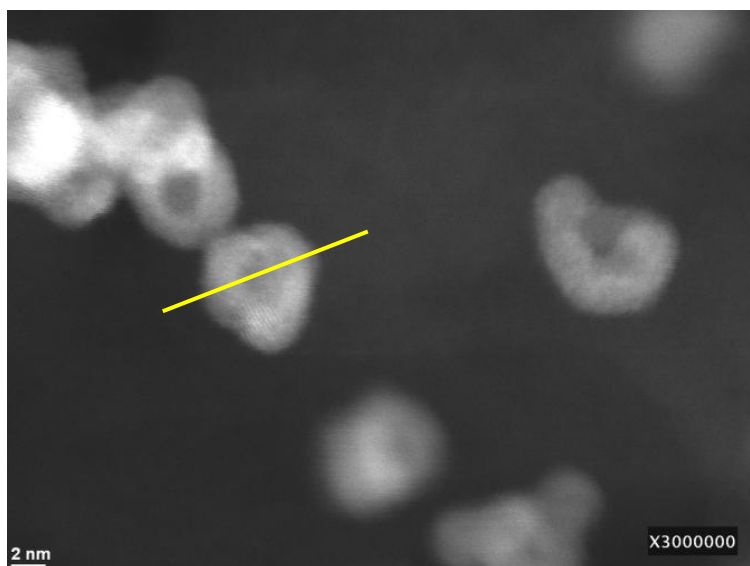


(a) HAADF-STEM image

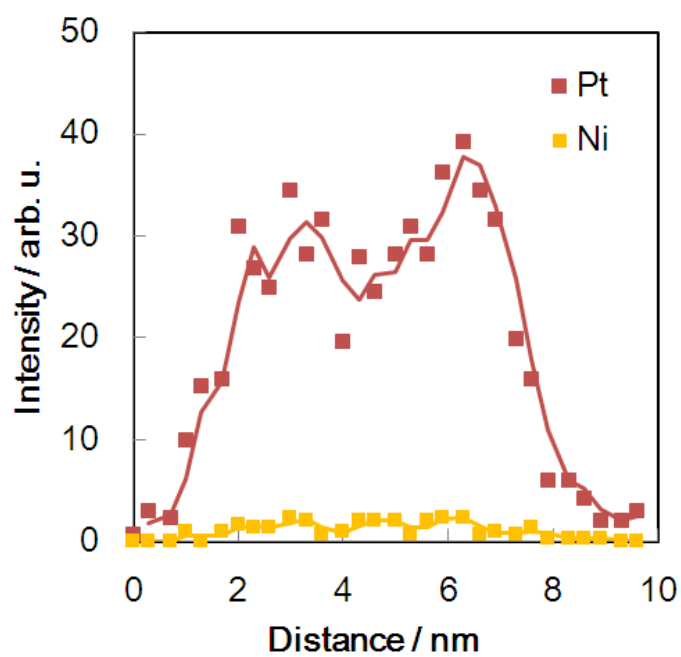


(b) STEM-EDX profile of yellow line in (a)

Figure 4.3 (a) HAADF-STEM image of heat treated PtCo/C-HT-600 after RDE experiments and (b) Pt and Co STEM-EDX intensity profile of yellow line shown in the HAADF image (a).



(a) HAADF-STEM image



(b) STEM-EDX profile of yellow line in (a)

Figure 4.4 (a) HAADF-STEM image of PtNi/C after RDE experiments and (b) Pt and Ni STEM-EDX intensity profile of yellow line shown in HAADF image (a).

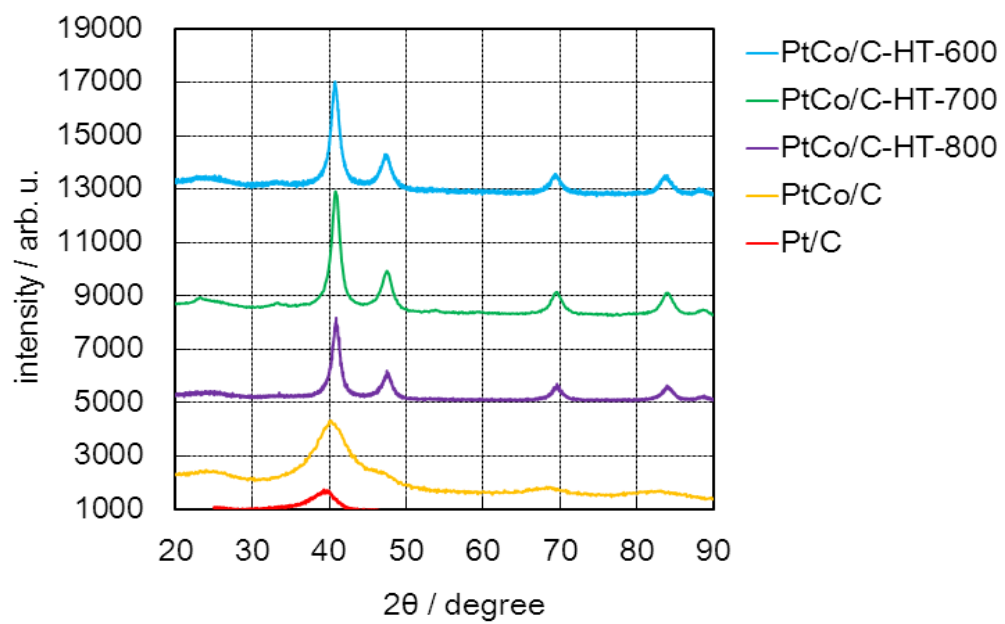


Figure 4.5 X-ray diffraction pattern of Pt/C, PtCo/C, heat treated PtCo/C-HT-600, PtCo/C-HT-700, and PtCo/C-HT-800.

4.3.2 ORR activities of Pt/C, PtCo/C, PtCo/C-HTs, PtCu/C, PtCu/C-HT and PtNi/C electrocatalysts

To determine the ORR activity, the Pt/C, PtCo/C, PtCo/C-HTs, PtCu/C, PtCu/C-HT and PtNi/C were dispersed in a solvent consisting of ultrapure water and Nafion ionomer by ultrasonication for 30 minutes. The suspensions were deposited on the precleaned glassy carbon substrate of RDE to satisfy the Pt loading of $8.3 \mu\text{g-Pt}/\text{cm}^2$ for PtCu/C-HT, $10 \mu\text{g-Pt}/\text{cm}^2$ for PtCo/C, PtCo/C-HTs and $17 \mu\text{g-Pt}/\text{cm}^2$ for Pt/C, PtCu/C and PtNi/C. Subsequently it was dried at 60°C .

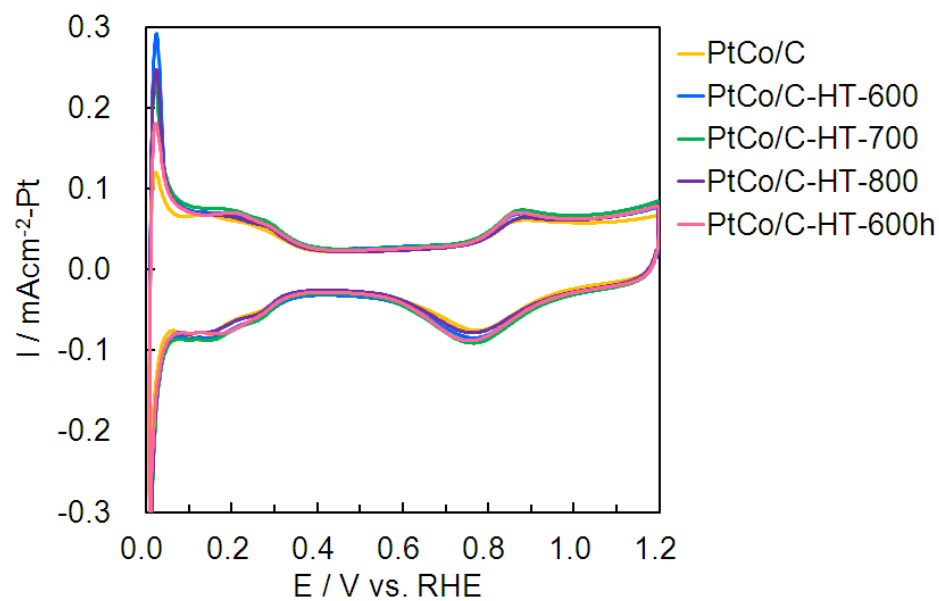
CVs of those prepared samples are shown in Figure 4.6. Observed current of CVs were normalized by the electrochemical effective Pt surface areas (S_{Pt}). S_{Pt} was determined by dividing the hydrogen adsorption charge by the hydrogen desorption and adsorption density $210 \mu\text{Ccm}^{-2}$, which is the density of Pt polycrystalline.² CVs of PtCo/C and PtCo/C-HTs were almost similar as shown in Fig. 4.6 (a). However as shown in Fig. 4.6 (b) the normalized current of the CVs of PtCu/C-HT and PtNi/C were a little larger than other samples. This is because S_{Pt} of those samples were smaller than other samples. The reason of smaller S_{Pt} for PtNi/C was considered to be its larger average diameter compared with other samples. However the reason of larger normalized current of PtCu/C-HT remains still unclear. As a whole the CVs showed typical response of Pt alloy electrocatalyst. ECA (Electrochemical surface area) of each sample was determined from the S_{Pt} and Pt loading on the RDE disc. Table 4.2 shows ECAs and ORR activities of Pt/C, PtCo/C, PtCo/C-HTs, PtCu/C, PtCu/C-HT and PtNi/C.

Polarization curve for ORR activity of electrocatalysts were obtained in a 0.1-M HClO_4 solution purged and saturated by 99.99% Oxygen at different rotation speeds (400, 800, 1200, 1600 and 2000 rpm). The potential observed by the measurement system was given in the IR-drop correction taking into account by the resistance between WE and RE. The specific activity at a corrected electrode potential of 0.9 V vs. RHE was acquired from the intercept of Koutecky-Levich plot, *i.e.*, the inverse

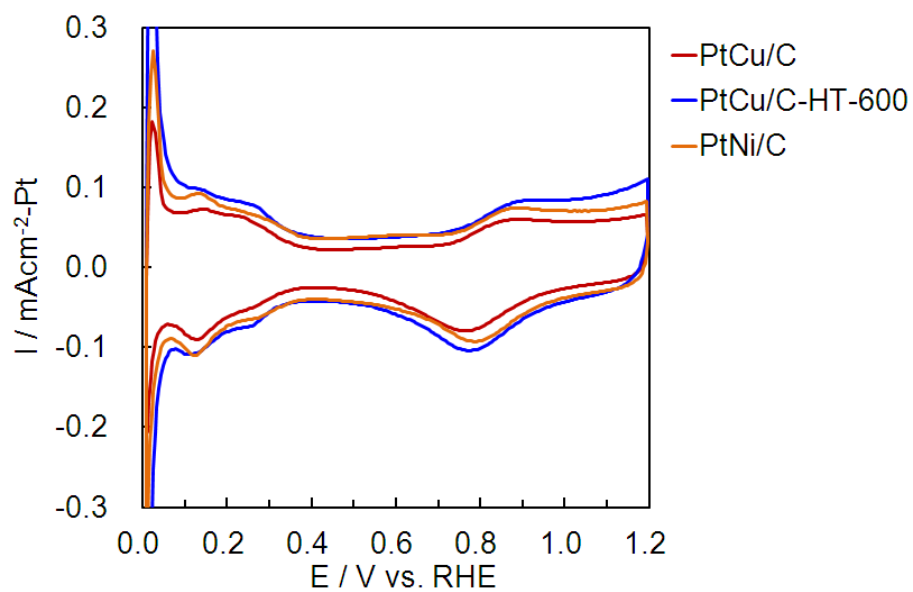
current density ($1/j$) plotted as a function of the inverse of the square root of the rotation rate ($\omega^{1/2}$) using the polarization curve among the prepared electrocatalysts. PtCo/C-HT-600h showed the highest area specific activity. Figure 4.7 shows the linear sweep voltammogram (LSV) of Pt/C base electrocatalyst, PtCo/C, PtCo/C-HT-600h. The activity enhanced in this order and PtCo/C-HT showed highest area specific activity. Area specific activity of PtCo/C-HT-600h was 10 times higher than that of Pt/C. Although the specific activity of PtCo/C was enhanced drastically by the heat treatment process, the area specific activity of PtCu/C-HT was not improved in spite of heat treatment. The area specific activities of no heat treated samples such as PtCo/C, PtCu/C and PtNi/C were almost similar level and they were approximately 4 to 5 times higher than that of Pt/C.

Table 4.2 ECA and ORR area-specific and mass-specific activities of Pt/C, PtCo/C, PtCo/C-HT-600, PtCo/C-HT-700, PtCo/C-HT-800, PtCo/C-HT-600h and PtCu/C, PtCu/C-HT-600 and PtNi/C electrocatalysts. The values in parenthesis indicated the IR uncorrected activity.

	ECA / m^2g^{-1}	Area specific activity / μAcm^{-2}	Mass specific activity / Ag^{-1}
Pt/C	84.2	526(298)	428
PtCo/C	43.7	2364 (1043)	1034
PtCo/C-HT-600	45.2	4311 (1635)	1947
PtCo/C-HT-700	42.3	4628 (1809)	1897
PtCo/C-HT-800	42.6	3643 (1466)	1546
PtCo/C-HT-600h	48.7	5238 (1828)	2551
PtCu/C	58.7	1990 (793)	1168
PtCu/C-HT-600	27.9	2176 (1490)	608
PtNi/C	31.1	2748 (1149)	856



(a) PtCo/C and PtCo/C-HTs,



(b) PtCu/C, PtCu/C-HT, and PtNi/C

Figure 4.6 Cyclic voltammogram of electrocatalysts, (a) PtCo/C, PtCo/C-HTs, and (b) PtCu/C, PtCu/C-HT, and PtNi/C.

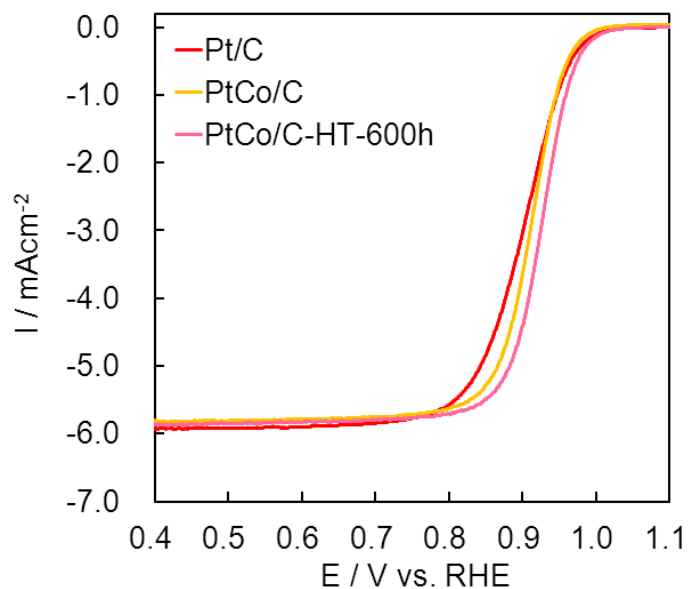


Figure 4.7 Linear sweep voltammogram at 1600 rpm of Pt/C, PtCo/C without heat treatment and heat treated PtCo/C-HT-600h which showed the highest ORR activity among the tested electrocatalysts.

4.3.3 XAFS analysis

4.3.3.1 XANES analysis of PtCo/C, PtCo/C-HTs, PtCu/C, PtCu/C-HT and PtNi/C electrocatalyst

Figure 4.8 shows Co K-edge XANES spectra of PtCo/C and PtCo/C-HTs at 0.4 V vs. RHE together with standard spectra of Co foil, CoO powder and PtCo alloy foil. Co K-edge of PtCo/C has a rather large absorption edge peak. In addition the peak energy of PtCo/C is close to CoO reference sample. Hence the most of the Co atoms in PtCo/C were not metallic but somewhat oxidized. This oxidation and insufficient metallic system was considered to be one reason of easy dissolution of Co atoms from PtCo/C electrocatalyst. On the other hand Co XANES spectra of PtCo/C-HTs were different from that without heat treatment. The edge peak height decreased and the edge position shifted to lower energy with heat treatment temperature. The edge and peak shoulders appeared at 7722 and 7728 eV resembling the PtCo foil spectrum. The shapes of XANES for PtCo/C-HTs are different from that of Co foil which has two peaks at 7723 and 7732 eV. The heat treatment has effectively reduced the Co species to form PtCo alloyed particle.

Figure 4.9 shows Cu K-edge XANES spectra of PtCu/C and PtCu/C-HT at 0.4 V vs. RHE together with standard spectra of PtCu alloy foil and Cu foil. XANES spectrum of PtCu/C was not so different from Cu foil or PtCu foil relative to the difference of spectra between PtCo/C and Co foil. The height of edge peak of PtCu/C was not so high compared with that of CuO or Cu₂O reported by Gaur *et al.*³ Cu atoms of PtCu/C without heat treatment process were less oxidized than Co atoms of PtCo/C. In addition Cu atoms were rather well alloyed in spite of no heat treatment compared with Co atoms of PtCo/C. The absence of no strongly oxidized state of Cu was the reason of no loss of Cu in PtCu/C comparing with PtCu/C-HT.

Figure 4.10 shows Ni K-edge XANES spectra of PtNi/C at 0.4 V vs. RHE together with standard spectra of PtNi alloy foil, Ni foil and NiO reference powder. The edge peak height and energy of PtNi/C was close to the NiO particle. Hence the Ni atoms

of PtNi/C were thought to be oxidized and the electronic states of Ni atoms in PtNi/C were thought to be different from that of PtNi alloy foil.

Figure 4.11 and Figure 4.12 show the Pt L_{III} and L_{II} XANES spectra of Pt foil and Pt alloys respectively. The edge peak called as white line was observed as shown in Fig. 4.11 which could be assigned to the transition of Pt 2p to 5d empty state. In order to elucidate density of Pt 5d vacancies for Pt/C, PtCo/C PtCo/C-HTs, PtCu/C, PtCu/C-HT and PtNi/C shown in Fig. 4.11, 4.12, I analyzed the Pt L_{II} and L_{III}-edge XANES spectra according to the method proposed by Mansour *et.al.*⁴ Table 4.3 shows Pt 5d vacancies of prepared electrocatalyst and reference foils. The correlation between Pt 5d vacancies and area specific activities are shown in Figure 4.13. The errors of the Pt 5d vacancies were calculated from the errors of the determined area sizes used in the calculation of vacancies. In this study the errors of the area sizes were assumed to have been 5 %. The small changes in Pt 5d vacancies were observed in the medium value of the Pt alloy foils and Pt alloy nanoparticles compared with that of Pt foil. However the increments of Pt 5d vacancies of the samples were so small that the differences between samples could be within the limit of errors. Hence the correlation between Pt 5d vacancies and activities were not clarified in this study.

Table 4.3 Pt 5d vacancies of Pt foil, Pt/Co, PtCu, PtNi random alloy foils, Pt/C, PtCo/C, PtCo/C-HTs, PtCu/C, PtCu/C-HT and PtNi/C at 0.4 V vs. RHE

Sample	Pt 5d vacancy
Pt foil	0.300
PtCo foil	0.302 ± 0.031
PtCu foil	0.306 ± 0.029
PtNi foil	0.303 ± 0.030
Pt/C	0.309 ± 0.031
PtCo/C	0.312 ± 0.031
PtCo/C-HT-600	0.313 ± 0.031
PtCo/C-HT-700	0.311 ± 0.031
PtCo/C-HT-800	0.313 ± 0.031
PtCo/C-HT-600h	0.313 ± 0.031
PtCu/C	0.305 ± 0.030
PtCu/C-HT	0.305 ± 0.030
PtNi/C	0.303 ± 0.030

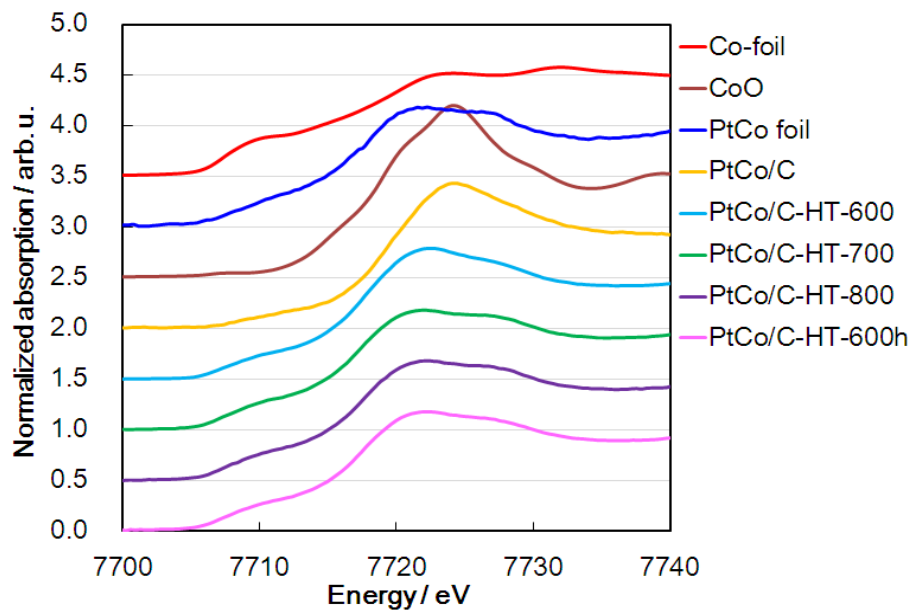


Figure 4.8 Co K-edge XANES spectra of Co foil, CoO reference powder, PtCo alloy foil, PtCo/C, PtCo/C-HT-600, PtCo/C-HT-700, PtCo/C-HT-800 and PtCo/C-HT-600h at 0.4V vs. RHE.

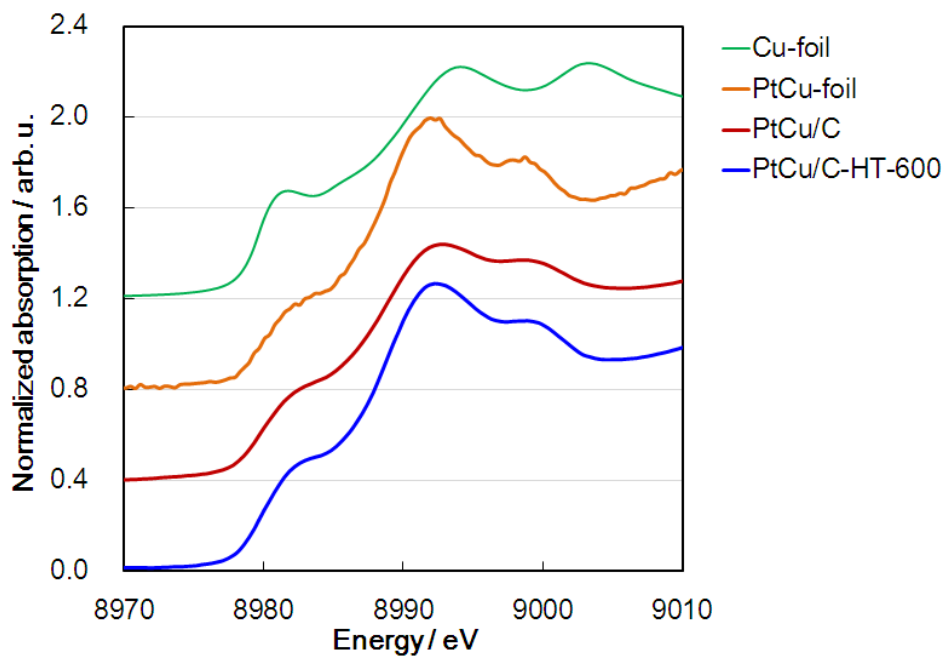


Figure 4.9 Cu K-edge XANES spectra of Cu foil, PtCu alloy foil, PtCu/C and PtCu/C-HT-600 at 0.4V vs. RHE.

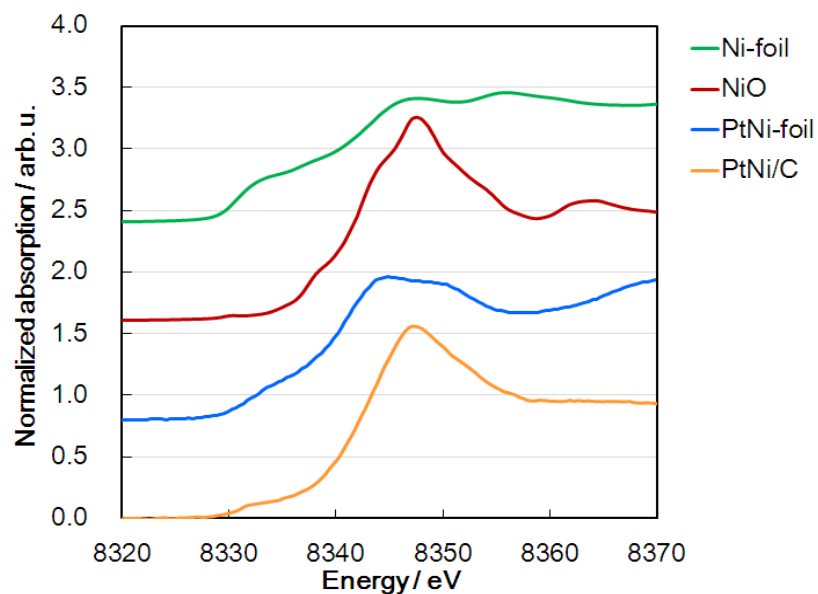


Figure 4.10 Ni K-edge XANES spectra of Ni foil, NiO reference powder, PtNi alloy foil and PtNi/C at 0.4V vs. RHE.

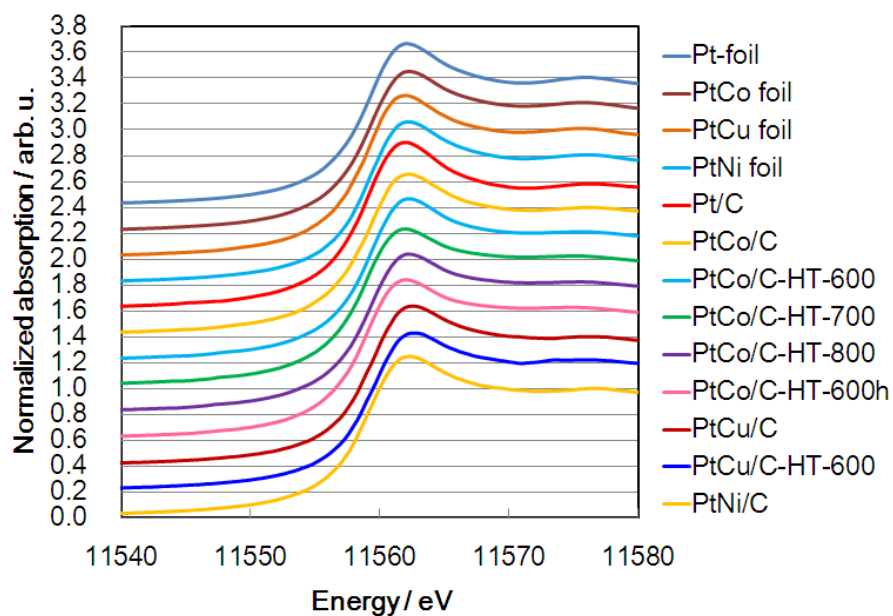


Figure 4.11 Pt L_{III}-edge XANES spectra of Pt foil, PtCo, PtCu, PtNi alloy foils, Pt/C, PtCo/C, PtCo/C-HTs, PtCu/C, PtCu/C-HT, and PtNi/C at 0.4V vs. RHE.

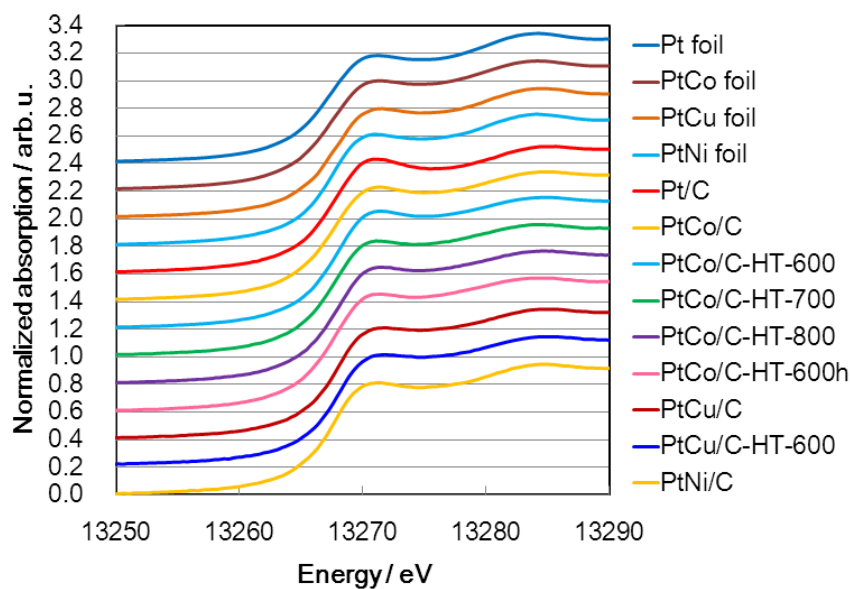


Figure 4.12 Pt L_{II}-edge XANES spectra of Pt foil, PtCo, PtCu, PtNi alloy foils, Pt/C, PtCo/C, PtCo/C-HTs, PtCu/C, PtCu/C-HT, and PtNi/C at 0.4V vs. RHE.

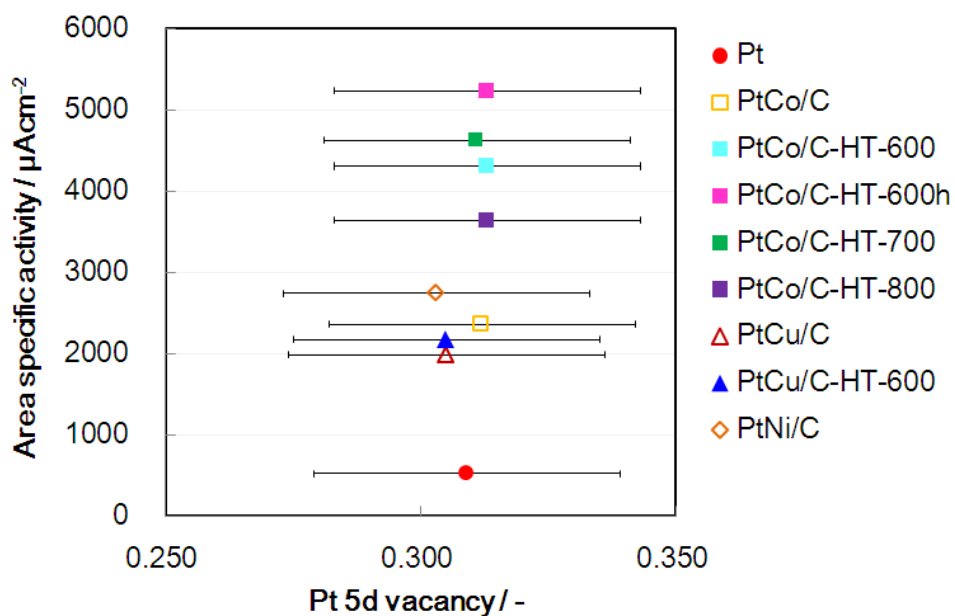


Figure 4.13 Correlation between Pt 5d vacancies of prepared electrocatalysts shown in Table 3 and area specific activities of those samples shown in Table 4.2.

4.3.3.2 EXAFS analysis of Reference foils and Pt/C base electrocatalyst

Firstly I analyzed the reference foils to confirm the validity of EXAFS analysis. Table 4.4 shows the curve fitting result using FEFF-derived phase shifts and amplitude functions.

For the curve fitting of PtCo alloy foil the mean free paths (MFs) for Pt and Co absorption edge were set to 1.1 and 0.59 nm to give a coordination number of 12. ΔE_0 for the Pt-Pt and Co-Co bond were fixed at the value for Pt and Co foils, respectively and the ΔE_0 for the Pt-Co, Co-Pt bond were determined in the curve fitting of PtCo alloy foil. These MFs and ΔE_0 s were used for the curve fitting of the following Pt alloy foils and PtCo nanoparticles. The Co-Co distance of PtCo random alloy foil was 0.263 ± 0.004 nm. It was much longer than that of Co foil. The Pt-Pt distance of PtCo random alloy foil was 0.275 ± 0.001 nm, which was almost the same as or a little shorter than that found in Pt foil. Co-Pt was found at 0.269 ± 0.001 nm a little shorter than that expected from average value of Co-Co and Pt-Pt distances in the alloy foil.

For the curve fitting analysis of PtCu and PtNi alloy foils I conducted the same procedure as in the case of PtCo foil. The mean free path for Cu and Ni absorption edge was set to 0.63 and 0.60 nm to give a coordination number of 12 respectively. The Cu-Cu distance of PtCu random alloy foil was 0.266 ± 0.003 nm. It was much longer than that of Cu foil as in the case of PtCo foil. The Pt-Pt distance of PtCu random alloy foil was 0.274 ± 0.001 nm, some contraction of Pt-Pt distance was observed. Pt-Cu distance was found at 0.269 ± 0.003 nm a little longer than that expected from average value of Cu-Cu and Pt-Pt distances as in the case of PtCo alloy foil. The Ni-Ni distance of PtNi random alloy foil was 0.258 ± 0.004 nm. It was much longer than that of Ni foil as in the case of PtCo and PtCu foil. The Pt-Pt distance of PtNi random alloy foil was 0.275 ± 0.001 nm, some small contraction of Pt-Pt distance was observed. Pt-Ni distance was found at 0.265 ± 0.002 nm longer than that expected from average value of Ni-Ni and Pt-Pt distances as in the case of PtCo and PtCu alloy foils.

Table 4.4 also shows structural parameters of Pt/C reference electrocatalyst. The Pt-Pt distance was 0.275 ± 0.001 nm, slightly shorter than that of Pt foil. The coordination number was also reasonable considering the average particle diameter of Pt/C 2.2 nm assuming cuboctahedral structure.

Table 4.4 Curve fitting parameters for reference Pt, Co, Cu, Ni foils, PtCo, PtCu, PtNi random alloy foils and Pt/C electrocatalyst at 0.4 V vs. RHE

Sample	Edge	Bond	Coordination number	Inter atomic distance / nm	Debye-Waller factor / nm
Pt foil	Pt-L _{III}	Pt-Pt	(12)	0.276 ± 0.001	0.0070 ± 0.0001
Co foil	Co-K	Co-Co	(12)	0.249 ± 0.001	0.0072 ± 0.0001
Cu foil	Cu-K	Cu-Cu	(12)	0.253 ± 0.001	0.0083 ± 0.0002
Ni foil	Ni-K	Ni-Ni	(12)	0.248 ± 0.001	0.0069 ± 0.0002
Pt/Co (9/1) foil	Pt-L _{III}	Pt-Pt	10.8 ± 0.8	0.275 ± 0.001	0.0075 ± 0.0001
		Pt-Co	1.0 ± 0.6	0.269 ± 0.003	0.0093 ± 0.0027
	Co-K	Co-Co	1.1 ± 0.6	0.264 ± 0.003	0.0035 ± 0.0035
		Co-Pt	10.4 ± 1.3	0.269 ± 0.001	0.0057 ± 0.0005
Pt/Cu (9/1) foil	Pt-L _{III}	Pt-Pt	10.3 ± 0.9	0.274 ± 0.001	0.0074 ± 0.0002
		Pt-Cu	1.0 ± 0.5	0.269 ± 0.003	0.0078 ± 0.0020
	Cu-K	Cu-Cu	1.2 ± 0.6	0.266 ± 0.003	0.0045 ± 0.0045
		Cu-Pt	10.5 ± 1.5	0.270 ± 0.001	0.0060 ± 0.0006
Pt/Ni (9/1) foil	Pt-L _{III}	Pt-Pt	10.8 ± 0.6	0.275 ± 0.001	0.0073 ± 0.0001
		Pt-Ni	1.1 ± 0.4	0.265 ± 0.002	0.0073 ± 0.0015
	Ni-K	Ni-Ni	1.4 ± 0.8	0.258 ± 0.004	0.0045 ± 0.0045
		Ni-Pt	10.0 ± 1.9	0.265 ± 0.002	0.0073 ± 0.0009
Pt/C	Pt-L _{III}	Pt-Pt	9.1 ± 1.6	0.275 ± 0.001	0.0084 ± 0.0004

4.3.3.3 EXAFS analysis of PtCo/C, PtCo/C-HTs, PtCu/C, PtCu/C-HT and PtNi/C electrocatalyst

Figures 4.14 and 4.15, respectively, shows k^3 -weighted Pt-L_{III} *in situ* EXAFS oscillations and their Fourier transforms for Pt/C PtCo/C, PtCo/C-HTs, PtCu/C, PtCu/C-HT and PtNi/C at 0.4V vs. RHE together with those of Pt and Pt alloy foils as reference. Table 4.6 summarized the curve fitting results of the prepared those electrocatalysts. The equations (5) and (6) shown in 3.2.4 of Chapter 3 were well satisfied within the error bars. For PtCo/C and PtNi/C curve fitting was conducted by Co-O and Co-Pt bonds or Ni-O and Ni-Pt bonds, respectively because Co or Ni atoms were severely oxidized as shown in the XANES spectrum in Fig. 4.8 and 4.10 respectively. In addition for the curve fitting of PtCo/C without heat treatment, ΔE_0 s for the Co-Pt and Co-Co were changed from those of PtCo alloy foil because the electronic state was considered different from the alloy foil as shown in the XANES spectra of Fig. 4.8. ΔE_0 s for the Cu-Pt and Cu-Cu were changed because the Cu-K edge XANES spectra of PtCu/C was not similar to that of PtCu alloy foil as shown in Fig. 4.9. For the curve fitting of PtNi/C, shift of ΔE_0 s for the Ni-Pt and Ni-O were conducted again by same reason as PtCo/C and PtCu/C.

Table 4.5 and 4.6 also contains coordination numbers expected from the assumption as random alloy particles. The diameters were expected as the value in Table 4.2 of section 4.3.2 determined from TEM. The shape of the nanoparticle was assumed to be cuboctahedral solid nanoparticles except of PtNi/C. Because the particle shape of PtNi/C was hollow structure as shown in the HAADF image and STEM-EDX line profile of Fig. 4.4, the surface shape of PtNi nanoparticle was assumed as cuboctahedron, and the shell thickness was assumed to be 2.5 nm and 8 atomic PtNi alloyed layers. The number of outer surface ridge atoms was assumed to be 13. The EXAFS-determined coordination numbers of all electrocatalyst samples coincided with the expected coordination numbers, which supported the idea that the alloy nanoparticles had the randomly mixed structure. I could say that the investigated

samples were not in the ordered intermetallic Pt₃Co or Pt₃Cu nanoparticle because Co-Co or Cu-Cu interaction was observed in the EXAFS analysis.

Table 4.5 Curve fitting results for heat treated PtCo/C and PtCo/C-HTs at 0.4 V vs.

RHE

Sample	Edge	Bond	Coordination		Atomic distance / nm	Debye-Waller factor / nm	R-factor
			Expected	Obtained			
PtCo/C	Pt L _{III}	Pt-Pt	7.9	8.1 ± 1.0	0.273 ± 0.001	0.0086 ± 0.0002	7.3
		Pt-Co	1.7	1.2 ± 1.0	0.268 ± 0.004	0.0161 ± 0.0056	
	Co K	Co-O	1.7	1.8 ± 0.5	0.199 ± 0.002	0.0100 ± 0.0026	8.2
		Co-Pt	7.9	7.9 ± 1.1	0.268 ± 0.001	0.0960 ± 0.0070	
PtCo/C -HT-600	Pt L _{III}	Pt-Pt	8.2	8.2 ± 1.0	0.270 ± 0.001	0.0078 ± 0.0002	4.4
		Pt-Co	2.7	2.3 ± 0.7	0.264 ± 0.002	0.0107 ± 0.0013	
	Co K	Co-Co	2.7	2.3 ± 0.5	0.261 ± 0.001	0.0088 ± 0.0012	3.2
		Co-Pt	8.2	7.9 ± 1.2	0.264 ± 0.001	0.0079 ± 0.0003	
PtCo/C -HT-700	Pt L _{III}	Pt-Pt	8.1	8.0 ± 1.0	0.270 ± 0.001	0.0075 ± 0.0002	6.1
		Pt-Co	2.8	2.5 ± 1.0	0.263 ± 0.002	0.0099 ± 0.0008	
	Co K	Co-Co	2.8	2.6 ± 0.9	0.260 ± 0.002	0.0100 ± 0.0016	2.5
		Co-Pt	8.1	8.2 ± 0.9	0.263 ± 0.001	0.0055 ± 0.0004	
PtCo/C -HT-800	Pt L _{III}	Pt-Pt	8.1	8.2 ± 1.7	0.270 ± 0.001	0.0086 ± 0.0005	4.3
		Pt-Co	2.8	2.3 ± 1.0	0.263 ± 0.003	0.0103 ± 0.0018	
	Co K	Co-Co	2.8	3.0 ± 0.8	0.259 ± 0.003	0.0098 ± 0.0013	7.9
		Co-Pt	8.1	7.3 ± 1.4	0.265 ± 0.001	0.0078 ± 0.0007	
PtCo/C -HT-600 h	Pt L _{III}	Pt-Pt	7.6	7.9 ± 1.4	0.269 ± 0.001	0.0079 ± 0.0003	8.1
		Pt-Co	3.2	2.5 ± 1.3	0.263 ± 0.003	0.0106 ± 0.0018	
	Co K	Co-Co	3.2	3.4 ± 1.1	0.261 ± 0.003	0.0122 ± 0.0017	2.5
		Co-Pt	7.6	7.1 ± 0.7	0.263 ± 0.001	0.0064 ± 0.0003	

Table 4.6 Curve fitting results for heat treated PtCu/C, PtCu/C-HT and PtNi/C at 0.4

V vs. RHE

Sample	Edge	Bond	Coordination number		Atomic distance / nm	Debye-Waller factor / nm	R-factor
			Expected	Obtained			
PtCu/C	Pt L _{III}	Co-Pt	7.6	7.1 ± 0.7	0.263 ± 0.001	0.0064 ± 0.0003	5.6
		Pt-Pt	7.0	6.7 ± 1.0	0.272 ± 0.001	0.0077 ± 0.0003	
	Cu K	Pt-Cu	2.6	2.0 ± 1.0	0.266 ± 0.003	0.0107 ± 0.0016	3.8
		Cu-Cu	2.6	2.0 ± 0.9	0.263 ± 0.003	0.0123 ± 0.0014	
PtCu/C -HT-600	Pt L _{III}	Cu-Pt	7.0	6.4 ± 1.2	0.267 ± 0.003	0.0108 ± 0.0008	5.4
		Pt-Pt	7.7	7.5 ± 1.1	0.272 ± 0.001	0.0073 ± 0.0003	
	Cu K	Pt-Cu	2.8	2.3 ± 1.1	0.267 ± 0.002	0.0092 ± 0.0019	3.2
		Cu-Cu	2.8	2.6 ± 0.7	0.264 ± 0.002	0.0093 ± 0.0010	
PtNi/C	Pt L _{III}	Cu-Pt	7.7	7.3 ± 0.9	0.267 ± 0.001	0.0082 ± 0.0005	4.0
		Pt-Pt	9.7	9.2 ± 0.9	0.273 ± 0.001	0.0085 ± 0.0002	
	Ni K	Pt-Ni	1.3	1.6 ± 0.6	0.266 ± 0.004	0.0107 ± 0.0017	2.6
		Ni-O	1.3	1.5 ± 0.3	0.202 ± 0.001	0.0055 ± 0.0014	
		Ni-Pt	9.7	10.2 ± 1.2	0.266 ± 0.001	0.0110 ± 0.0006	

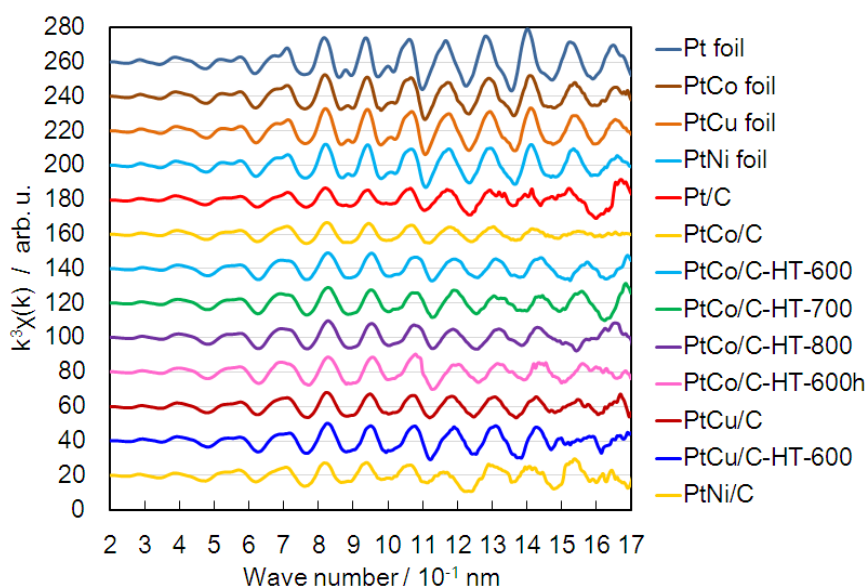


Figure 4.14 k^3 -weighted Pt-L_{III} edge EXAFS oscillation of Pt foil, PtCo, PtCu, PtNi alloy foils, Pt/C, PtCo/C, PtCo/C-HTs, PtCu/C, PtCu/C-HT, and PtNi/C at 0.4V vs. RHE.

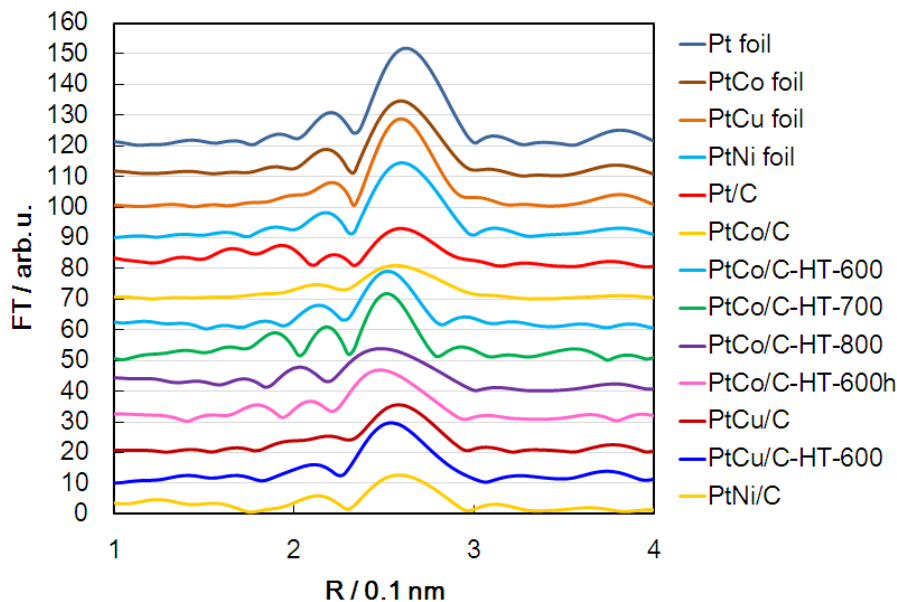


Figure 4.15 Fourier transform of k^3 -weighted Pt-L_{III} edge EXAFS oscillation of Pt foil, PtCo, PtCu, PtNi alloy foils, Pt/C, PtCo/C, PtCo/C-HTs, PtCu/C, PtCu/C-HT, and PtNi/C at 0.4V vs. RHE.

4.4. Discussion

4.4.1 Estimation of PtCo/C electrocatalysts internal structures

Because the determined coordination numbers and expected coordination numbers of heat treated PtCo/C-HTs as random alloy were approximately the same, the structures of those electrocatalyst were thought to be randomly mixed. On the other hand, a small peak at 33° originated from Pt₃Co intermetallic structure was observed in the XRD as shown in Fig. 4.5. To clarify the structure of PtCo/C-HT-600, -700, -800 (Pt₃Co) were not perfectly Pt₃Co intermetallic ordered structure, Hamilton method was conducted on PtCo/C-HTs samples with the hypothesis of Co-Co coordination number should be zero. Co K-edge EXAFS R-factor of one shell (Only Co-Pt) or two shells (Co-Co, Co-Pt) curve fittings and the confidence level of rejection are shown in Table 4.7. The validity of 2 shells curve-fitting was approved according to the Hamilton method and the Pt₃Co intermetallic structure was denied in more than 90 % confidence level. Adjustable parameter was 3 (Only Co-Pt) or 6 (Co-Co + Co-Pt). The Hamilton method indicated that the perfect formation of ordered Pt₃Co was rejected. However intermetallic Pt₃Co atomic ordering might be partially formed because I had a corresponding peak in XRD. I simulated XRD pattern and Pt₃Co peak could be reproduced even if 40% Co site was exchanged with Pt site in the Pt₃Co nanoparticles. The coordination number of the structure shown in Table 4.8 also satisfied the determined EXAFS coordination number within the error bar shown in Table 4.5. of section 4.3.3.2. As just described above combining XRD and EXAFS I concluded that the prepared Pt₃Co nanoparticles were not completely random alloy but not completely ordered intermetallic Pt₃Co. They had partially ordered Pt₃Co structure. The confidence level of PtCo/C-700-HT for the rejection was inferior to other samples. Hence it was considered that the atomic ordering was proceeded somewhat in the 700 °C treatment in my samples also as reported by Wang *et al.*⁵ This work showed that the XRD analysis is not sufficient to claim the formation of perfect intermetallic compound but combination of XAFS and XRD is necessary.

Table 4.7 Co K-edge one shell and two shells curve fitting R-factors of PtCo/C-HT-600, -700 and -800 at 0.4 V vs. RHE.

Sample	R-factor of two-shell	R-factor of one-shell	Confidence level of Pt ₃ Co intermetallic rejection
PtCo/C-HT-600	1.2	7.2	99.5 %
PtCo/C-HT-700	2.3	4.6	90.0 %
PtCo/C-HT-800	8.4	15.0	97.5 %

Table 4.8 Coordination numbers of Pt₃Co intermetallic modeled particle 40 % of the position of Co atoms were replaced with the Pt atoms in the particle.

Model	Co-Co	Co-Pt	Pt-Co	Pt-Pt
Pt ₃ Co intermetallic	0	10.6	3.6	7.1
40% replaced	2.1	8.5	2.9	7.9
Pt ₃ Co random alloy	2.7	8.0	2.8	8.0

4.4.2 Bond length and electronic effects to the ORR activity of electrocatalyst

According to Adzic *et al.*⁶ and Mukerjee *et al.*⁷ although there was the predominant correlation between Pt-Pt distances and area specific activities, excessive contraction induces deterioration of activity. Though when I reviewed previous reports^{5,8,9,10,11} on alloy electrocatalyst which showed enhanced activity tested by RDE measurement in HClO₄ solutions, the correlation of activity and Pt-Pt distance did not show the deterioration of activity at the short Pt-Pt distance of 0.265 nm as reproduced and shown in Figure 4.16. However Pt-Pt distances of Fig 4.16 are mixed with those determined by *in situ* XAFS⁹, *ex situ* XAFS¹¹, *ex situ* atomic PDF⁸ and *ex situ* XRD.^{5,10} Hence the correlation of Pt-Pt distances and enhanced area specific activities of alloy electrocatalysts should be studied again by the Pt-Pt distances determined by *in situ* XAFS to clarify the correlation.

The correlation of Pt-Pt distances and area specific activities of Pt/C, PtCo/C, PtCo/C-HTs, PtCu/C, PtCu/C-HT and PtNi/C prepared in this study are shown in Figure 4.17 with those of Wang *et al.*⁵ The 2nd vertical axis is for activity of electrocatalysts of Wang *et al.* The R² value of correlation between Pt-Pt distances and activities determined only by the electrocatalyst prepared in this research was 0.82. Critically strong correlation was observed. Pt-Pt distances of electrocatalysts of Wang *et al.* were determined by the lattice constants and shifted 0.002 nm to match the Pt-Pt distance of the both of this thesis and their Pt/C base electrocatalyst. The enhancement of area specific activity of prepared PtCo/C-HT-600h (Pt₂Co) was approximately 10 times compared with that of Pt/C. In addition enhancement of the area specific activities of heat treated PtCo/C-HTs at 600, 700, 800 °C, which were Pt₃Co and consisted of the random and ordered inner part and Pt rich surface, were 7 to 9 times. Activity enhancements observed in Pt₂Co was similar to that of Pt shell and completely ordered intermetallic Pt₃Co core nanoparticle reported by Wang *et al.* In addition Pt₃Co of Wang *et al.* heat treated at 400 °C also fitted the correlation of Pt-Pt distance and activity of this study. Hence the ordered Pt₃Co perfect intermetallic structure is not the essential conditions for the 12 times high ORR activity. The origin of activity enhancement of Pt₃Co reported by Wang *et al.* was Pt-Pt contraction.

Although the area specific activity of PtCo/C (Pt₅Co) was improved by the heat treatment process, the activity of PtCu/C (Pt₃Cu) was not improved by the heat treatment process. The reason was clarified that the contraction of Pt-Pt distance was not induced by the processes. Pt-Pt distances of PtCu/C and PtCu/C-HT were both 0.272 ± 0.001 nm. To clarify the reason of no contraction by heat treatment, further analysis would be needed for example the effects of heat treatment atmospheres and temperatures and keep times combining with several analysis methods.

In those prepared electrocatalyst samples, PtNi/C (Pt₉Ni/C) showed characteristic hollow structure and its Pt-Pt distance was 0.273 ± 0.001 nm. In spite of the characteristic structure the area specific activity was approximately 5 times higher than

that of Pt/C. In addition the enhanced activity did not apart from the correlation between area specific activities and Pt-Pt distances of other nanoparticles. On the other hand the Pt-Pt distance of PtNi (9/1) alloy foil containing same Co atomic percent as PtNi/C was determined as 0.275 ± 0.001 nm. Further contraction of Pt-Pt distance was observed in PtNi/C nanoparticle in spite of the same Co atomic concentration. The origin of contraction of Pt-Pt distance in PtNi/C was considered to be not only as nanoparticle but also specific hollow structure according to the Density functional theory (DFT) calculations as reported by Wang *et al.*¹

In addition the Pt-Pt distance of Pt/Au/C core-shell electrocatalyst described in chapter 3 determined in K-edge EXAFS analysis was 0.275 ± 0.001 nm and its area specific activity was $571 \mu\text{Acm}^{-2}$. As shown in in Table 3.1 and described in section 3.3.3 of chapter 3 Pt-Pt distance of Pt foil determined by K-edge EXAFS (0.278 ± 0.001 nm) was 0.003 nm longer than that determined by L-edge (0.275 ± 0.001 nm) in mean value. In addition Pt-Pt distance of Pt foil determined in L-edge of this chapter 4 was 0.276 ± 0.001 nm as shown in Table 4.4. Hence the Pt-Pt distance of Pt/Au/C was corrected to 0.273 ± 0.001 nm using the standard value of this chapter. Its IR corrected area specific activity was $734 \mu\text{Acm}^{-2}$. Hence the Pt-Pt distance including error and the area specific activity of Pt/Au/C also fits the correlation in Fig. 4.17. Accordingly the activity enhancement of the several shapes of and several added metal concentrations of nanoparticles including hollow nanoparticles and core-shell nanoparticles have the same correlation with the contraction of Pt-Pt distance.

As regards to Pt 5d vacancy, the determined vacancies of Pt foil, reference alloy foils, and prepared electrocatalysts are listed in Table 4.3 of section 4.3.3.1. In this study the increments of the vacancies were included in errors and the correlation between Pt 5d vacancies and activities was not clarified or almost nothing. The reason remains unclear. To elucidate the reason of no change of Pt 5d vacancies, theoretical calculation with realistic cluster structure would be helpful because the similar study was reported by Jia *et al.*¹² However the study was conducted on the unrealistic small

nanocluster. Hence the study should be done again with the realistic cluster.

As regards to the activity deterioration by the excess contraction of Pt-Pt distance reported by Mukerjee *et al.*,⁷ I studied carefully in this thesis. Although Pt-Pt distance of Pt foil they reported was 0.277 nm, Pt-Pt distance of Pt foil of this study was 0.276 ± 0.001 nm. Hence the distance would be compared by shifting 0.001 nm. According to Mukerjee *et al.* the activity hit the peak at 0.271 nm of PtCr, deterioration was observed from 0.270 nm of PtFe to 0.268 nm of PtCo and PtNi. On the other hand in this study Pt-Pt distance of Pt₂Co would be 0.270 ± 0.001 nm shifting by 0.001 nm of Pt-Pt distance. Although deterioration should be observed in this study either, if the report of Mukerjee *et al.* was correct, it was not observed. Hence some other elusive reason should have existed in the deterioration of activity in the study of Mukerjee *et al.* One of the reasons is the activity testing method. In the study of Mukerjee *et al.* the activities were tested in typical cell with membrane electrode assembly. In that system the surface condition of electrocatalyst would be governed by the fabrication process of electrocatalyst layers and activity would be changed. Obviously there would be the limitation of activity enhancement in the contraction of Pt-Pt distance by adding the excess Co atoms, because some of the Pt atoms on the surface of nanoparticle would be isolated, then several types of adsorption mechanism of oxygen molecule on Pt atom including bridge type^{13,14} would be unfavorable and the first step of ORR would be deteriorated.

The correlation of Pt-Pt distances and activities of electrocatalysts prepared in this study as shown in Fig. 4.17 and that of the previous reports in Fig. 4.16 are again reproduced and shown in Figure 4.18 and R^2 value was determined as 0.27. In Fig. 4.18 the activities of electrocatalysts prepared in this study were plotted by the IR uncorrected values to compare rightly with other researches. As a result, although Pt-Pt distances were determined by the several measurement methods, weak correlation was observed. Hence Pt-Pt distance has strong effect on activity and it should be contracted for activity enhancement.

Conclusively to achieve the high area specific activity for ORR, the shapes of, Pt 5d vacancies of and structures of the nanoparticles are not considered to be the direct origin of enhanced area specific activity. However Pt-Pt bond distance has to be contracted for the enhancement of area specific activity. The shapes, the added metal concentration and the structures are methods to induce the contraction of Pt-Pt distance. In addition there is no deterioration by excess contraction of Pt-Pt distance.

Meanwhile the effect of Pt-Pt contraction on ORR still remains elusive. ORR activity is often discussed combining with d-band electronic states. The role of Pt-Pt contraction on d-band is explained as an enhancement of d-orbital overlapping and broadening leading to downshift of d-band energy.^{12,15,16} The role of the downshift of d-band center on ORR process is simply explained as the weakness of adsorption energy of oxygen species including OH and O according to Hammer *et al.*¹⁷ The reason of activity volcano plot is reported combining with the limitation of two rate determining steps; OH inhibits removal and OOH intermediate formation on the surface according to Tripković *et al.*¹⁸ According to them ideally it would be desirable to have weaker OH and stronger OOH binding to the surface. Because binding energies of OH and OOH cannot be changed independently, material with the tradeoff of these two limiting regimes should be controlled to the best balance for ORR. Therefore PtM electrocatalyst which has an intermediate oxygen species' binding energy was found to be close to the top of the volcano plot.¹⁸

However as shown in this thesis, there was no activity deterioration by Pt-Pt contraction as far as 0.269 nm. In addition volcano-plot of the correlation between Pt-Pt distance and activity was not observed in the review of previous reports as shown in Fig. 4.16. In fact previous reports on the activity enhancement of PtM electrocatalyst discussed with the adsorption energy of oxygen species combining with d-band center, and the relations with the each ORR elementary steps were not studied well.^{6,19-27} Though ORR reaction mechanism is complex and consists of several elementary steps, including oxygen molecule adsorption, O-O bond breaking, O and

OH or OOH reduction.^{25,28,29,30} Hence ORR activity enhancement of prepared electrocatalysts should not be explained simply by d-band center downshift and balance of adsorption energy.

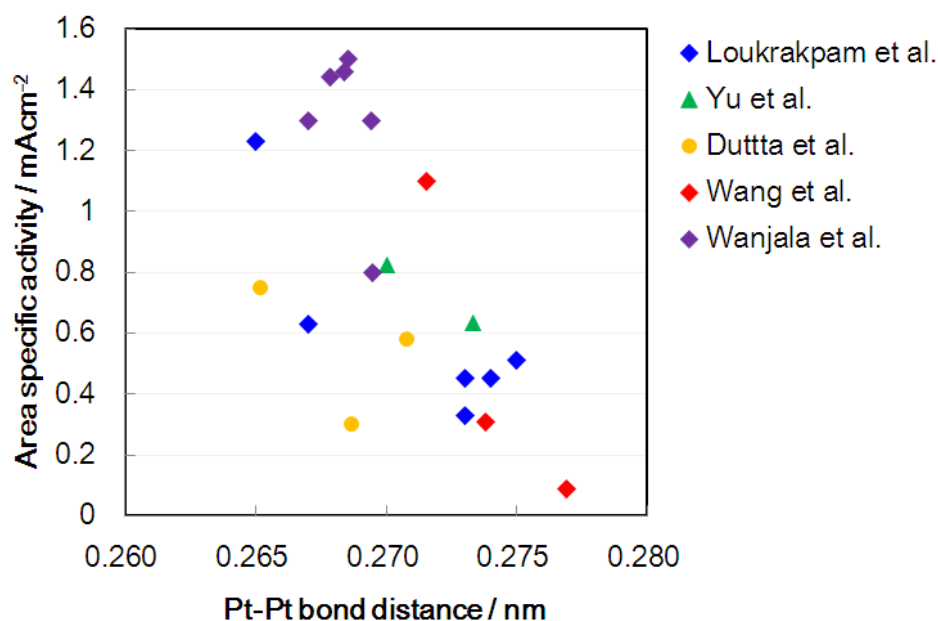


Figure 4.16 Correlation between Pt-Pt distances and area specific activities of Pt alloy electrocatalysts of previous reports.^{5,8,9,10,11}

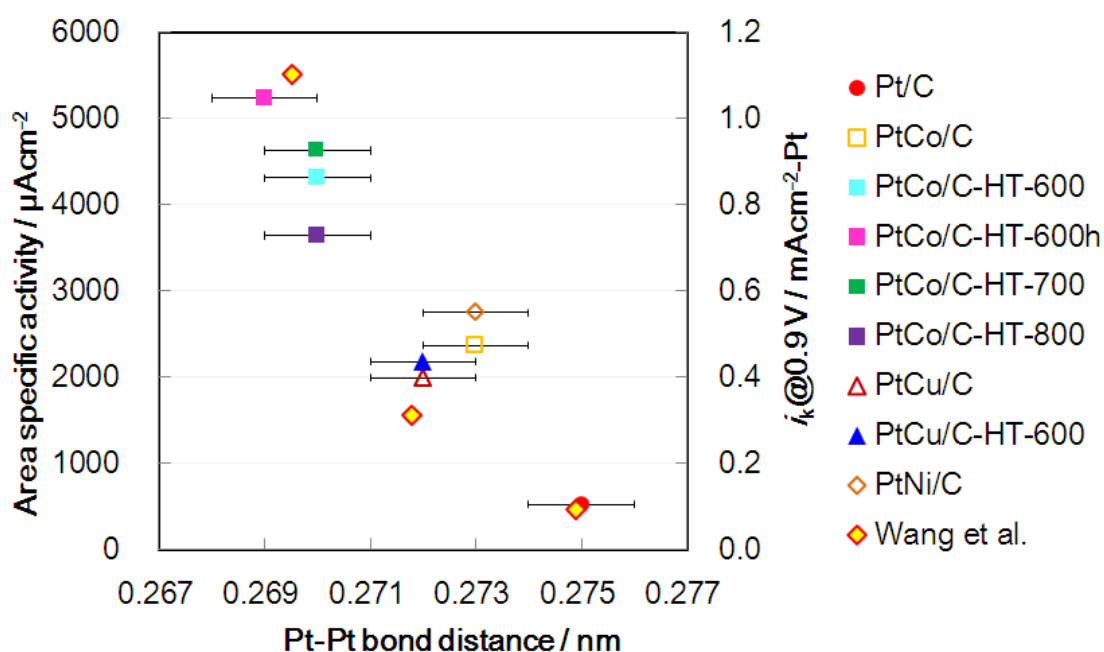


Figure 4.17 Correlation between Pt-Pt distances at 0.4 V vs. RHE. and area specific activities of Pt/C, PtCo/C, heat treated PtCo/C-HTs, PtCu/C, heat treated PtCu/C-HT and PtNi/C hollow structure with that of Wang *et al.*⁵ First vertical axis is for the activity of this study and the 2nd vertical axis is for that of Wang *et al.*

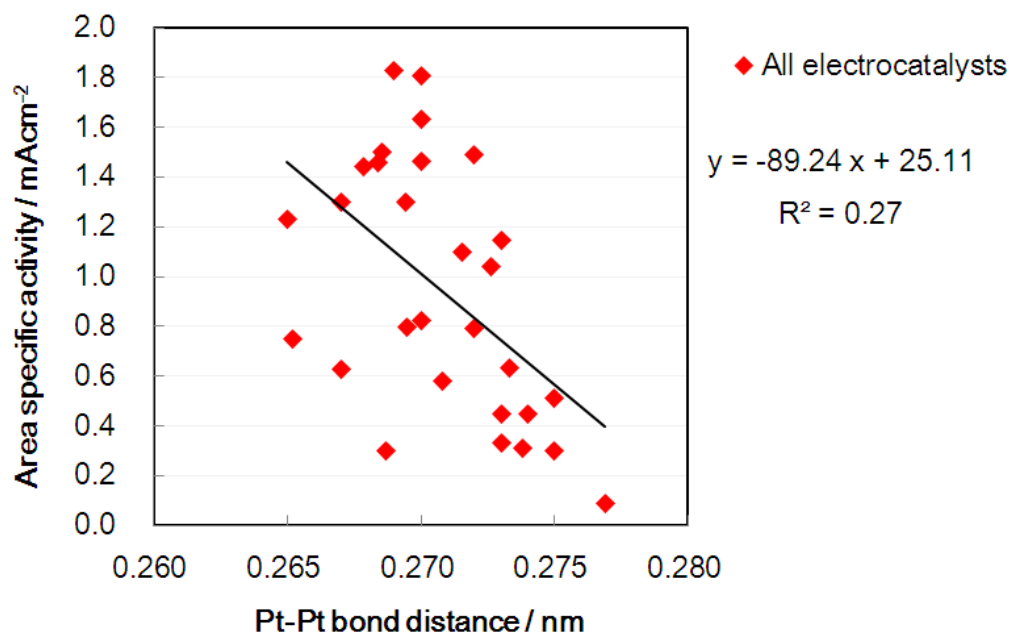


Figure 4.18 Correlation between Pt-Pt distances and area specific activities of electrocatalysts reported previously and prepared in this study.

4.5 Conclusions

Carbon-supported PtM (PtCo/C, PtCu/C and PtNi/C) alloy electrocatalysts were prepared. They showed much higher area specific activities than Pt/C.

XAFS analysis has demonstrated that these PtM particles have mainly random alloy structure and that there is a strong correlation between Pt-Pt bond distances and area specific activities. In addition Pt-Pt distance should be contracted for activity enhancement in any types of PtM alloy electrocatalysts. However activity deterioration by excess Pt-Pt contraction was not observed. On the other hand relation with the Pt 5d vacancy was not observed.

Next step of this study is understanding correlation between Pt-Pt distances and essential each elementary ORR steps more precisely through the theoretical calculation to elucidate the reason of activity enhancement by Pt-Pt contraction.

4.6 References

- ¹ Wang, J. X.; Ma, C.; Choi, Y.; Su, D.; Zhu, Y.; Liu, P.; Si, R.; Vukmirovic, M. B.; Zhang, Y.; Adzic, R. R., Kirkendall Effect and Lattice Contraction in Nanocatalysts: A New Strategy to Enhance Sustainable Activity. *Journal of the American Chemical Society* **2011**, *133*(34), 13551-13557.
- ² Li, W.; Lane, A. M., Resolving the HUPD and HOPD by DEMS to determine the ECSA of Pt electrodes in PEM fuel cells. *Electrochemistry Communications* **2011**, *13*(9), 913-916.
- ³ Gaur, A.; Shrivastava, B. D.; Joshi, S. K., Copper K-edge XANES of Cu(I) and Cu(II) oxide mixtures. *Journal of Physics: Conference Series* **2009**, *190*(1), 012084.
- ⁴ Mansour, A. N.; Cook, J. W.; Sayers, D. E., Quantitative technique for the determination of the number of unoccupied d-electron states in a platinum catalyst using the L_{2,3} x-ray absorption edge spectra. *The Journal of Physical Chemistry* **1984**, *88*(11), 2330-2334.
- ⁵ Wang, D.; Xin, H. L.; Hovden, R.; Wang, H.; Yu, Y.; Muller, D. A.; DiSalvo, F. J.; Abruña, H. D., Structurally ordered intermetallic platinum–cobalt core–shell nanoparticles with enhanced activity and stability as oxygen reduction electrocatalysts. *Nat Mater* **2013**, *12*(1), 81-87.
- ⁶ Adzic, R. R.; Zhang, J.; Sasaki, K.; Vukmirovic, M. B.; Shao, M.; Wang, J. X.; Nilekar, A. U.; Mavrikakis, M.; Valerio, J. A.; Uribe, F., Platinum Monolayer Fuel Cell Electrocatalysts. *Topics in Catalysis* **2007**, *46*(3-4), 249-262.
- ⁷ Mukerjee, S.; Srinivasan, S.; Soriaga, M. P.; McBreen, J., Role of Structural and Electronic Properties of Pt and Pt Alloys on Electrocatalysis of Oxygen Reduction. *Journal of The Electrochemical Society* **1995**, *142*(5), 1409-1422.
- ⁸ Loukrakpam, R.; Shan, S.; Petkov, V.; Yang, L.; Luo, J.; Zhong, C.-J., Atomic Ordering Enhanced Electrocatalytic Activity of Nanoalloys for Oxygen Reduction Reaction. *The Journal of Physical Chemistry C* **2013**, *117*(40), 20715-20721.
- ⁹ Yu, Z.; Zhang, J.; Liu, Z.; Ziegelbauer, J. M.; Xin, H.; Dutta, I.; Muller, D. A.; Wagner, F. T., Comparison between Dealloyed PtCo₃ and PtCu₃ Cathode Catalysts for Proton Exchange Membrane Fuel Cells. *Ibid.* **2012**, *116*(37), 19877-19885.
- ¹⁰ Wanjala, B. N.; Fang, B.; Shan, S.; Petkov, V.; Zhu, P.; Loukrakpam, R.; Chen, Y.; Luo, J.; Yin, J.; Yang, L.; Shao, M.; Zhong, C.-J., Design of Ternary Nanoalloy Catalysts: Effect of Nanoscale Alloying and Structural Perfection on Electrocatalytic Enhancement. *Chemistry of Materials* **2012**, *24*(22), 4283-4293.
- ¹¹ Dutta, I.; Carpenter, M. K.; Balogh, M. P.; Ziegelbauer, J. M.; Moylan, T. E.; Atwan, M. H.; Irish, N. P., Electrochemical and Structural Study of a Chemically Dealloyed PtCu Oxygen Reduction Catalyst. *The Journal of Physical Chemistry C* **2010**, *114*(39), 16309-16320.
- ¹² Jia, Q.; Segre, C. U.; Ramaker, D.; Caldwell, K.; Trahan, M.; Mukerjee, S., Structure–property–activity correlations of Pt-bimetallic nanoparticles: A theoretical study. *Electrochimica Acta* **2013**, *88*(0), 604-613.
- ¹³ Yeager, E., Recent Advances in the Science of Electrocatalysis. *Journal of The Electrochemical Society* **1981**, *128*(4), 160C-171C.
- ¹⁴ Chan, A. W. E.; Hoffmann, R.; Ho, W., Theoretical aspects of photoinitiated chemisorption, dissociation, and desorption of oxygen on platinum(111). *Langmuir* **1992**, *8*(4), 1111-1119.
- ¹⁵ Kitchin, J. a. N. o. r., J. and Barteau, M. and Chen, J., Role of Strain and Ligand Effects in the Modification of the Electronic and Chemical Properties of Bimetallic Surfaces. *Physical Review Letters* **2004**, *93*(15), 156801.
- ¹⁶ Mavrikakis, M. a. H., B. and Norskov, J., Effect of Strain on the Reactivity of Metal Surfaces. *Ibid.* **1998**, *81*(13), 2819.

-
- ¹⁷ Hammer, B.; Nørskov, J. K., Electronic factors determining the reactivity of metal surfaces. *Surface Science* **1995**, *343* (3), 211-220.
- ¹⁸ Tripković, V.; Skúlason, E.; Siahrostami, S.; Nørskov, J. K.; Rossmeisl, J., The oxygen reduction reaction mechanism on Pt(111) from density functional theory calculations. *Electrochimica Acta* **2010**, *55* (27), 7975-7981.
- ¹⁹ Zhang, J.; Lima, F. H. B.; Shao, M. H.; Sasaki, K.; Wang, J. X.; Hanson, J.; Adzic, R. R., Platinum Monolayer on Nonnoble Metal–Noble Metal Core–Shell Nanoparticle Electrocatalysts for O₂ Reduction. *The Journal of Physical Chemistry B* **2005**, *109* (48), 22701-22704.
- ²⁰ Stamenkovic, V. R.; Mun, B. S.; Mayrhofer, K. J. J.; Ross, P. N.; Markovic, N. M., Effect of Surface Composition on Electronic Structure, Stability, and Electrocatalytic Properties of Pt-Transition Metal Alloys: Pt-Skin versus Pt-Skeleton Surfaces. *Journal of the American Chemical Society* **2006**, *128* (27), 8813-8819.
- ²¹ Lima, F. H. B.; de Castro, J. F. R.; Santos, L. G. R. A.; Ticianelli, E. A., Electrocatalysis of oxygen reduction on carbon-supported Pt–Co nanoparticles with low Pt content. *Journal of Power Sources* **2009**, *190* (2), 293-300.
- ²² Friebel, D.; Viswanathan, V.; Miller, D. J.; Anniyev, T.; Ogasawara, H.; Larsen, A. H.; O’Grady, C. P.; Nørskov, J. K.; Nilsson, A., Balance of Nanostructure and Bimetallic Interactions in Pt Model Fuel Cell Catalysts: In Situ XAS and DFT Study. *Journal of the American Chemical Society* **2012**, *134* (23), 9664-9671.
- ²³ Chen, S.; Sheng, W.; Yabuuchi, N.; Ferreira, P. J.; Allard, L. F.; Shao-Horn, Y., Origin of Oxygen Reduction Reaction Activity on “Pt₃Co” Nanoparticles: Atomically Resolved Chemical Compositions and Structures. *The Journal of Physical Chemistry C* **2009**, *113* (3), 1109-1125.
- ²⁴ Stamenkovic, V. R.; Fowler, B.; Mun, B. S.; Wang, G.; Ross, P. N.; Lucas, C. A.; Marković, N. M., Improved Oxygen Reduction Activity on Pt₃Ni(111) via Increased Surface Site Availability. *Science* **2007**, *315* (5811), 493-497.
- ²⁵ Stamenkovic, V. R.; Mun, B. S.; Arenz, M.; Mayrhofer, K. J. J.; Lucas, C. A.; Wang, G.; Ross, P. N.; Markovic, N. M., Trends in electrocatalysis on extended and nanoscale Pt-bimetallic alloy surfaces. *Nat Mater* **2007**, *6* (3), 241-247.
- ²⁶ J, Z.; M.B, V.; K, S.; F, U.; R.R, A., Platinum monolayer electrocatalysts for oxygen reduction: Effect of substrates, and long-term stability. *Journal of the Serbian Chemical Society* **2005**, - 70 (- 3), - 525.
- ²⁷ Zhang, J.; Vukmirovic, M. B.; Xu, Y.; Mavrikakis, M.; Adzic, R. R., Controlling the Catalytic Activity of Platinum-Monolayer Electrocatalysts for Oxygen Reduction with Different Substrates. *Angewandte Chemie International Edition* **2005**, *44* (14), 2132-2135.
- ²⁸ Nilekar, A. U.; Mavrikakis, M., Improved oxygen reduction reactivity of platinum monolayers on transition metal surfaces. *Surface Science* **2008**, *602* (14), L89-L94.
- ²⁹ Tian, F.; Anderson, A. B., Effective Reversible Potential, Energy Loss, and Overpotential on Platinum Fuel Cell Cathodes. *The Journal of Physical Chemistry C* **2011**, *115* (10), 4076-4088.
- ³⁰ Wang, J. X.; Zhang, J.; Adzic, R. R., Double-Trap Kinetic Equation for the Oxygen Reduction Reaction on Pt(111) in Acidic Media†. *The Journal of Physical Chemistry A* **2007**, *111* (49), 12702-12710.



Chapter 5

General conclusions and general discussions

5.1 General conclusions

In this study several types of bimetallic nanoparticle electrocatalysts were prepared to make correlation between the ORR activities and structural factors such as Pt-Pt distances, electronic states, shapes, inner structures, added metals, concentration of added metals to clarify the activity governing factor.

In this thesis I revealed how EXAFS is important and provides the fruitful information of nanoparticles especially under working conditions. I represent the examples as follows.

In structural analysis of Pt/Au core-shell, although Pt-Pt distance is the activity governing factor, Pt-Pt distance of Pt shell is not determined from XRD because XRD does not have the element selectivity. Instead Pt shell is as much as two layers and too thin to give diffraction pattern. However by EXAFS Pt-Pt distance of the Pt shell can be determined as described in section 3.3.3.3 of chapter 3 because EXAFS utilizes the X-ray absorption of characteristic atoms and element selectivity. For the confirmation of Pt/Au as core-shell structure, a typical analysis method as STEM-HAADF is inadequate because Pt and Au are neighboring on periodic table, and the scattering abilities are almost same. Although STEM-EDX is another structural analysis method of nanoparticle, it is again inadequate for thin Pt/Au core-shell because the shell thickness is too thin for its spatial resolution. In addition those structural analysis methods are available only in vacuum not under working condition. However the coordination numbers of Pt/Au determined directly by EXAFS can provide the core-shell structure directly under working conditions.

What I found through this thesis is as follows.

Metal bond length of inner part of bimetallic nanoparticles cannot be speculated from the bulk monometallic lattice structure or bimetallic bulk lattice structure as in the comparison of EXAFS reference foils with alloy clusters. The monometallic nanocluster structure is quite different from the corresponding bimetallic nanocluster structure. It is analogous to a eutectic mixture. Although both of the pure metal and

the eutectic alloy show randomly mixed liquid more than melting point, only the eutectic alloy shows specific mixed structure of two solid solution phases under the eutectic isotherm of the phase diagram. In the case of this study both of the bimetallic bulk and the monometallic bulk showed similar structure as EXAFS reference foils, the bimetallic nanoparticle showed the different structure compared with the monometallic nanocluster. The difference between the bimetallic nanoparticle and bimetallic bulk is not only in bond length but also in its inner and surface structure or atomic arrangement as follows. Pt-Pt contraction of Pt shell of Pt/Au core-shell was unimaginable from the Pt monolayer on Au single crystal and PtAu alloy foil as described in section 3.3.3 of chapter 3. The mechanism of contraction remains still elusive. Besides PtNi hollow nanoparticle shows the shorter Pt-Pt distance than PtNi bulk in spite of the same Pt/Ni atomic ratio as shown in section 4.3.3 of chapter 4. One of the reasons is the specific hollow structure according to theoretical calculation by Wang *et al.*¹

There are two categories in bimetallic nanoparticles. One is segregated type and the other is alloy type. The segregated type could be classified as core-shell type and cluster in cluster type. I tried to make core-shell type in this thesis as described in chapter 3. Alloy type can be classified to three categories: ordered alloy, random alloy and heterobondphilic alloy. Ordered alloy was formed in previous papers with diffraction studies.^{2,3} However EXAFS revealed that the random alloy structure is preferred because analysis only by the diffraction pattern is not sufficient to reveal the detail inner structure of nanoparticles as described in section 4.4.1 of chapter 4. In fact although XRD pattern of Pt₃Co alloy electrocatalysts prepared in this study showed the Pt₃Co specific intermetallic diffraction peak in some degree, their coordination numbers determined by EXAFS did not support the complete Pt₃Co intermetallic structure. The structure of Pt₃Co nanoparticle whose coordination numbers was within errors determined by EXAFS still showed the Pt₃Co intermetallic diffraction pattern according to diffraction pattern calculation. As a result of combining analysis of EXAFS and XRD, the prepared Pt₃Co electrocatalysts were clarified as intermediate of randomly

mixed and intermetallic, partly intermetallic and random. This is due to the high mobility of atoms in the nanoparticles with larger surface ratio compared with bulk or importance of nanoscale phase properties.⁴

In any way by state-of-art preparation techniques I was able to prepare the bimetallic alloy nanocluster with controlling these inner structures and identified these atomic level structures. In this work I used mainly EXAFS but electron microscopy technique also has made great advances recently. Especially spherical aberration correction STEM-EDX provided the atomic imaging and elements analysis using fluorescence X-ray. I was able to show the core-shell structure of PtCo nanoparticle using analytical STEM-EDX as described in section 4.3.1 of chapter 4. But I should notice that careful background and normalization must be carried out to conclude the correct structure.

XANES can provide the electronic state of Pt through the white line peak analysis.⁵ It corresponds to the unoccupied state of density of d-electron level. The d-electron level is directly related to the conduction band of the Pt nanoparticle so that we can infer the relation between ORR activity and d electronic state. As an example of XANES advantage compared with other methods is penetration ability of X-ray. Although electronic states determined by XPS give valuable information, XPS is difficult methods under electrochemical working conditions, because the emitted electron cannot penetrate the electrolyte solution. However XAFS is able to determine the Pt 5d vacancies under working conditions by penetration ability of X-ray as described in section 3.4.2 of chapter 3 and section 4.3.3.1 of chapter 4. Although in this thesis Pt 5d vacancies of prepared PtM alloy electrocatalysts were almost the same.

Now is the time to discuss the governing factors for ORR activity.

5.2 General discussions

5.2.1 The effect of Pt-Pt contraction on ORR activity

Although I have clarified that the Pt-Pt contraction is essential for the enhancement of ORR activity as described in section 4.4.2 of chapter 4, the detail effect of contraction of Pt-Pt distance on ORR still remains elusive because the previous researches discussed ORR with the adsorption energy of oxygen species as O or OH mainly from the standpoint of inhibition of the reaction sites and the removal of intermediate oxygen species, combining with the downshift of d-band center induced by Pt-Pt contraction or ligand effect of added metal and did not study further the correlation with each elementary ORR steps as follows.⁶⁻¹⁶

Zhang *et al.* prepared Pt shell, AuNi or PdCo core electrocatalysts and discussed the activity measured by RDE testing with d-band center combining oxidation states of core-shell compared with Pt/C determined by XANES.⁶ The core-shell expected to have lower d-band center from DFT calculation showed the smaller oxidation white line peak of XANES. Stamenkovic *et al.* studied the Pt skin or skeleton alloy model electrode and analyzed its UPS spectra and determined d-band center and activity measured by RDE testing. They discussed activity improvement with the position of the metallic d-band center vs. Fermi level, combining oxygen species adsorption properties of the surface.⁷ Adzic *et al.* reported several Pt monolayer core-shell electrocatalysts for ORR and discussed their activity combining oxidation states of Pt using XANES white line peak, OH inhibits and d-band center downshift expected by Pt-Pt contraction and ligand effect by core-shell structure.⁸ Lima *et al.* prepared PtCo electrocatalysts and discussed their activity enhancements combining with XANES white line peak and OH inhibits and d-band center downshift expected by ligand effect of Co alloying.⁹ Chen *et al.* prepared Pt rich shell and PtCo core nanoparticles and discussed enhanced activity with the Pt-Pt distance obtained from synchrotron XRD, surface coverage of oxygenated species determined from cyclic voltammograms, and oxidation states determined by XANES white line peaks.¹⁰ The reason of activity

enhancement was reported as the reduction in coverage of surface-blocking species by the downshift of d-band center. Stamenkovic *et al.* studied PtNi model electrode with the UPS spectra again and discussed its activity enhancement with the downshift of d-band center.¹¹ Stamenkovic *et al.* summarized and reported the reason of volcano type activity enhancement as d-band center shift of PtM flat model electrode governed with the balance of adsorption energies of reactive intermediates and surface coverage by blocking species.¹² Friebel *et al.* studied Pt island or Pt monolayer model electrode formed on Rh (111), their activity, structures combining EXAFS, then discussed the volcano-plot activity enhancement with the change of adsorption energy of oxygen species due to a shift of the d-band center to lower energy caused by strain and vertical ligand effects.¹⁵ Zhang *et al.* studied Pt monolayer model electrode formed on several kinds of single crystals and discussed reason of enhanced activity through the volcano-plot correlation of d-band center and activity, correlation of oxygen binding energy and activation energy of oxygen molecule dissociation then concluded O-O bond breaking and the hydrogenation of reactive intermediates have to be facile at the cathode.¹⁴ Jia *et al.* studied electronic state of PtM nanocluster reported in Mukerjee *et al.*¹⁷ using DFT calculation and discussed the activity enhancement with the Pt-Pt contraction, d-band center shift and oxygen adsorption energy, then concluded shift of d-band center is significant.¹⁶ However as described in chapter 4 there was not volcano-plot correlation between Pt-Pt distance and activity tested in HClO₄ solution. Hence it means that the effect of d-band center downshift on activity remains elusive.

Eventually previous studies described above discussed the activity enhancement with d-band center shift and adsorption energy of oxygen species. However ORR reaction mechanism is complex and consists of several elementary steps, including oxygen molecule adsorption, O-O bond breaking, O and OH or OOH reduction.^{14,18,19,20} Hence ORR activity enhancement would not be explained simply by the shift of d-band center and balance of adsorption energy of oxygen species. The correlation with each ORR steps has to be studied for further understanding.

Future direction of this research is to understand correlation between Pt-Pt contraction and essential elementary ORR steps combining with the electron charge transfer between Pt surface and oxygen molecule or oxygen species, and their adsorption structures. To clarify that effect analysis from the theoretical standpoint such as large-scale DFT calculation, for example the natural bond orbitals (NBOs) method^{21,22} using calculation program of Open MX²³ would be needed. NBOs method provides a Lewis-structure type orbital representation expressing localized bonding and lone pair. Hence one can analyze properties of chemical bonds, intermolecular interactions, and chemical reactivity. It would be helpful to understand the interaction between Pt surface and oxygen species including electron transfer.

When conducting the theoretical calculation, the realistic size cluster model is required. The reason is as follows. According to the preliminary DFT studies of oxygen molecule adsorption on (100) surface of Pt₁₄₇ cuboctahedral nanocluster, surface Pt atoms adsorbed with oxygen molecule are speculated to be lifted by interaction with adsorbent.²⁴ Hence if the size of cuboctahedral cluster is as small as Pt₁₄₇, appropriate bridge adsorption mechanism and structural change by oxygen molecular on an actual (111) surface would be impossible because (111) surface of Pt₁₄₇ has only one Pt atom which is not located on the ridge. The structural change of Pt nanocluster induced by the interaction with oxygen molecule would be different depending on the adsorbed position. For that reason the size of cuboctahedral nanoparticle has to be larger than Pt₃₀₉ for correct study of adsorption structure. In addition the internal and external structure determined by EXAFS, XRD and STEM is needed to build the realistic cluster model for the good validation with the experimental results. Theoretical study on the realistic cluster structure and size is the currently missing point to understand the real catalysis of electrocatalysts. The effect of excess Pt-Pt contraction on activity, the effect of alloying on Pt 5d vacancies would be further suggested by that theoretical calculation.

5.2.2 Activity enhancement in an actual fuel cell stack

In this thesis I discussed activity governing factor with the activity measured by typical RDE testing methods. However, the Pt surface condition of actual FC stack would be different from that of the RDE testing condition. The reason is as follows. To determine the activity at the RDE testing method, LSVs are measured from the lower potential as 0.2 V to 1.2 V vs. RHE anodically sweep as shown in Fig. 3.5 in chapter 3. Hence oxide formation on the surface of Pt electrocatalyst of the testing condition is limited and it depends on the properties of electrocatalysts. This method is not wrong from the standpoint to determine the activity of electrocatalyst with limited oxide inhabitation on the surface of electrocatalysts. On the other hand in an actual FCEV, FC stack is mainly operated at high potential around 0.8 V at the idle or the economy point of an automobile. Hence the surface of electrocatalyst is usually almost covered with Pt oxides. When the driver of the FCEV suddenly increases the pressure on the accelerator pedal at for example a junction of expressway, because output power is needed, the current density would be increased to satisfy the required output power and the potential would be lowered around 0.6 V vs. RHE which is the lower limit depending on each FC systems. Then the most of the oxides would be reduced and the surface of the Pt electrocatalyst would be similar to that of the RDE testing condition. However after the potential lowering around 0.6 V, the potential would be cathodically shifted to around 0.8 V because the constant maximum power would not be needed and the required output power of FCEV changes depending on the surrounding traffic. Then the surface oxide would be formed again and it would not be reduced until maximum output power would not be needed. In addition maximum output power would not be needed for typical city traffic of automobiles. Hence at the most of the operation, driving of automobiles, Pt surface would be covered with oxides and the Pt surface is completely different from that of typical RDE testing conditions.

Markovic *et al.* suggested the ORR reaction rate equation below,²⁵

$$i = i_0 \times (1 - \theta) \times \exp\left(-\frac{\beta F \eta}{RT}\right) \times \exp\left(-\frac{\gamma R \theta}{RT}\right)$$

where i_0 is the exchange current density, θ is the ratio of the surface of the oxide formation, β and γ are the symmetry factors, F is the faraday constant, R is the gas constant and T is temperature. Although exchange current density i_0 was improved by enhancement of activity thorough Pt-Pt contraction, the effect of θ would be still large for FC stack in actual world.

Next question is what kinds of electrocatalysts show the smaller θ in an actual world. The structures of several types of electrocatalysts including the electrocatalyst which are already given up have to be studied to know the governing factor of smooth reduction of Pt oxide coverage and ever inhibition of the oxide coverage formation in an actual world when FC stack is operated continuously around 0.8 V.

In parallel different approach should be tried to achieve the activity enhancement and the reduction of Pt usage. Although Pt-Pt distance of PtCo was contracted by alloying and existence of Co atoms, Pt-Pt distance of Pt/Au core-shell was contracted by surface segregation, and it was not governed by core Au-Au distance. Hence for core-shell structure there is the possibility of Pt-Pt contraction with the core material whose atomic distance is larger than that of Pt nanoparticle. In addition the core material is able to be selected from the materials which have resistance to dissolution in acid solution, because added 3d transition atoms of Pt bimetallic alloy would not be perfectly protected from dissolution and activity would be deteriorated in the long-term operation. For that core-shell nanoparticle there is the possibility of achievement of area-specific activity enhancement, increase of Pt surface fraction, and improvement of durability. Even if the enhancement of area-specific activity would be limited in an actual world, mass-specific activity must be improved and the durability would be improved depending on the core material.

5.3 References

- ¹ Wang, J. X.; Ma, C.; Choi, Y.; Su, D.; Zhu, Y.; Liu, P.; Si, R.; Vukmirovic, M. B.; Zhang, Y.; Adzic, R. R., Kirkendall Effect and Lattice Contraction in Nanocatalysts: A New Strategy to Enhance Sustainable Activity. *Journal of the American Chemical Society* **2011**, *133*(34), 13551-13557.
- ² Wang, D.; Xin, H. L.; Hovden, R.; Wang, H.; Yu, Y.; Muller, D. A.; DiSalvo, F. J.; Abruña, H. D., Structurally ordered intermetallic platinum–cobalt core–shell nanoparticles with enhanced activity and stability as oxygen reduction electrocatalysts. *Nat Mater* **2013**, *12*(1), 81-87.
- ³ Xiong, L.; Manthiram, A., Influence of atomic ordering on the electrocatalytic activity of Pt-Co alloys in alkaline electrolyte and proton exchange membrane fuel cells. *Journal of Materials Chemistry* **2004**, *14*(9), 1454-1460.
- ⁴ Wanjala, B. N.; Luo, J.; Fang, B.; Mott, D.; Zhong, C.-J., Gold-platinum nanoparticles: alloying and phase segregation. *Ibid.* **2011**, *21*(12), 4012-4020.
- ⁵ Bart, J. C. J.; Vlaic, G., Extended X-Ray Absorption Fine Structure Studies in Catalysis. In *Advances in Catalysis*, D.D. Eley, H. P.; Paul, B. W., Eds. Academic Press: 1987; Vol. Volume 35, pp 1-138.
- ⁶ Zhang, J.; Lima, F. H. B.; Shao, M. H.; Sasaki, K.; Wang, J. X.; Hanson, J.; Adzic, R. R., Platinum Monolayer on Nonnoble Metal–Noble Metal Core–Shell Nanoparticle Electrocatalysts for O₂ Reduction. *The Journal of Physical Chemistry B* **2005**, *109*(48), 22701-22704.
- ⁷ Stamenkovic, V. R.; Mun, B. S.; Mayrhofer, K. J. J.; Ross, P. N.; Markovic, N. M., Effect of Surface Composition on Electronic Structure, Stability, and Electrocatalytic Properties of Pt-Transition Metal Alloys: Pt-Skin versus Pt-Skeleton Surfaces. *Journal of the American Chemical Society* **2006**, *128*(27), 8813-8819.
- ⁸ Adzic, R. R.; Zhang, J.; Sasaki, K.; Vukmirovic, M. B.; Shao, M.; Wang, J. X.; Nilekar, A. U.; Mavrikakis, M.; Valerio, J. A.; Uribe, F., Platinum Monolayer Fuel Cell Electrocatalysts. *Topics in Catalysis* **2007**, *46*(3-4), 249-262.
- ⁹ Lima, F. H. B.; de Castro, J. F. R.; Santos, L. G. R. A.; Ticianelli, E. A., Electrocatalysis of oxygen reduction on carbon-supported Pt–Co nanoparticles with low Pt content. *Journal of Power Sources* **2009**, *190*(2), 293-300.
- ¹⁰ Chen, S.; Sheng, W.; Yabuuchi, N.; Ferreira, P. J.; Allard, L. F.; Shao-Horn, Y., Origin of Oxygen Reduction Reaction Activity on “Pt₃Co” Nanoparticles: Atomically Resolved Chemical Compositions and Structures. *The Journal of Physical Chemistry C* **2009**, *113*(3), 1109-1125.
- ¹¹ Stamenkovic, V. R.; Fowler, B.; Mun, B. S.; Wang, G.; Ross, P. N.; Lucas, C. A.; Marković, N. M., Improved Oxygen Reduction Activity on Pt₃Ni(111) via Increased Surface Site Availability. *Science* **2007**, *315*(5811), 493-497.
- ¹² Stamenkovic, V. R.; Mun, B. S.; Arenz, M.; Mayrhofer, K. J. J.; Lucas, C. A.; Wang, G.; Ross, P. N.; Markovic, N. M., Trends in electrocatalysis on extended and nanoscale Pt-bimetallic alloy surfaces. *Nat Mater* **2007**, *6*(3), 241-247.
- ¹³ J, Z.; M.B, V.; K, S.; F, U.; R.R, A., Platinum monolayer electrocatalysts for oxygen reduction: Effect of substrates, and long-term stability. *Journal of the Serbian Chemical Society* **2005**, - *70*(- 3), - 525.
- ¹⁴ Zhang, J.; Vukmirovic, M. B.; Xu, Y.; Mavrikakis, M.; Adzic, R. R., Controlling the Catalytic Activity of Platinum-Monolayer Electrocatalysts for Oxygen Reduction with Different Substrates. *Angewandte Chemie International Edition* **2005**, *44*(14), 2132-2135.
- ¹⁵ Friebel, D.; Viswanathan, V.; Miller, D. J.; Anniyev, T.; Ogasawara, H.; Larsen, A. H.; O’Grady, C. P.; Nørskov, J. K.; Nilsson, A., Balance of Nanostructure and Bimetallic Interactions in Pt Model Fuel Cell Catalysts: In Situ XAS and DFT Study. *Journal of*

the American Chemical Society **2012**, *134* (23), 9664-9671.

¹⁶ Jia, Q.; Segre, C. U.; Ramaker, D.; Caldwell, K.; Trahan, M.; Mukerjee, S., Structure–property–activity correlations of Pt-bimetallic nanoparticles: A theoretical study.

Electrochimica Acta **2013**, *88* (0), 604-613.

¹⁷ Mukerjee, S.; Srinivasan, S.; Soriaga, M. P.; McBreen, J., Role of Structural and Electronic Properties of Pt and Pt Alloys on Electrocatalysis of Oxygen Reduction.

Journal of The Electrochemical Society **1995**, *142* (5), 1409-1422.

¹⁸ Nilekar, A. U.; Mavrikakis, M., Improved oxygen reduction reactivity of platinum monolayers on transition metal surfaces. *Surface Science* **2008**, *602* (14), L89-L94.

¹⁹ Tian, F.; Anderson, A. B., Effective Reversible Potential, Energy Loss, and Overpotential on Platinum Fuel Cell Cathodes. *The Journal of Physical Chemistry C* **2011**, *115* (10), 4076-4088.

²⁰ Wang, J. X.; Zhang, J.; Adzic, R. R., Double-Trap Kinetic Equation for the Oxygen Reduction Reaction on Pt(111) in Acidic Media†. *The Journal of Physical Chemistry A* **2007**, *111* (49), 12702-12710.

²¹ Weinhold, F.; Landis, C. R., NATURAL BOND ORBITALS AND EXTENSIONS OF LOCALIZED BONDING CONCEPTS. *Chemistry Education Research and Practice* **2001**, *2* (2), 91-104.

²² Ohwaki, T.; Otani, M.; Ozaki, T., A method of orbital analysis for large-scale first-principles simulations. *The Journal of Chemical Physics* **2014**, *140* (24), -.

²³ Ozaki, T.; Kino, H., Efficient projector expansion for the *ab initio* LCAO method. *Physical Review B* **2005**, *72* (4), 045121.

²⁴ Ohwaki *et al.* scheduled to be submitted to the *Journal of Physical chemistry C*.

²⁵ Marković, N. M.; Gasteiger, H. A.; Grgur, B. N.; Ross, P. N., Oxygen reduction reaction on Pt(111): effects of bromide. *Journal of Electroanalytical Chemistry* **1999**, *467* (1–2), 157-163.



Acknowledgement

I would like to express my gratitude to Professor Kiyotaka Asakura, Catalysis Research Center (CRC) in Hokkaido University for his invaluable advice, instructive discussions, and continual encouragement. All of the work described in my thesis was carried out under his supervision. He has been the best adviser for me for three years of my doctoral course. I had a lot of time to discuss many problems and questions relative to my thesis combining metaphor with him. I would like to make a grateful acknowledgment to Associate Prof. Satoru Takakusagi, CRC in Hokkaido University, for his valuable advice. I also owe Assistant Professor Hiroko Ariga and Assistant Professor Hiromitsu Uehara, CRC in Hokkaido University, for their kindly support. I am grateful to all the members of the Asakura lab.

I would like to express my sincere gratitude to Kazuhiko Shinohara, Hisashi Mitsumoto, Seiho Sugawara, Mitsutaka Abe, Nissan motor Co., LTD. for their support and I am grateful to all the members of Fuel cell electrocatalysts research member of the Nissan motor Co., LTD. I sincerely thank for Nissan motor Co., LTD. for its financial support. This thesis would not have been achieved without their help.

I would like to express my gratitude to the X-ray analysis team members of Nissan Arc for their help of at the XAFS experiment with long beam time at SPring-8.

I would like to express my thanks to the SUNBEAM of SPring-8 for the approval of experiment and for the helps at the experiment and the official works. Also I would like to appreciate the staffs of the Spring-8.

I thank all the professors and staffs in Division of Quantum Science and Engineering in Hokkaido University and CRC for their technical and official supports.

Finally, I sincerely thanks to my family for continual encouragement.